

A Search for  $\mu^- N \rightarrow e^- N$  with Sensitivity Below  $10^{-16}$

**M**uon – **E**lectron **C**Onversion

Proposal to Brookhaven National Laboratory AGS

M. Bachman, G. Kagel, R. Lee, T.J. Liu, W. Molzon, M. Overlin

University of California, Irvine

A. Empl, E.V. Hungerford, K. J. Lan,  
B.W. Mayes, L.S. Pinsky, J. Wilson, M. Youn

University of Houston

R.M. Djilkibaev, V.M. Lobashev, A.N. Toropin

Institute for Nuclear Research, Moscow

A. Mincer, P. Nemethy, J. Sculli

New York University

W.D. Wales

University of Pennsylvania

D. Koltick, S. Carabello,

Purdue University

PRIMARY BEAM	8-20 GeV proton beam pulsed at 1.11 MHz $4 \times 10^{13}$ per spill 2-3 second repetition rate, 50% duty cycle
PRIMARY TARGET	Radiation cooled tungsten
SECONDARY BEAM	Low energy, negative $\mu$ $5 \times 10^{11}$ per pulse
SECONDARY TARGET	Aluminum
TIME REQUESTED	4000 hours
SPOKESPERSON	W. Molzon Department of Physics and Astronomy University of California Irvine, CA 92697-4574 714 824-5987 wmolzon@uci.edu

September 1997

# Contents

<b>1</b>	<b>Introduction</b>	<b>1</b>
<b>2</b>	<b>Motivation for and Status of LFV Searches</b>	<b>2</b>
2.1	Introduction . . . . .	2
2.2	Experimental Status . . . . .	2
2.3	Theoretical Motivation for Continuing LFV Searches . . . . .	3
2.4	Current Status of $\mu^- N \rightarrow e^- N$ searches . . . . .	5
<b>3</b>	<b>Overview of the Experimental Technique</b>	<b>7</b>
<b>4</b>	<b>Physics Background Sources</b>	<b>9</b>
4.1	$\mu$ Decay in Orbit . . . . .	10
4.2	Radiative $\mu$ Capture . . . . .	10
4.3	Beam electrons . . . . .	11
4.4	$\mu$ Decay in Flight . . . . .	12
4.5	$\pi$ Decay in Flight . . . . .	13
4.6	Radiative $\pi$ Capture . . . . .	13
4.7	Cosmic Rays . . . . .	15
<b>5</b>	<b>Detector Rates</b>	<b>16</b>
<b>6</b>	<b>Choice of Accelerator for the Experiment</b>	<b>20</b>
<b>7</b>	<b>Pulsed Proton Beam</b>	<b>21</b>
7.1	$\mu$ Beam Design and Performance . . . . .	24
7.2	The Production Solenoid and Target Performance . . . . .	24
7.2.1	$\mu$ Production . . . . .	25
7.2.2	Target Cooling . . . . .	26
7.2.3	Solenoid Heat Load . . . . .	30
7.3	The Transport Solenoid . . . . .	34
<b>8</b>	<b>The MECO Detector</b>	<b>36</b>
8.1	The Detector Solenoid . . . . .	38
8.2	The Stopping Target . . . . .	39
8.3	The Tracking Detector . . . . .	41
8.3.1	Tracking Detector Performance Analysis . . . . .	43
8.3.2	Prototype Straw Chambers . . . . .	48
8.4	Electron Trigger Calorimeter . . . . .	51
8.5	Cosmic Ray Shielding . . . . .	56
8.5.1	Background Rate Calculation . . . . .	57
8.5.2	Hardware Implementation . . . . .	60
<b>9</b>	<b>MECO Expected Performance and Sensitivity</b>	<b>63</b>

<b>10 MECO Equipment Cost</b>	<b>65</b>
<b>11 MECO R&amp;D Plan</b>	<b>67</b>
<b>12 Acknowledgements</b>	<b>68</b>

# 1 Introduction

We propose to search for the process  $\mu^- N \rightarrow e^- N$  with a significantly improved sensitivity with respect to past and proposed future searches. Our interest is in searching for violations of additive quantum numbers associated with each type of lepton. Violation of these quantum numbers is commonly referred to as lepton flavor violation (LFV). This process, if observed, will provide direct evidence of muon and electron number violation.

The experiment will be conducted in a new  $\mu$  beam line at the AGS, produced using a pulsed proton beam. The proton energy will be chosen in the range 8-20 GeV to optimize the  $\mu$  flux per unit time and minimize operating costs of the experiment. The expected sensitivity, normalized to the kinematically similar process of  $\mu$  capture on the nucleus, is one event for a branching fraction of  $2 \times 10^{-17}$ .

In this proposal, we briefly review the physics motivation for such a search, discuss the present status and expected results of other experiments with related goals, outline the basic ideas of the experiment, and discuss the status and results of studies of the important experimental issues.

The reaction  $\mu^- N \rightarrow e^- N$  is closely related to the decay  $\mu \rightarrow e \gamma$ , with which particle physicists are perhaps more familiar. For example,  $\mu^- N \rightarrow e^- N$  can occur through the exchange of a virtual photon coupling the leptons to the nucleus. In that case, the rate for  $\mu \rightarrow e \gamma$  can be directly related to the rate for  $\mu^- N \rightarrow e^- N$ . More generally,  $\mu^- N \rightarrow e^- N$  can occur through the exchange of other particles, and in these situations, it is often a more sensitive probe of LFV.

The experiment is done by bringing a large flux of  $\mu^-$  to rest in a thin target. The  $\mu^-$  quickly become Coulomb bound to nuclei where they either decay or are captured on the nucleus (inverse  $\beta$  decay). For moderate size nuclei, these processes happen at about the same rate, and  $\mu$ 's disappear with a lifetime of about 1  $\mu$ s. If a  $\mu$  converts to an electron, it is emitted with energy equal to the  $\mu$  mass less the binding energy ( $\sim 0.5$  MeV) and is detected as an isolated electron originating in the stopping target. The conversion rate is conventionally normalized to the kinematically similar process  $\mu^- A \rightarrow \nu A'$ . In both cases, the final state consists of a nucleus and a light lepton with energy equal to nearly the rest energy of the  $\mu$ . We define the quantity  $R_{\mu e} = \Gamma(\mu^- A \rightarrow e^- A)/\Gamma(\mu^- A \rightarrow \nu A')$ .

Our MECO (Muon to Electron CONversion) [1] proposal builds on ideas from earlier experiments, in particular those of the early studies [2] and the MELC proposal [3] for an experiment at the Moscow Meson Factory. We have devised a new detector with improved performance and a new method of producing a momentum and charge selected  $\mu$  beam with low electron contamination. The experiment is also improved by using a high energy (in comparison with accelerators at which this type of experiment is typically done) synchrotron to produce the proton beam.

We believe that this experiment has a real chance of making a discovery of profound importance. This physics cannot be addressed at the *energy frontier*. There is no particular reason to believe that lepton flavor violation is more likely in the  $\tau$  lepton sector. Lepton flavor violating interactions of high energy hadrons or leptons cannot be detected directly, and even if this were possible, LFV decays of light particles are a more sensitive probe for any conceivable interaction luminosity at a high energy machine. The largest flux of  $\mu$ 's is produced at existing low energy accelerators and no facility is foreseen at which this

experiment could be done better and or on a comparable time scale.

The remainder of this proposal is organized as follows. We first discuss the motivation for and experimental status of searches for  $\mu$  and electron number violation. We then give a brief overview of the experimental technique, followed by a discussion of the physics backgrounds and sources of high signal rates in the experimental apparatus. We discuss why we have chosen BNL as the facility at which to do this experiment. We then discuss the new pulsed  $\mu$  beam which must be produced, and then describe the proposed experimental apparatus. Finally, we summarize the expected performance of the experiment, discuss the estimated cost, and describe an R & D plan to allow us to answer technical questions about the beam and detector and make a reliable cost estimate.

## 2 Motivation for and Status of LFV Searches

### 2.1 Introduction

The search for  $\mu$  and electron lepton number violation (LVF) has continued since shortly after the discovery of the  $\mu$ , with no evidence for such processes having been seen. The motivation to continue is twofold. First, electron,  $\mu$  and tau lepton number appear to be exactly conserved. These laws derive from observation and there is a compelling experimental interest in testing them. Second, these conservation laws are not the result of invariance under a local gauge transformation, and there is strong theoretical prejudice that violations will be seen.

The discovery of LFV processes would indicate the existence of either a new force mediated by new gauge bosons with nondiagonal lepton flavor couplings, or a new class of heavy particles with lepton flavor mixing in this new sector (e.g. supersymmetry). There exists the possibility of LFV in essentially all extensions to the Standard Model, and we discuss some of these in the following section.

There has been recent progress in LFV searches using both kaon processes and  $\mu$  processes. We list in table 1 the LFV processes which have been studied, the current experimental limits on these processes, and their classification in terms of a *generation number* in the model of Cahn and Harari [4]. The *generation number* may have significance in some models where mixing in the quark and lepton sectors are related; in any event it serves as a means of classifying related processes.

### 2.2 Experimental Status

Lepton flavor violation has been searched for in three  $\mu$  processes:  $\mu \rightarrow e\gamma$ ,  $\mu \rightarrow eee$ , and  $\mu^- N \rightarrow e^- N$ . If the underlying process is mediated by photon exchange,  $\mu \rightarrow e\gamma$  is usually most sensitive; the decay  $\mu \rightarrow eee$  requires an off-shell photon internally converting, and the process  $\mu^- N \rightarrow e^- N$  has an extra factor of  $Z\alpha$  for the coupling to the nucleus. For moderate to large nuclei and for a given strength process mediated by photons,  $\mu^- N \rightarrow e^- N$  is a factor of about 200 less sensitive [19] than  $\mu \rightarrow e\gamma$ . If the process is not mediated by a photon, then  $\mu^- N \rightarrow e^- N$  has clear advantages.

Experimentally,  $\mu \rightarrow e\gamma$  is limited by backgrounds from radiative  $\mu$  decay, with the

Table 1: LFV violating process, the change in generation number in the model of Cahn and Harari, the current experimental limits, and the inferred limits on intermediate particle masses (updated from the reference for new experimental results).

Process	$\Delta G$ [4]	limit	mass limit (TeV)
$K_L^0 \rightarrow \mu e$ [5, 6]	0,2	$2.4 \times 10^{-11}$	100
$K_L^0 \rightarrow \pi \mu e$ [8]	0,2	$3.2 \times 10^{-10}$	100
$K^+ \rightarrow \pi \mu e$ [9]	0	$2.1 \times 10^{-10}$	29
$\mu \rightarrow eee$ [10]	1	$1.0 \times 10^{-12}$	86
$\mu^+ \rightarrow e\gamma$ [11]	1	$1.7 \times 10^{-11}$	20
$\mu^- N \rightarrow e^- N$ [12]	1	$7.8 \times 10^{-13}$	500

photon and electron originating from either the same or different  $\mu$  decays. A significant experimental advantage for  $\mu^- N \rightarrow e^- N$  is that, since there is only one outgoing particle, there is no accidental background and the stopping rate can be much higher. Further, the sources of 104 MeV electrons are very much suppressed. This is contrasted with the case of  $\mu \rightarrow e\gamma$ , where the electron flux from  $\mu \rightarrow e\nu\bar{\nu}$  decay is peaked at the energy of the electrons from  $\mu \rightarrow e\gamma$ .

Two  $\mu$  experiments are analyzing data or in construction. The MEGA experiment [13] at Los Alamos is a search for  $\mu^+ \rightarrow e^+\gamma$  which has completed data taking and is analyzing. Results are anticipated soon, with a sensitivity of a few events for a branching fraction of  $10^{-11}$ . There are no proposals for more sensitive searches for this process, although a number of ideas for experiments which could reach a sensitivity close to  $10^{-14}$  have been discussed [14].

The second experimental program is SINDRUM2 at PSI, a search for the process  $\mu^- N \rightarrow e^- N$ . The first phase is completed, and a limit  $R_{\mu e} < 7.8 \times 10^{-13}$  at 90% confidence level has been set [12]. This program is continuing and an improvement by more than a factor of 10 is anticipated. We discuss that experiment in more detail in the section on our MECO proposal.

### 2.3 Theoretical Motivation for Continuing LFV Searches

Lepton flavor violation occurs in many extensions to the Standard Model. For example, in the most trivial extension with massive neutrinos, lepton flavor violating interactions will occur through loop diagrams, with mixing in an internal neutrino line. With the present limits on neutrino masses and mixing angles, the rates for lepton flavor violating processes ( $K_L^0 \rightarrow \mu e$  or  $\mu^- N \rightarrow e^- N$ , for example) are below the sensitivity of experiments that can be conceived today. Other models, for example those containing horizontal gauge bosons which explicitly couple one lepton family to another, do not have any particular scale at which lepton flavor violation should occur, since both the mass of the gauge boson and the mixing angle are unspecified. In the case of technicolor, the expectation was that lepton flavor violation would occur at levels which are already ruled out, and these models are

severely restricted by limits on LFV.

More interest has occurred recently in another scenario, where LFV occurs in supersymmetric grand unified theories. These models are particularly attractive, as supersymmetry is perhaps the most realistic candidate to solve many of the shortcomings of the Standard Model. Much of the experimental effort at high energy colliders (LEP, the Tevatron, the LHC) is directed towards discovering new massive particles at about the electroweak symmetry breaking scale, and much of that is devoted to supersymmetry searches.

It has recently been realized, first by Hall and Barbieri, that LFV will occur at experimentally accessible levels in a large class of supersymmetric models [15, 16, 17, 18]. Further, in some specific grand unified supersymmetric models, the rate for LFV processes can be directly related to standard model parameters. A set of Feynman diagrams from one such model is shown in figure 1, taken from reference [18]. The predicted rates for the processes

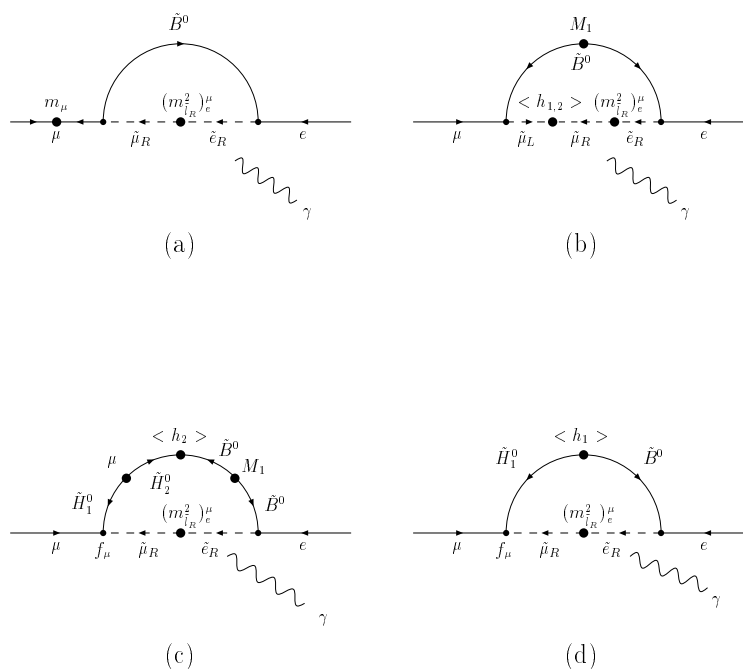


Figure 1: Examples of Feynman diagrams for  $\mu^- N \rightarrow e^- N$  containing supersymmetric partners of SM particles. The same diagrams contribute to  $\mu \rightarrow e\gamma$ .

$\mu^- N \rightarrow e^- N$  and  $\mu \rightarrow e\gamma$  are plotted in figure 2.

In this model, where the interaction with the nucleus is mediated by a photon, the branching fraction for  $\mu \rightarrow e\gamma$  is greater by a factor of about 100 than the probability of conversion of a  $\mu^-$  in a Coulomb orbit. In other models, in which the process is mediated by something other than a photon (in some SU(5) models, for example) the branching fraction for  $\mu^- N \rightarrow e^- N$  can be greater than that for  $\mu \rightarrow e\gamma$ .

If grand unified supersymmetric models are correct, a search for  $\mu^- N \rightarrow e^- N$  with sensitivity of  $10^{-16}$  has a real potential for making a discovery.

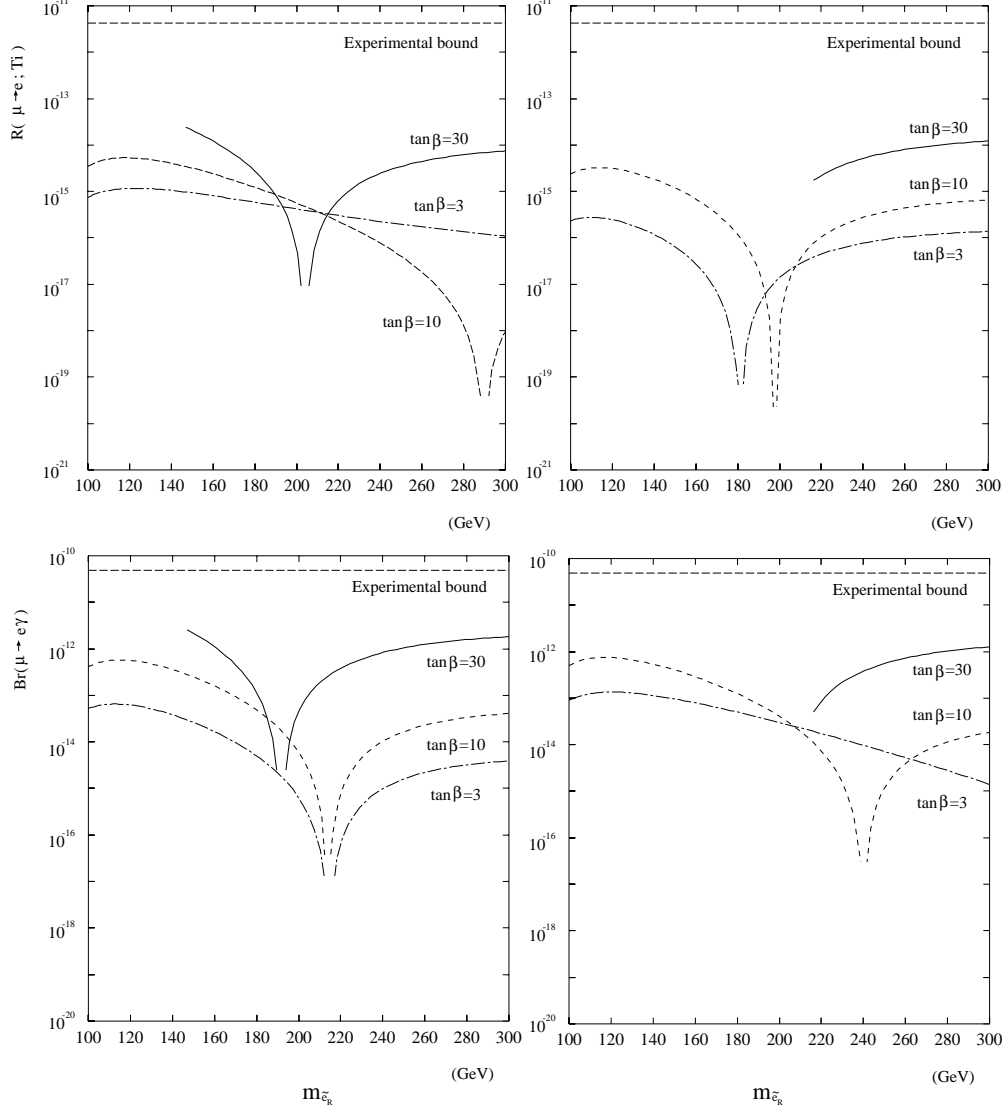


Figure 2: Expected rates for  $\mu^- N \rightarrow e^- N$  and  $\mu \rightarrow e \gamma$  in the model of Hisano, et al., for different values of the ratio of Higg's particle vacuum expectation values, as a function of the right handed squark mass. The plots are shown for the parameter  $\mu > 0$  (left) and  $\mu < 0$  (right).

## 2.4 Current Status of $\mu^- N \rightarrow e^- N$ searches

The current best limit for  $\mu^- N \rightarrow e^- N$  derives from the SINDRUM2 experiment at PSI [12], which has set an upper bound on  $R_{\mu e}$  at  $7.8 \times 10^{-13}$  (90% CL), as yet unpublished. They propose to improve their sensitivity to  $4 \times 10^{-14}$  with a new beam and new background rejection technique.

It is instructive to look at this experiment to understand why the technique used there cannot be pushed significantly further. Figure 3 shows a cut view of the present apparatus. It is a cylindrical detector, with drift chambers in a solenoidal field to measure the electron



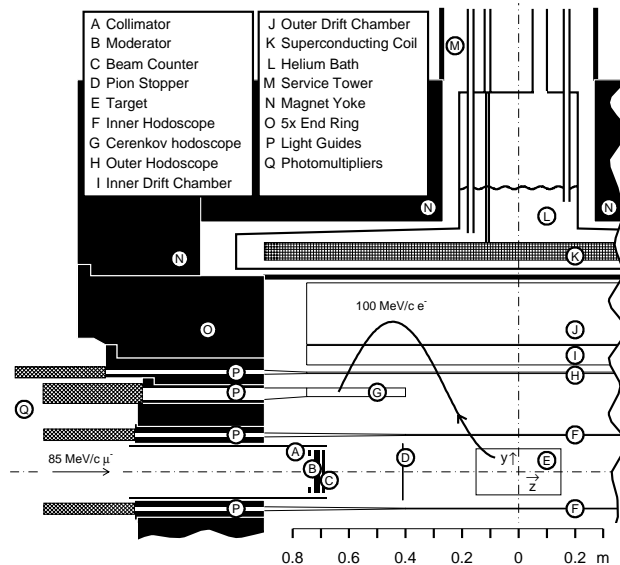


Figure 3: A cut view of the SINDRUM2  $\mu^-N \rightarrow e^-N$  apparatus.

momentum. Mouns are stopped in a target on the axis of the solenoid. The resolution in the SINDRUM2 case is limited by dispersion in the energy loss in the target and the scintillation counters. The beam is continuous, and contains a mixture of  $\mu$ 's,  $\pi$ 's and electrons. The stopping rate is about  $10^7 \text{ s}^{-1}$ . In SINDRUM2, backgrounds from stopping  $\pi$ 's, scattered electrons, and  $\mu$  decay in flight are eliminated by rejecting events in which there is a signal in a thin scintillator in the beam time coincident with the detected electron. Figure 4 shows the energy spectrum of electrons before two sets of cuts are applied. The first set is designed to eliminate cosmic ray induced backgrounds, and basically removes events with other signals in the detector. The background removed by these cuts is shown as the heavy shaded area. The lighter shaded area are those events eliminated by cuts on the beam scintillator. The lightest shading indicates the events remaining after all cuts, and are presumably dominated by the  $\mu$  decay in a Coulomb bound state.

To further improve the sensitivity, the SINDRUM2 collaboration proposes to increase the stopping rate to  $10^8 \text{ s}^{-1}$ , at which point they will no longer be able to use a beam veto. They propose to eliminate the prompt background by purifying the beam, eliminating all  $\pi$ 's, and reducing the beam energy so that  $\mu$ 's decaying in flight will not result in electrons sufficiently energetic to cause backgrounds. The beam they propose has an absorber on the axis of a solenoid to absorb undecayed  $\pi$ 's. From figure 4, we see that the prompt veto eliminates about 200 events in a sample with a limit of  $8 \times 10^{-13}$ , implying about 4000 events of that type for a sample which would yield a limit of  $4 \times 10^{-14}$ . Hence, the beam will have to be cleaner by a factor of 4000 to be background free. Improving the sensitivity by a further 3 orders of magnitude using similar techniques is not possible.

The cosmic ray background in the SINDRUM2 detector is thought to come primarily from photon conversions in the stopping target [20]. They eliminate events with extra track segments in the detector. As discussed below, we have found that a GEANT simulation of

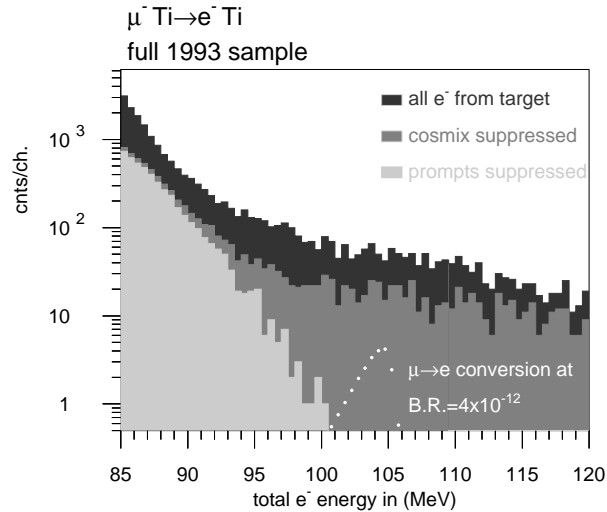


Figure 4: Histogram of the electron energy distribution from the SINDRUM2 experiment. The unshaded is after all cuts, lightly shaded are events removed by “prompt” cuts, and the heavily shaded is events removed by cosmic ray cuts.

our detector and shielding shows that the primary source of cosmic ray background is from  $\mu$  interactions and decays within the detector volume.

Figure 4 shows that the intrinsic background due to  $\mu$  decay in the Coulomb bound orbit is well separated from the signal region. Near the endpoint, the background is proportional to  $(E_{max} - E)^5$ . Hence, with the SINDRUM2 resolution, we will expect about 1 background event per MeV at 102.5 MeV ( a factor of 2 closer to the endpoint than the present 1 background event level) with about 32 times the sensitivity, or about the expected new SINDRUM2 sensitivity. At lower sensitivity, this background would dominate the signal with the SINDRUM2 resolution.

We conclude that a significantly different technique is required to reach sensitivity below  $10^{-16}$ . It requires a much more intense  $\mu$  beam, with  $\sim 10^{11}$  stops per second, and significantly improved background rejection.

### 3 Overview of the Experimental Technique

The proposed experimental technique uses a new  $\mu$  production source,  $\mu$  transport, and detector design to allow significantly higher sensitivity. The details of each of these aspects of the experiment are discussed in subsequent sections. Here we give a brief description of the experimental technique. A schematic drawing of the  $\mu$  production target,  $\mu$  beam transport, and the stopping target and detectors is shown in figure 5. The whole region of the  $\mu$  production target, transport, and detector are in vacuum.

In order to reduce prompt backgrounds (as defined in the previous section), the  $\mu$  beam is pulsed with a pulse spacing of order the  $\mu$  lifetime in the stopping target. To maximize the sensitivity, the pulse rate should be comparable to the rate at which  $\mu$ 's disappear through

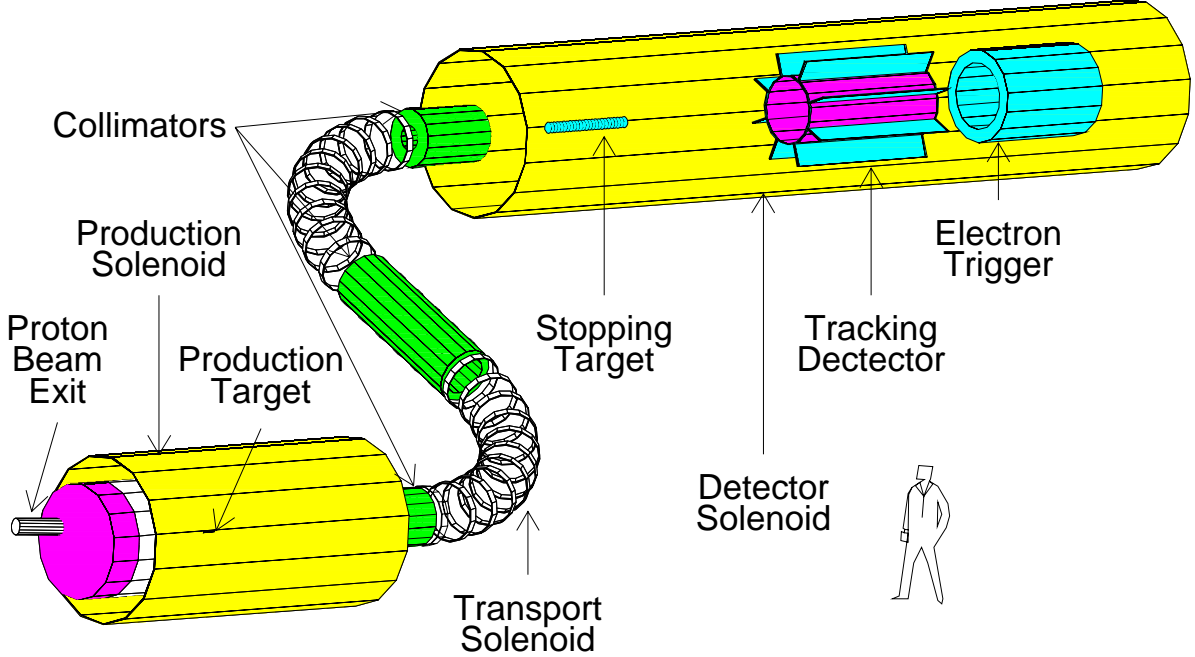


Figure 5: Schematic drawing of the production solenoid, transport solenoid, and detector solenoid with the targets, collimators, and detectors.

decay or capture. The requirement that we detect conversion electrons only after most  $\pi$ 's (which cause background) have decayed argues for a relatively low  $Z$  target, in which  $\mu$ 's have a relatively long lifetime. Since high  $Z$  targets have an advantage in terms of sensitivity to the underlying physics, this argues for a high  $Z$  target, in which  $\mu$ 's have a relatively short lifetime. A suitable compromise is to choose a stopping target such that the  $\mu^-$  lifetime in the target is about  $1 \mu\text{s}$ . The choice of stopping target is further influenced by the requirement that the nucleus which results from  $\mu$  capture be higher mass than the target mass, so that photons from radiative  $\mu$  capture cannot have energy greater than the  $\mu$  rest energy. Aluminum, with a lifetime for  $\mu$ 's of 880 ns, and a maximum energy of 102.5 MeV for photons resulting from radiative  $\mu$  capture, is chosen. The pulse frequency is then about 1 MHz, the exact frequency depending on details of the accelerator used.

The pulsed  $\mu$  beam is derived from a pulsed proton beam. We propose that the beam be produced by extracting a bunched beam from the AGS and using a secondary device to further reduce the ratio of proton rate between pulses to that during pulses.

The  $\mu$ 's are produced from a high  $Z$  (tungsten) target in a production solenoid, where the axial component of the field varies from  $\sim 3 \text{ T}$  at the end away from the  $\mu$  beam direction to  $2 \text{ T}$  at the end where the  $\mu$  beam exits the production solenoid. This geometry results in a very high capture probability for  $\pi$ 's and the  $\mu$ 's into which they decay. This is due to the fact that  $\pi$ 's and  $\mu$ 's initially traveling away from the  $\mu$  beam direction (toward the high field region of the solenoid) are reflected by the field, as in a magnetic bottle. The  $\mu$ 's are transported to the stopping target and detector region in a curved transport solenoid. The effect of the curvature on particles propagating in helical trajectories in the solenoid is exploited to sign and momentum select the beam. This is important for rate and background

issues as will be discussed.

The  $\mu$  stopping target and detector are located in a detector solenoid, with the axial component of the field decreasing from 2 T at the entrance end to 1 T just before the detector region. The detector is located downstream of the target in order to minimize rates in it due to particles coming from the target. The axially graded field has the same magnetic bottle effect as in the production solenoid, and results in very good acceptance for 105 MeV electrons originating in the target. It also has advantages in distinguishing electrons produced in the upstream pole piece of the production solenoid from those produced in the target.

The tracking detector is required to have little mass in order to minimize the contribution of multiple scattering and energy loss to the electron energy measurement resolution. A resolution of  $\sim 300$  keV, including the effects of energy loss straggling in the target, can be achieved with a detector composed of either straw chambers or a combination of straw chambers and scintillating fibers. This is sufficient to reduce the background from  $\mu$  decay in orbit to an acceptable level.

The trigger detector's primary purpose is to select events to be recorded for offline analysis by requiring an energy deposit in the detector consistent with that of a 105 MeV electron. In addition, it provides some confirmation of the electron energy, aids in distinguishing electrons from other particles, and helps in identifying backgrounds from particles produced by cosmic rays.

The whole region of the detector is surrounded by a cosmic ray shield. It has passive and active components, to minimize the rate of production of electrons by cosmic ray  $\mu$ 's and to identify those electrons which are produced in time with a cosmic ray  $\mu$  traversing the detector.

## 4 Physics Background Sources

We next discuss the backgrounds to the  $\mu^- N \rightarrow e^- N$  signal, which motivates many of the basic ideas of our experiment. The primary sources are:

1. Muon decay in a Coulomb bound orbit, with an electron energy endpoint equal to the energy of the signal.
2. Radiative  $\mu$  capture on a nucleus with a photon energy endpoint 2.5 MeV below the energy of the signal electrons.
3. Beam electrons which scatter in the stopping target.
4.  $\mu$  decay in flight.
5.  $\pi$  decay in flight.
6. Radiative  $\pi$  capture on a nucleus, a photon energy endpoint equal to  $m_\pi$ .
7. Cosmic ray induced electrons

The first two sources of background are intrinsic to  $\mu$ 's stopped in the target; they can be minimized by improving the measurement of the electron energy.

Sources 3-6 derive from prompt processes, with the electron detected close in time to the arrival of a beam particle in the detector. It is for the purpose of eliminating this background that we conclude that a pulsed beam is necessary. A pulsed beam has been used in an earlier experiment [21]. A first estimate of the required extinction can be done by reference to the SINDRUM2 data. Without the beam veto there is one prompt background at a sensitivity of about  $10^{-10}$ . To get an expected background below 0.01 events at a branching fraction of  $10^{-16}$  would require a beam extinction of  $10^{-8}$ . We have found that the ratio of the flux of prompt  $\pi$ 's and electrons to that of  $\mu$ 's is somewhat higher for our beam, and we will need a beam extinction (defined to be the ratio of the number of protons between pulses to that during pulses) of  $\sim 10^{-10}$ .

Cosmic ray background scales with running time, not sensitivity, and can be reduced with appropriate active and passive shielding.

We next discuss the results of our calculations of each source of background in more detail.

## 4.1 $\mu$ Decay in Orbit

The rate for production of electrons from  $\mu$  decay in Coulomb bound orbit approximately proportional to  $(E_{max} - E_e)^5$  near the endpoint [22]. Hence the signal/background ratio is extremely sensitive to resolution. Removing high energy tails in the energy resolution function is of critical importance to reducing the background. Figure 6 shows the signal and background for  $R_{\mu e} = 10^{-16}$  for two different designs of the detector, with effects of target energy loss and detector spatial resolutions taken into account. These distributions were calculated in a full GEANT simulation [24] which is discussed in detail later.

In figure 6, the detected energy is shifted below 105 MeV due to energy loss in the target and in the detector flanges. By accepting events between 103.9 MeV and 105.4 MeV, the noise to signal ratio is below 0.05 with large acceptance for signal events. The FWHM for both detectors is 1 MeV or below, with very little high energy tail in the resolution function. More discussions of the detector design and the resolution function will follow.

## 4.2 Radiative $\mu$ Capture

Radiative  $\mu$  capture background results from the process  $\mu^- Al \rightarrow \gamma \nu_\mu Mg$ . The photon endpoint energy is 102.5 MeV and the probability (per  $\mu$  capture) of producing a photon with energy exceeding 100.5 MeV is  $\sim 4 \times 10^{-9}$  [25]. The conversion probability in the target is  $\sim 0.005$ , and the probability of the electron energy exceeding 100 MeV is  $\sim 0.005$ . The probability of producing an electron above 100 MeV is then  $[4 \times 10^{-9}] \times [5 \times 10^{-3}] \times [5 \times 10^{-3}] = 10^{-13}$ . Further, these electrons are all less than 102 MeV (most are near 100 MeV), and for an electron to be considered as signal, its measured energy must exceed 103.9 MeV. The integral of the high energy tail in the resolution function above 1.9 MeV is less than  $10^{-5}$  (limited by statistics). Hence, the probability of getting an electron above 103.9 from radiative  $\mu$  capture is less than  $10^{-18}$  or a signal/noise ratio of greater than 100 for  $R_{\mu e} = 10^{-16}$ .

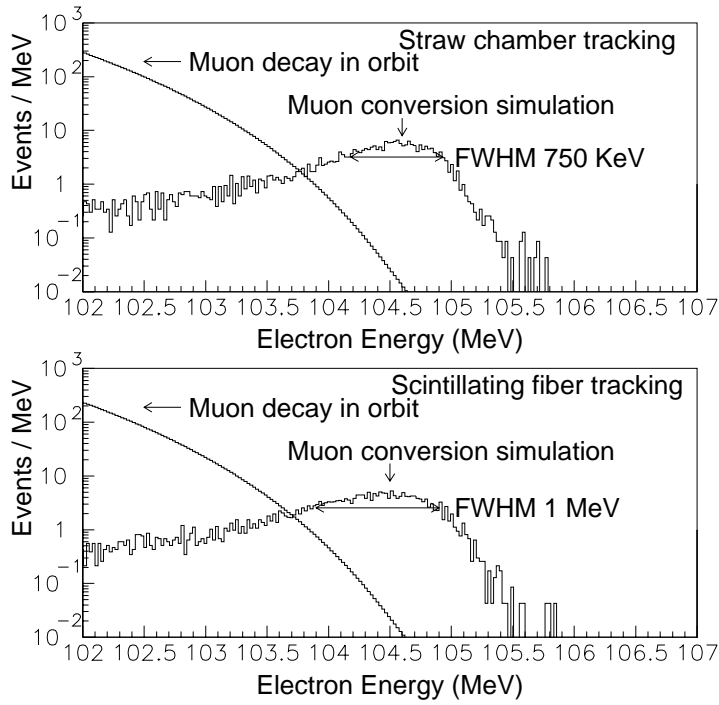


Figure 6: A simulation of the expected signal and background for  $R_{\mu e} = 10^{-16}$  for two different proposed detectors. The vertical scale is arbitrary; the relative normalization of the signal and background curves is for  $R_{\mu e} = 10^{-16}$  and we would see  $\sim 5$  events above 103.9 MeV at this value for the nominal running time of  $10^7$  seconds.

### 4.3 Beam electrons

Beam electrons which cause background must be produced in the production or transport solenoid region and then scatter in the stopping target in order to simulate signal events.

The rate for electrons scattering at  $\sim 100$  MeV is defined by the Mott cross section multiplied by a nuclear form factor for the target material. The experimentally determined [26] form factor for aluminum is shown in figure 7. Figure 8 shows the scattering cross section on aluminum for Mott scattering, and with the form factor included.

The collimator system is designed to suppress high energy electrons. A GEANT simulation of the production of electrons and their transport to the detector solenoid yielded no transmitted electrons above 100 MeV for  $10^7$  incident protons. Lacking any events at the  $10^{-7}$  level, we take the transverse momentum distribution to be that of electrons of 70–90 MeV (essentially flat from 0–20 MeV/c), and use that distribution to calculate the probability of scattering in the target to a transverse momentum exceeding 90 MeV/c. Including the solid angle acceptance, the probability that electrons of 100 MeV scatter with  $p_t > 90$  MeV/c is about  $10^{-5}$ . With a run time of  $10^7$  sec, a proton intensity of  $2 \times 10^{13}$  p/s, and a beam extinction of  $10^{-10}$ , the total number of background events is less than:

$$[10^7] \times [2 \times 10^{13}] \times [10^{-10}] \times [10^{-7}] \times [10^{-5}] = 0.02$$

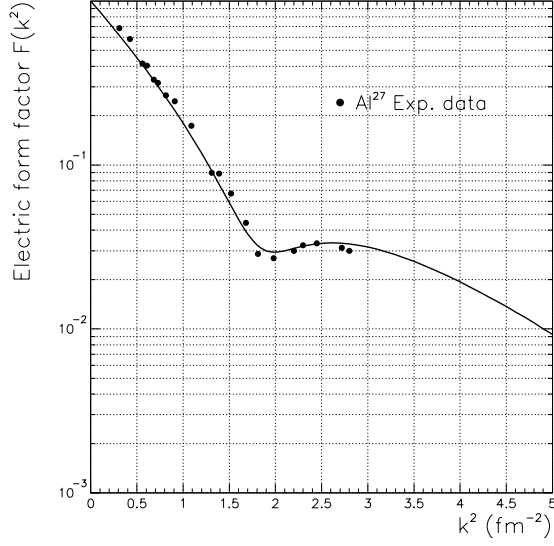


Figure 7: The form factor for electrons scattering on aluminum.

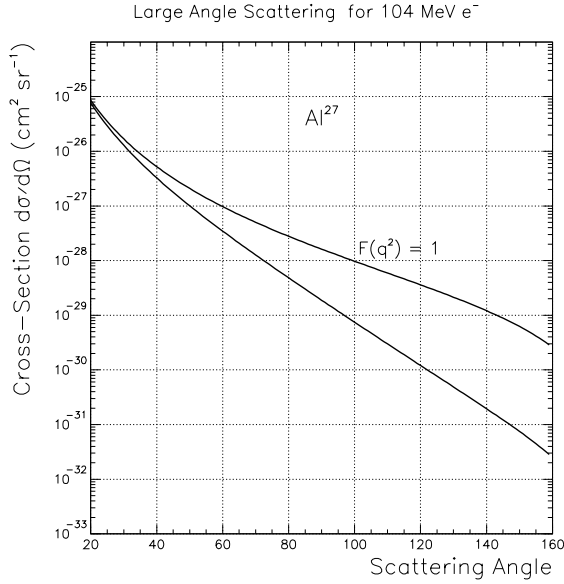


Figure 8: The electron scattering cross section as a function of scattering angle for 100 MeV electrons. Cross sections are shown for the Mott formula, and with the inclusion of the nuclear form factor.

#### 4.4 $\mu$ Decay in Flight

Muon decay in flight can result in energetic electrons which either have sufficient transverse momentum to fake signal or scatter in the stopping target and fake signal. In order for the electron to have energy above 102 MeV, the  $\mu$  momentum must exceed 77 MeV. Electrons produced by  $\mu$  decays before and within the transport solenoid are included in the beam electron background calculation. Background from decays in the detector solenoid are calculated using a GEANT beam simulation. The yield of  $\mu$ 's with  $p_\mu > 77$  MeV passing the

transport solenoid is  $\sim 1.1 \times 10^{-4}$ , the decay probability upstream of the tracking detector is  $1.2 \times 10^{-2}$ , and the probability of having  $103 \text{ MeV} < E_e < 105 \text{ MeV}$  and  $p_t > 90 \text{ MeV}$  is less than  $1.2 \times 10^{-7}$  with no events seen in a larger energy interval. With a beam extinction of  $10^{-10}$ , the total background in a one year run is less than:

$$[10^7] \times [2 \times 10^{13}] \times [10^{-10}] \times [1.1 \times 10^{-4}] \times [1.2 \times 10^{-2}] \times [1.2 \times 10^{-7}] = 0.003.$$

A second background source is electrons from  $\mu$  decay which scatter in the stopping target. The GEANT simulation was used to calculate the energy distribution of electrons from  $\mu$ 's which passed the transport solenoid and decayed in the region between the entrance to the production solenoid and the tracking detector. The kinematical distribution of these electrons was then used as input to a simple simulation of the probability that an electron of the appropriate energy scattered in the stopping target with a resulting transverse momentum exceeding  $90 \text{ MeV}/c$ . The probability per proton of getting an electron with  $103 \text{ MeV} < E_e < 105 \text{ MeV}$  from a  $\mu$  decay, per proton, is  $1.0 \times 10^{-8}$  and the probability of scattering to  $p_t > 90 \text{ MeV}/c$  is  $2 \times 10^{-5}$ , resulting in an expected number of background events of:

$$[10^7] \times [2 \times 10^{13}] \times [10^{-10}] \times [1 \times 10^{-8}] \times [2 \times 10^{-5}] = 0.004.$$

## 4.5 $\pi$ Decay in Flight

Beam  $\pi$ 's decaying to electrons with  $E_e > 102 \text{ MeV}$  and  $p_T > 90 \text{ MeV}/c$  are also a potential source of background. The  $\pi$  momentum must exceed  $60 \text{ MeV}$  for this background process. A GEANT simulation was used to calculate the probability of a proton producing a beam  $\pi$  with  $p_\pi > 54 \text{ MeV}/c$  passing the transport solenoid; it is  $4 \times 10^{-6}$ . The probability for a  $\pi$  to decay into an electron after the transport solenoid and before the tracking detector is  $1 \times 10^{-4}$  and the probability of the decay electron to have  $E_e > 102 \text{ MeV}$  and  $p_t > 90 \text{ MeV}$  is  $5 \times 10^{-6}$ . The background from this source is:

$$[10^7] \times [2 \times 10^{13}] \times [10^{-10}] \times [4 \times 10^{-6}] \times [1 \times 10^{-4}] \times [5 \times 10^{-6}] = 0.00004$$

A second background mechanism is  $\pi$  decay electrons which scatter in the stopping target. This background was calculated in much the same way as the similar process for  $\mu$  decay. The number of electrons from  $\pi$  decay with  $103 \text{ MeV} < E_e < 105 \text{ MeV}$  per proton is  $1.6 \times 10^{-11}$  and the probability of scattering to  $p_t > 90 \text{ MeV}/c$  is  $4 \times 10^{-5}$ , resulting in an expected number of background events of:

$$[10^7] \times [2 \times 10^{13}] \times [10^{-10}] \times [1.6 \times 10^{-11}] \times [4 \times 10^{-5}] = 0.00001.$$

## 4.6 Radiative $\pi$ Capture

Stopped  $\pi^-$ s are immediately captured by a nucleus after they stop in the target; about 2% of the captures result in the emission of a photon [27] without significant nuclear excitation. The photon energy spectrum has a peak at  $110 \text{ MeV}$  and endpoint at  $140 \text{ MeV}$ . The probability of photon conversion in the Al target, with a conversion electron in a  $1.5 \text{ MeV}$  energy interval around  $104 \text{ MeV}$  is  $3.5 \times 10^{-5}$ , as calculated in a GEANT simulation. The acceptance for electrons from photon conversion is large ( $\sim 0.8$ ), since the path length for conversion is largest for photons emitted at  $90^\circ$ . The yield of  $\pi^-$ 's which pass the transport solenoid and stop in the target is  $\sim 6 \times 10^{-7}$  per proton. Accounting for the beam extinction of  $10^{-10}$ ,



the background is:

$$[10^7] \times [2 \times 10^{13}] \times [10^{-10}] \times [6 \times 10^{-7}] \times [0.02] \times [3.5 \times 10^{-5}] \times [0.8] = 0.007$$

A contribution which is more difficult to calculate is that due to  $\pi$ 's which take a very long time to traverse the production and transport solenoid and arrive at the stopping target. For these events, the suppression factor of  $10^{-10}$  from the beam extinction is absent. However, since our detection window starts  $\sim 600$  ns after the proton pulse, the  $\pi$ 's must live approximately 600 ns and must follow a trajectory in the transport solenoid which results in a flight time of 600 ns in order to be a source of background. This background is estimated as follows. A total of  $10^7$  protons are caused to impinge on the production target. The momentum, position, and time coordinates are recorded for  $\pi$ 's which reach the entrance of the transport solenoid. These events are then transported to the stopping target without allowing them to decay. About 400  $\pi$ 's stop in the target at least 450 ns after the production time.

Figure 9 shows the distribution in the arrival time at the stopping target, weighted by

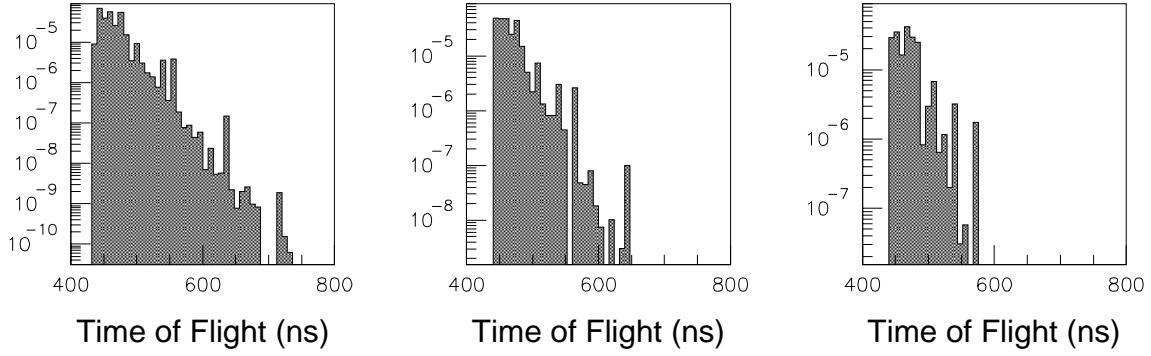


Figure 9: The distribution in the  $\pi$  arrival time for late arriving  $\pi$ 's, weighted by the survival probability in the transport solenoid. The distributions are shown for no absorber (left), 100  $\mu\text{m}$  Al (middle), and 200  $\mu\text{m}$  Al (right).

the survival probability. Figure 10 shows the distribution in the momentum of these  $\pi$ 's, also weighted by the survival probability. Based on the time distribution in figure 9 we take an accepted time window starting 600 ns after the proton pulse (the minimum flight time to the target is  $\sim 50$  ns). When weighted by the survival probability from the beginning of the transport solenoid to the stopping target, a total of  $2.0 \times 10^{-7}$   $\pi$ 's from  $10^7$  protons stop in the target at least 600 ns after the proton pulse, or  $2.0 \times 10^{-14}$  late stopped  $\pi$ 's per proton. The probability of making a background electron is  $5.6 \times 10^{-7}$  (see the preceding paragraph). Hence, without further suppression, the total background is:

$$[10^7] \times [2 \times 10^{13}] \times [2.0 \times 10^{-14}] \times [5.6 \times 10^{-7}] = 2.2.$$

Two means exist to further suppress these events. First, the late arriving  $\pi$ 's are very low energy, and can be absorbed with high efficiency in a very thin window. We have calculated, using a GEANT simulation, the attenuation of these events using an aluminum absorber of either 100  $\mu\text{m}$  or 200  $\mu\text{m}$  thickness at the exit of the transport solenoid. Figures 9 and 10 show the weighted arrival time and energy distributions of events passing the absorbers. The

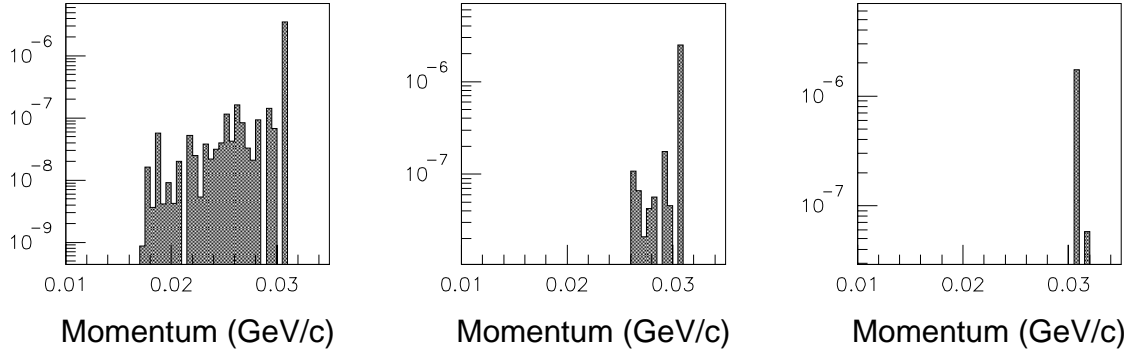


Figure 10: The distribution in the  $\pi$  momentum for late arriving  $\pi$ 's, weighted by the survival probability in the transport solenoid. The distributions are shown for no absorber (left), 100  $\mu\text{m}$  Al (middle), and 200  $\mu\text{m}$  Al (right).

weighted numbers of stopping  $\pi$ 's per proton in these cases are  $1.2 \times 10^{-14}$  and 0, resulting in backgrounds of 1.4 and 0 events. For the latter case, we estimate the actual level by fitting the time distribution, and extrapolating the curve to get the integral above 600 ns. That gives  $7 \times 10^{-16}$  stopped pions per proton, corresponding to a background of 0.1 events. The decrease in  $\mu$  stops in the target is  $\sim 3\%$  and  $\sim 6\%$  for the two thicknesses. We note that some higher energy  $\pi$ 's are degraded, and hence move slowly from there to the stopping target. Since this path length is small, this does not result in a new source of background from late arriving  $\pi$ 's.

The second means of suppression is simply to delay the start of the timing window from the nominal 600 ns, so that the late arriving  $\pi$ 's are further suppressed due to decays. For example, if the start time is at 700 ns instead, this corresponds to a suppression factor of about 100 (from figure 9) resulting in backgrounds of 0.014 events in the case of the smaller absorption thickness. This reduces the fraction of  $\mu$  captures in the timing window, as will be discussed in the sensitivity section. We assume the background from late arriving  $\pi$ 's will be reduced to this level.

We note that if the axial component of the field is continuously decreasing, the longitudinal component of the moment continuously increases. In our simulations, we have a constant field region at the upstream end of the production solenoid and the transport solenoid is constant field. That will allow particles to move very slowly in the axial direction. We will explore whether a small gradient in the field regions which are now constant decreases the probability of late arrivals. We are optimistic that this background can be reduced.

Late arriving  $\pi$ 's is what drives the specific choice of the time structure of the pulsed beam, and we will discuss that in the section on the MECO sensitivity.

## 4.7 Cosmic Rays

Cosmic ray induced electrons are potentially a limiting background and we have studied it using a GEANT simulation [28] of the detector and shielding. The details of the simulation

and the shielding required to reduce the background to a negligible level are discussed in a later section. The conclusion of these studies is that cosmic ray background can be reduced to a negligible level with a combination of active and passive shielding and detection of extra particles in the tracking detector. These consist of the following:

- A passive shield of modest thickness (2 m of concrete and 0.5 m of steel).
- Two layers of scintillator veto counter surrounding the detector, with a combined efficiency for charged particles of 99.99%.
- Selection criteria which eliminate events having significant evidence of extra particles in the detector in time with the electron candidate.

With this suppression, the expected background from cosmic rays in a  $10^7$  second run is estimated to be  $\sim 0.0035$  events.

## 5 Detector Rates

High rates in the detector may limit the experimental sensitivity in several ways. First, the occupancy might be so high as to make the detection efficiency low, by corrupting signals from candidate electrons. Second, signals in the detectors may fake those of a real electron. For example, by superimposing noise hits on those from a low energy (100 MeV, for example) electron, the energy could be mismeasured and confused with a signal event of 105 MeV. This possibility may be addressed by requiring that the hit-population within the coincidence resolving time of the tracking detector be so small that pattern recognition can exclude false trajectories. Third, there may be contributions to the trigger rate due to pileup of many low energy particles in the trigger detector. This possibility may be reduced by segmentation and geometric design of the trigger device.

In this section, we discuss the calculations of the rates in the detectors. The effect of these rates on the physics signal has not been calculated in detail; we make some comments on the possible effects in the section on the tracking detector simulation. The effect on trigger rates is discussed in the section on that detector. Neither of the latter two effects seems to be a serious problem.

The time structure of the beam helps mitigate the effects of the high stopping rate. During the pulse of stopping  $\mu$ 's, when there is a very high flux of charged particles traversing the experiment, we will not detect conversion electrons. The rate will likely be sufficiently high that we will decrease detector voltages during that time. However, even within the time window when the detectors are operational, a substantial flux of particles, primarily resulting from  $\mu$  capture processes and  $\mu$  decay, traverse the detector. The primary sources of charged particle fluxes in the detector during the detection time are electrons from  $\mu$  decay in orbit and photons, neutrons, and protons from  $\mu$  capture.

To minimize the rate from  $\mu$  decay electrons, the inner radius of the tracking detector is chosen to ensure that most of them do not hit the tracking detector. These rates were calculated using a full GEANT simulation, and using the spectrum of electrons from this process as shown in figure 11.

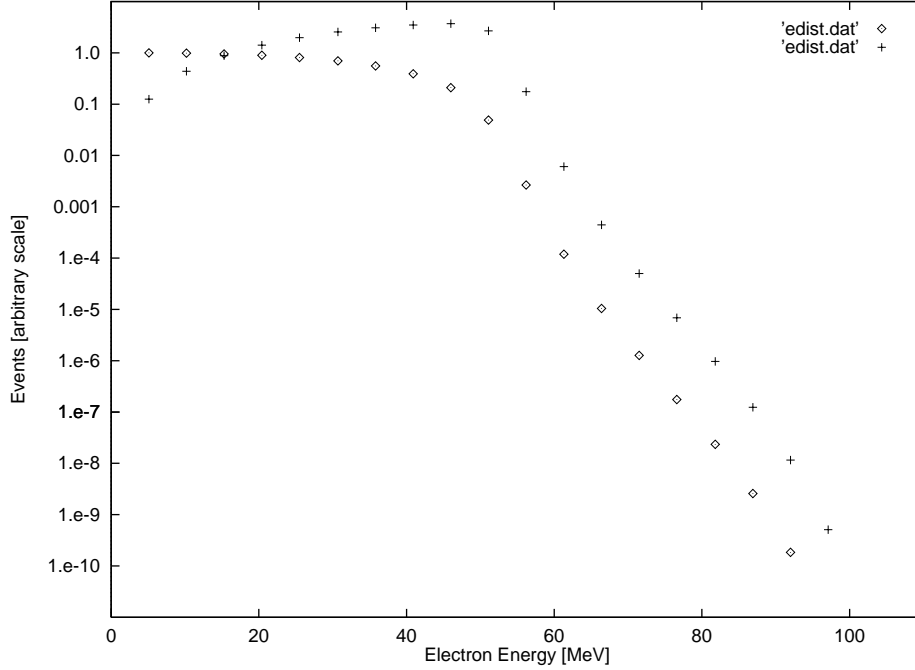


Figure 11: Plot of the differential and integral electron energy distributions for  $\mu$  decay in orbit. The circles are the integral of the distribution for energies above the abscissa value, and the crosses are the differential distribution.

The detector rate from  $\gamma$ 's is dominated by conversions and Compton scattering of those below 10 MeV. This spectrum is difficult to estimate. Every  $\mu$  capture results in the production of excited nuclear states, radioactive nuclei, and/or neutron emission with the possibility of subsequent neutron induced nuclear gamma rays. This results in photons originating from various places in the detector solenoid, some fraction of which are not even time associated with the beam gating. Almost all of these photons are less than a few MeV (the binding energies of the most probable excited nuclei after  $\mu$  capture are less than 4 MeV). To proceed we analyze the effects of a flat energy spectrum at a rate of 1.8 photons per  $\mu$  capture.

Neutrons are produced during the  $\mu$ -capture process. A neutron spectrum, typical for our target, can be created from experimental data [29, 30]. The spectrum is divided by energy. The neutrons below 10 MeV are produced by a thermal distribution and there is an exponential tail above 10 MeV. A GEANT simulation showed that the effects of the neutron flux on the detector rates are negligible.

Protons are also emitted during the  $\mu$ -capture process. The proton spectrum shape, which is predominately due to protons below 15 MeV, was taken from an experiment [31] using  $\mu$ 's stopping in emulsion. The shape is almost Gaussian centered at a proton energy of  $\sim 7.5$  MeV with a width of  $\sim 5.5$  MeV a high energy tail extending to above 25 MeV. The spectrum is normalized to 0.035 protons per stopped  $\mu$ , as extrapolated from the data of Wyttenbach *et al.* [32]. This normalization is rather uncertain, since it depends on extrapolating from the rate measured on nuclei larger than aluminum. The proton spectrum we use is shown in figure 12. The total flux of protons exiting the stopped target is large, with an instantaneous intensity exceeding  $10^9 \text{ s}^{-1}$ .

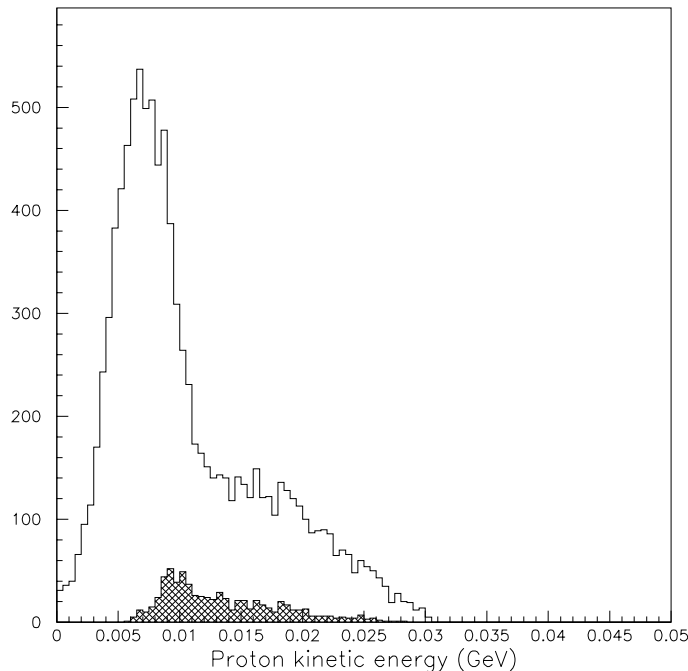


Figure 12: The distribution of the energy of protons originating from  $\mu$  capture on aluminum. The shape is from a fit to the data of reference [31]. Also shown (shaded) is the distribution of the kinetic energy of protons which cause hits in the tracking detector, showing the attenuation of low energy protons in the proton absorbers described in the text.

The tracking detector rates from these sources were estimated using the full GEANT simulation of the detector, including simulation of the detector segmentation. Photons and protons were caused to originate in the stopping target with distributions in the position of the origin appropriate to the  $\mu$  stopping distributions, and caused to emanate isotropically. The number of detector elements hit by the produced particles and their interactions in the target and detector were calculated.

The largest contribution to the rate is from protons; without shielding, the average rate in individual tracking detector elements (5 mm diameter straw tubes) is  $\sim 1.3$  MHz. However, the protons can be attenuated significantly by a set of absorbers. One is a cylindrical cone at large radii between the stopping target and detector; this upstream absorber is not intercepted by 105 MeV electrons. A downstream absorber consists of a sheet immediately upstream of the tracking detector extending radially outward from its inner radius and a cylinder extending the length of the tracking detector and immediately inside it. The tracking chamber rates were studied as a function of the thickness of these absorbers. Figure 13 shows the rate as a function of thickness for each absorber, with the other thickness fixed. Both absorbers were made of polyethylene. Based on the variation shown, thicknesses of 0.1 and 0.05 cm were chosen for the upstream and downstream absorbers, respectively. The resulting instantaneous rate is  $\sim 170$  kHz per wire. The effect of the extra material on the electron

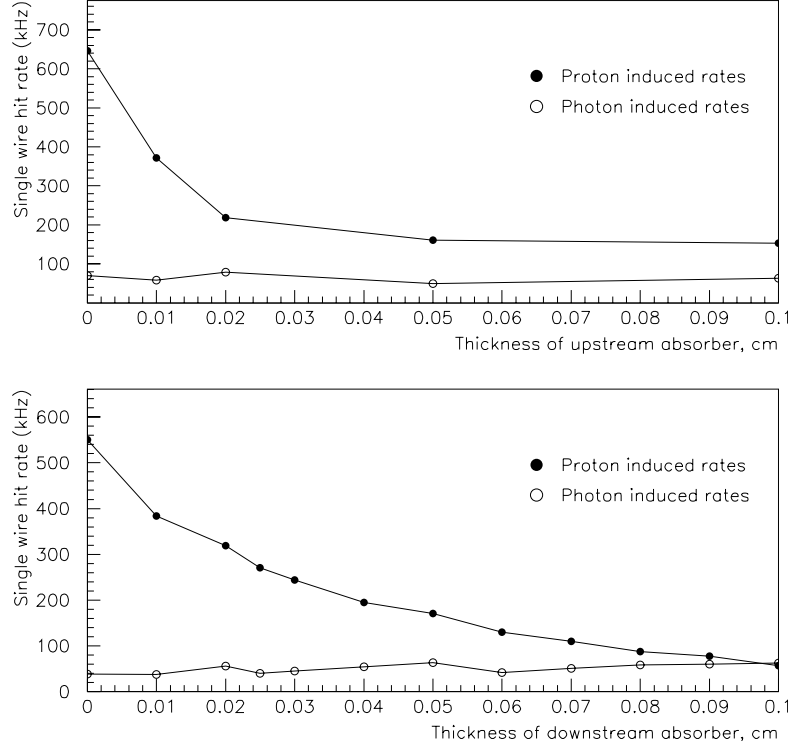


Figure 13: Plot of the mean single channel detector rates as a function of the thickness of the proton absorbers. For the upstream (cone) absorber plots. Nominal values of the thickness of 0.1 cm and 0.05 cm for the upstream and downstream absorbers, respectively, were used when studying rate as a function of the other thickness.

energy measurement is small and has been included; if rates are higher than expected, the thickness of the downstream absorber could be increased.

The protons are generally heavily ionizing. The momentum distribution of protons which hit the straws is shown in figure 12. They typically have a mean ionization rate of  $10\times$  minimum ionizing.

A similar calculation was done for photons. Figure 13 also shows the electron rate as a function of the absorber thicknesses (conversions in these could increase the rate due to photons). The simulation was done with the full detector, including the electron trigger detector, in place. With the chosen attenuator thicknesses, the rate is  $\sim 70$  kHz per detector element. The chamber hits are caused by low momentum electrons which spiral, typically hitting a straw a number of times, but within a very short time.

Finally, the rate due to the high energy tails of the  $\mu$  decay in orbit electrons was calculated. Muon decay electrons were generated with electron energy  $E_e > 51$  MeV, originating in the stopping target with a distribution appropriate for  $\mu$  stops and emitted isotropically. Nearly all the straw detector hits were in the cylinder; the mean rate of hits in these tracking detector elements due to decay in orbit electrons is 48 kHz, and the contribution to the rate

in the vanes is negligible.

The total rate per detector element is  $\sim 240$  kHz and  $\sim 300$  kHz in the vanes and cylinder, respectively. These rates are lower by a factor of 2-3 than rates in the BNL E871 straw chambers detectors of similar construction. In a 30 ns gate, typical of the drift time in the straw detectors operated with a  $100 \mu\text{m}/\text{ns}$  drift velocity gas, the average occupancy is under 1%.

## 6 Choice of Accelerator for the Experiment

Experiments using low energy  $\mu$  beams have until now been done at low energy machines (PSI, LAMPF, TRIUMF). Typically, the ratio of usable produced  $\mu$ 's to targeted protons was of order  $10^{-8}$ . Djilkibaev and Lobashev [2, 3] proposed placing the  $\pi$  production target in a graded solenoidal field and collecting  $\pi$ 's over essentially  $4\pi$  solid angle. They calculated it should be possible to produce up to  $\sim 10^{-4}$   $\mu$ 's per proton with such a scheme. Coupled with the very high currents possible at these machines, significant improvements in sensitivity could be contemplated. The Moscow Meson Factory, for which MELC was proposed, will not be able to operate enough to execute a sensitive experiment.

The TRIUMF cyclotron could plausibly accelerate sufficient protons to produce the necessary  $\mu$  flux. A preliminary design for a means of making a pulsed beam with intensity close to that required has been produced. For reasons of scheduling and resources at TRIUMF, we cannot foresee doing the experiment there in the near future.

We have been in frequent contact with members of the SINDRUM2 collaboration and with the PSI management. As discussed earlier, PSI has a planned program to reach below  $10^{-13}$  in  $R_{\mu e}$ . Further increases in sensitivity do not seem possible due to the incompatibility of pulsed beam operation with other commitments of the accelerator. We have not explored whether producing a pulsed beam at PSI is feasible.

We now know that a significantly larger ratio of usable  $\mu$ 's to targeted protons can be achieved using a higher energy (e.g. 8-20 GeV protons). The achievable flux is discussed below. While not known precisely, it is in the required range at either the AGS or at the Fermilab booster, given certain assumptions about the operating scenario.

The AGS now accelerates close to  $8 \times 10^{12}$  protons per spill per RF bucket; in our mode of operation, this would yield up to  $2.4 \times 10^{13}$  protons per 2 second cycle time at 8 GeV operation. A number of modifications to the AGS operation will be required to meet our intensity goals. They involve the following:

- Extract a beam at lower energy than normally done, in order to increase the repetition rate and decrease operating costs
- Find a means of bunched beam extraction with  $\sim 1$  MHz bunch frequency. This will possibly require changing the machine RF to have 6 or 9 bunches with every 2nd or 3rd filled. Alternatively, a barrier bucket extraction scheme could be implemented.
- Construct a new proton beam line with a secondary means of beam pulsing.
- Increase the maximum proton intensity per RF bucket to  $1.3\text{-}2.0 \times 10^{13}$  protons.

The second possibility is to use the Fermilab 8 GeV Booster. In principle, with modifications, the accelerator can produce  $5 \times 10^{12}$  protons per spill at 7.5 Hz and 50% duty cycle. This meets our requirements, and reduced intensity could be had while simultaneously operating the  $\bar{p}$  source and the 120 GeV program. As we understand things, the following modifications would be needed at the Booster:

- The magnet now have an activation which varies sinusoidally in time; the power supplies would have to be modified to run with a flat top, allowing a slow beam extraction with  $\sim 50\%$  duty factor.
- A slow beam extraction would need to be implemented.
- The beam would need to be rebunched, with 2 bunches in the revolution time of the machine.
- A suitable area would be needed to which the beam would be extracted, and sufficient space for the experiment and a secondary pulsing device would be needed.
- A suitable “supercycle” incorporating fast extraction for  $\bar{p}$  production and the 120 GeV program interleaved with slow extraction for MECO would have to be devised.
- Radiation shielding to accommodate the increased intensity would be needed.

Using the Fermilab Booster as the proton driver requires significant accelerator modifications. We believe the modifications to the AGS are simpler, cheaper, and could be implemented significantly earlier.

## 7 Pulsed Proton Beam

We have studied how the BNL proton beam can be pulsed. Recall the pulsing is intended to produce short (much less than  $\tau_\mu$ ) pulses of  $\mu$ 's separated by approximately  $\tau_\mu$ . Two possibilities exist using the AGS.

The first is to use the RF structure of the beam, and extract it bunched. The AGS has 8 RF bunches in the  $2.7 \mu$ 's revolution time. Hence, filling only two bunches would give a pulse spacing of 1350 ns. Another choice is to increase the RF frequency, put 9 bunches in the machine, and fill three of them, yielding a bunch spacing of 900 ns. Space charge effects limit the intensity per bunch to  $1 - 2 \times 10^{13}$  protons. If we could get the same total intensity in two bunches, that has significant advantages in terms of sensitivity and reduced background from late arriving  $\pi$ 's. If the intensity is limited by the bunch intensity, at present the two scenarios give the about the same sensitivity since our acceptance is about 1.5 times higher for the 1350 ns bunch spacing.

With the help of AGS personnel, we have measured [33] the performance of a bunched extracted beam. One RF bunch was filled and accelerated to 24 GeV, and extracted bunched. We measured the E871 trigger rate at various times with respect to the RF bunch. Figure 14 shows the relative intensity as a function of time with respect to the filled bunch. The extinction between bunches is below  $10^{-6}$  and in unfilled bunches is of order  $10^{-3}$ . The histogram(dots) are the results from measurements with a QVT(scalers); both were used in



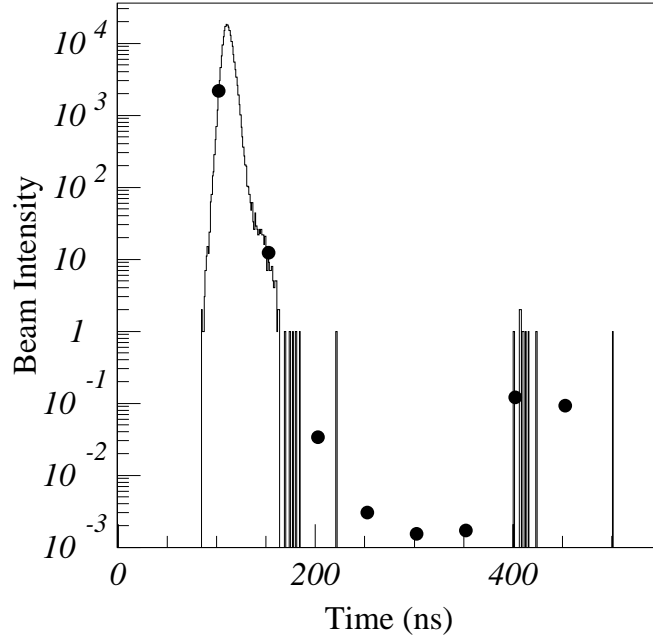


Figure 14: Plot of the beam intensity as a function of time with respect to pulses in the bunched beam extracted from the AGS.

order to get both a good measure of the main pulse shape and a good dynamic range. The extracted pulse has a width of about 30 ns.

A second way to extract a bunched beam is to use barrier RF buckets. With an unbunched beam, two empty RF buckets are produced adjacent to each other and then separated in phase, resulting in an empty region in the ring. The beam is extracted by exciting a resonance which pushes beam between the RF buckets, and then to extraction. In principle, beam is only extracted in this narrow phase in the ring. Multiple pairs of barrier buckets could be inserted in the ring if we wanted a pulse frequency different from the revolution frequency of the machine. Barrier bucket extraction has been tested at 100 MHz bunching, with pulse widths of about 400 ps achieved.

It appears likely that it will not be possible to reach an extinction below  $10^{-8}$  in the extracted beam, and we are exploring other means of reducing the off pulse rate. The preferred solution is a pulsed electric or magnetic kicker [34] in the proton transport line. The proposed device will divert an 8 GeV beam by 2.5 mrad. The beam will be focused onto a septum magnet at the end of a drift path following the kicker such that the beam could then be transported to the  $\mu$  production target during the active part of the duty cycle and dumped during the rest of the duty cycle.

The electrostatic implementation uses a potential difference of 200 kV over a 5 cm gap, for an electric field of  $E = 4$  MV/m. Electrostatic separators typically use potentials up to 500 kV over 10 cm. The device will be  $\sim 10$  m long. For a DC device 5 m long and a field of 4 MV/m, the transverse momentum is given by  $p_t = eEl/c = 20$  MeV/c, where  $e$  is the electron charge,  $E$  is the electric field, and  $l$  is the length of the device. This yields an angular kick of 2.5 mrad for a beam momentum of 8 GeV/c.

To save cost, we will drive this device resonantly using LRC circuits with large  $Q$ . In that way, no high voltage drivers are needed. The capacitor in the circuit is the pair of electrodes of the kicker. We drive a number of electrodes resonantly (with sine wave time structure) such that the sum of the  $p_t$  kicks has the correct time structure. To get an acceptable pulse shape,  $\sim 15$  harmonics of the  $\sim 1$  MHz fundamental frequency are required.

The Fourier coefficients of the 10% duty cycle rectangular wave are shown in figure 15. The length of each electrode is proportional to the magnitude of the Fourier coefficient, and

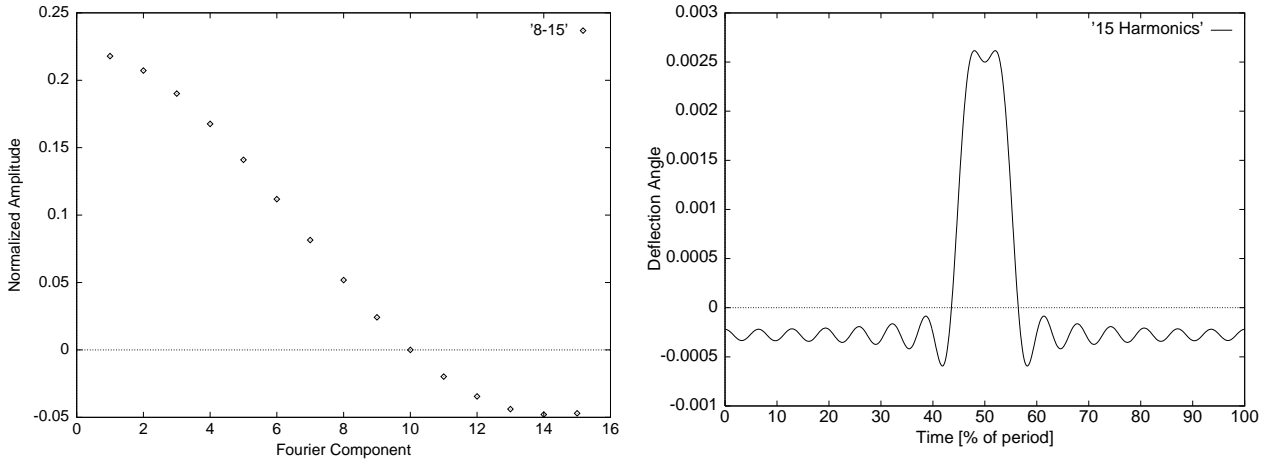


Figure 15: The left plot shows the amplitudes of the Fourier components for a 10% duty cycle square wave. Negative amplitudes indicate the component is  $180^\circ$  out of phase. The plot on the right shows, for a 15 element kicker, the angular deflection of an 8 GeV beam as a function of the time during one period of the 1 MHz pulse.

the sum over electrodes of the length times the sign of the Fourier coefficient is required to be 5 m, which yields a  $p_t$  kick of 20 MeV/c at  $t=0$ . The electrode lengths vary from 1.5 m to under 20 cm. The total length of the device, including a spacing of 10 cm (equal to twice the gap) between adjacent electrodes, is 10.14 m. To preserve the correct phasing of the Fourier components, the phase of the signal on each electrode is adjusted to account for the particle flight time.

The performance of the device was simulated by propagating an 8 GeV/c beam along the axis of the device, calculating the angular kick of each electrode, and summing the angular kicks and displacements as the particle traversed the device. Figure 15 shows the angular kick as a function of phase in the 1 MHz fundamental frequency. The electrodes are driven by LRC circuits, with the electrode forming the capacitor. The capacitances vary from 9.65 pF to under 1 pF, and the required inductors range in value from 2.63 mH to 0.13 mH. If the inductors are wound as air core solenoids, they could have resistances of a few Ohms, which would give  $Q$  values of a few thousand. Maintaining stability of the LRC circuit would be difficult, and it would probably be expedient to detune the circuit (add resistance) at the expense of increased driving voltage. For the high  $Q$  implementation, the total driver power required is under 10 kW; detuning the  $Q$  by a factor of 10 raises the power to under 100 kW.

We plan to test the effect of the kicker by tuning a secondary beam to provide a parallel transport through a kicker magnet, deflecting the beam magnetically by 2.5 mrad, focusing

the resulting beam on a septum magnet, and measuring the fraction of the beam that gets through when the beam is not diverted. The effect of tails in the beam emittance, momentum dispersion during the spill, high intensity, etc. will be measured in these tests. The effect of the pulsed extraction on the emittance will be checked by doing this with a pulsed beam and measuring the intensity as a function of time during the spill.

The conceptual design has been studied at BNL [35]. Specific suggestions have been made about the mechanical construction, for example, including the inductors inside the vacuum tank containing the kicker to avoid high voltage feedthroughs.

In addition, it has been suggested that a preferred implementation could be a pulsed magnetic kicker using the idea of a Fourier series expansion of the desired waveform and resonantly driven LRC circuits, but using stripline magnets as the inductors. Simulations have shown a central region of 4% uniformity in a circle of 1.25 cm radius, inside an aperture of  $5 \times 6$  cm. Ferrite pole pieces will be explored as a possible means of reducing the required current and increasing the size of the uniform field region. This device is described in reference [36]. This implementation has been costed at  $\sim$  \$75k per module, with  $\sim$  15 modules required.

## 7.1 $\mu$ Beam Design and Performance

An important feature of the MECO experiment is a high intensity  $\mu$  beam. The basic design of the  $\mu$  production is based on that of the MELC experiment [3]. The essential idea is to use a production target in a solenoid with a graded field. Produced  $\pi$ 's below some transverse momentum travel in helical trajectories inside the solenoid, and they will decay to  $\mu$ 's. By placing the target in a region of the field in which the axial component is decreasing in the direction of the outgoing  $\mu$  beam, the acceptance is made to extend to nearly  $4\pi$ . The  $\mu$ 's produced by  $\pi$  decay are transported in the transport solenoid to the detector solenoid, in which they are stopped and conversion electrons detected. Figure 5 shows the full set of solenoids with production and stopping targets and the detectors.

The transport solenoid has two functions: to transport the produced  $\mu$ 's to the stopping target with good efficiency and to remove unwanted particles from the beam. It [37] consists of a set of short solenoids arranged to form a straight solenoid, a bend of  $90^\circ$ , another straight section, another bend of  $90^\circ$  in the opposite direction, and a final straight section. The arrangement is shown in figure 5. In each of the straight sections is a collimator. As discussed below, this arrangement has good transport efficiency, and the collimators are used to sign and momentum select the beam.

## 7.2 The Production Solenoid and Target Performance

The use of a production target in a solenoid was first discussed in the references [2] [3] and was subsequently adopted by proponents of the muon collider [38, 39]. We will use a similar design, which places a tungsten target in a smoothly varying magnetic field; it is illuminated by a proton beam incident approximately opposite from the direction of the  $\mu$  transport direction.

### 7.2.1 $\mu$ Production

Figure 16 shows a schematic view of the production solenoid and beginning of the transport solenoid with a typical event containing a  $\mu$  produced by the interaction of a proton in the

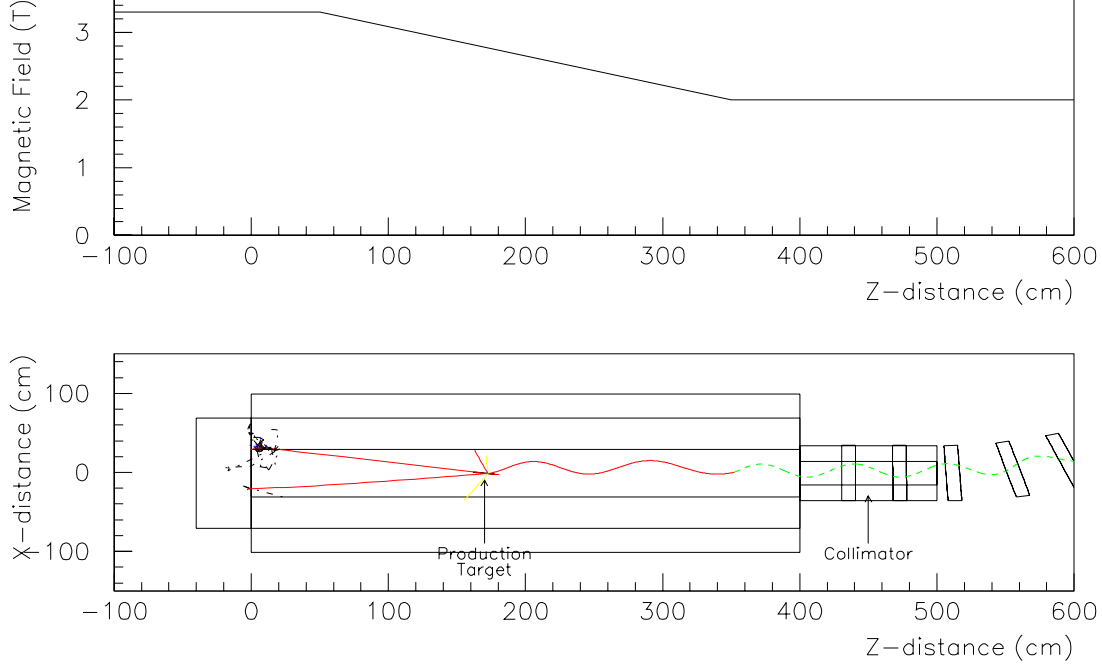


Figure 16: Schematic drawing of the production solenoid with a proton interaction producing a  $\mu$  superimposed. The incident proton beam enters from the right. Above the drawing is a plot of the axial component of the magnetic field in this region as a function of  $z$ . The horizontal scales of the two drawings are the same.

target. The axial component of the magnetic field varies smoothly from 3.3 T to 2.0 T, serving to reflect the trajectories of low momentum  $\pi$ 's and  $\mu$ 's which are generated from the tungsten target in the middle of the production region. The proton beam enters from a hole in the downstream wall of the solenoid (400 cm in figure 16); non-interacting protons exit through a larger hole in the upstream wall (0 cm in figure 16). The direction of the proton beam is opposite that of the  $\mu$  beam in order to make the construction of the exit channel and heat shielding easier.

An accurate estimate of the  $\mu$  flux is difficult to make due to lack of measurements of low energy  $\pi$  production by protons incident on heavy targets. These production cross sections are now being measured by E910 [40] at BNL. Model calculations based on FLUKA [41], GHEISHA [42], SHIELD [43], MARS [44], DPMJET2 [45], and ARC [46], disagree by a factor of 6. Figure 17 shows the predictions of the different models. We are continuing our study of  $\pi$  and  $\mu$  yields, and anticipate a better understanding of the yields when the E910 data become available. Toward that end, the NYU group is working with the E910 experimenters to speed up their analysis [47].

The yield of  $\mu$ 's depends on the target shape, the proton energy, the value of the field in the production and transport solenoids and the size of the collimators which ultimately

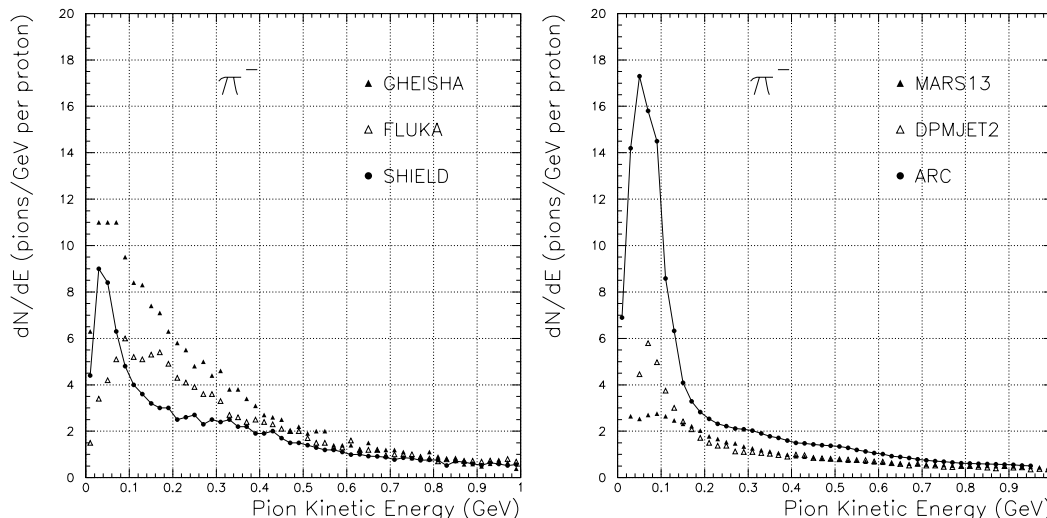


Figure 17: Predicted  $\pi^-$  yields for 24 GeV protons on mercury from six hadronic codes: GHEISHA, FLUKA, SHIELD (left) and MARS, DPMJET2, ARC (right). At low kinetic energies (of most interest to MECO), the predictions vary dramatically. Similar differences exist for 8 GeV protons on tungsten.

define the  $\mu$  beam size. We have performed preliminary optimizations of the yield as a function of these parameters [48, 49]. Given the basic shape of the target and production solenoid, several parameters were varied during simulations of the  $\mu$  yields. Some of these are shown in figure 18. Some characteristics of the particle production in the MECO setup are shown in figures 19 and 20.

The current design calls for a graded magnetic field, changing from 3.3 T to 2.0 T, a 16 cm long and 0.8 cm diameter tungsten target, rotated at  $10^\circ$  with respect to the solenoidal axis, placed at nearly the center of the graded field, and a 20 cm radius collimator at the exit of the solenoid. These values were chosen to maximize the number of  $\mu$ 's which stop in the conversion target, in the detector solenoid while minimizing the number of high energy electrons ( $> 100$  MeV). The field values were also chosen to balance a reasonable tradeoff between cost and yield. Optimization of the target radius is sensitive to the beam shape, and thus difficult to characterize until the beam emittance is accurately known. The current configuration results in 1.2%  $\mu$ 's per proton at the conversion target, of which 37% stop.

We are continuing to optimize the yields. Increases in yield may be possible with optimization of target density, collimator shapes, and conversion target location.

### 7.2.2 Target Cooling

With an incident flux of  $2 \times 10^{13}$  protons per second, the target can be radiatively cooled. We have calculated [50] that the maximum temperature is below  $2450^\circ$  K, at which temperature the target would lose 0.1% of its mass in a one year run due to evaporation.

Tungsten's high melting temperature of 3722 K allows us to use the simple technique of radiative cooling. The proton beam comes in one second bursts, every two seconds (50% duty cycle). The target is a tungsten cylinder of length 16 cm and radius 0.4 cm; total surface area

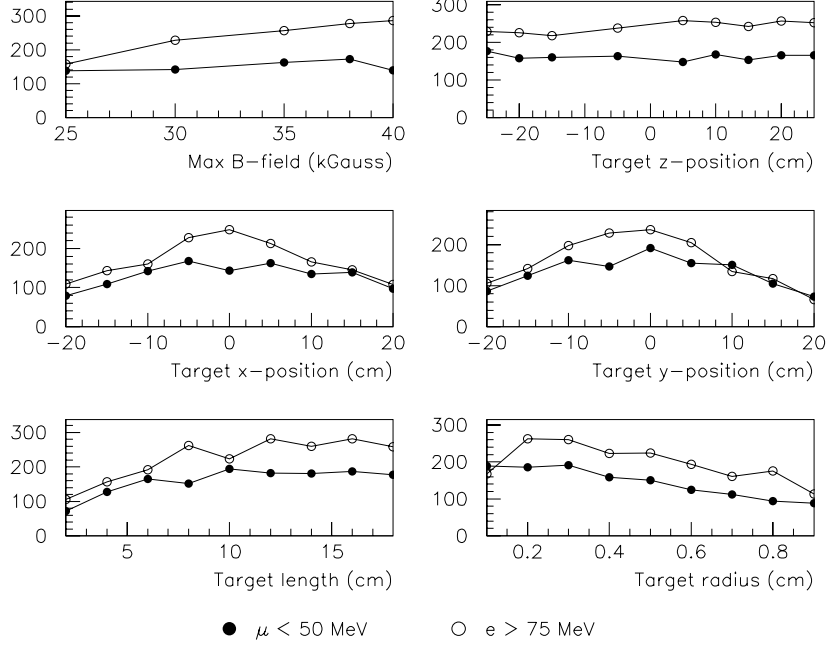


Figure 18: Some yields for  $\mu$ 's ( $< 50$  MeV) and electrons ( $> 75$  MeV) at exit of production solenoid per 10,000 8 GeV protons on target. Optimal values are chosen to be  $B_{\max} = 33$  kGauss,  $z_{\text{targ}} = 0.0$  (center of B-field variation),  $x_{\text{targ}} = y_{\text{targ}} = 0.0$ ,  $l_{\text{targ}} = 16$  cm,  $r_{\text{targ}} = 0.4$  cm.  $z_{\text{targ}}$  shows very little variation near the optimal point. For these studies, a point beam of protons was used. This affects optimization of target radius, making very small radius appear optimal.

is  $41 \text{ cm}^2$ ; mass is 155 g. To estimate target temperature, we assume that the heat conduction is sufficiently high that the target temperature is independent of radius. The temperature is then determined by two differential equations, one for the “heating stage”, when the proton beam releases power during a pulse; the other for the “cooling stage” between beam pulses.

The differential equation for “heating” is

$$C_P \frac{dT}{dt} = P - \sigma \epsilon S T^4,$$

where

- $C_P$  = the total heat capacity of the target (Joules/Kelvin),
- $P$  = peak power (Watts),
- $T$  = target temperature (Kelvin),
- $t$  = time (seconds),
- $S$  = is the target surface area ( $\text{cm}^2$ ),
- $\sigma = 5.67 \times 10^{-12}$  ( $\text{W cm}^{-2}\text{K}^{-4}$ ),
- $\epsilon \simeq 0.3$ , “blackness” degree of tungsten at  $\simeq 2500$  K.

The total heat capacity  $C_P$  for our target is  $0.132 \text{ J/g/K} \times 155 \text{ g} = 20.5 \text{ J/K}$ . The “cooling” equation is the same except that the peak power is zero.

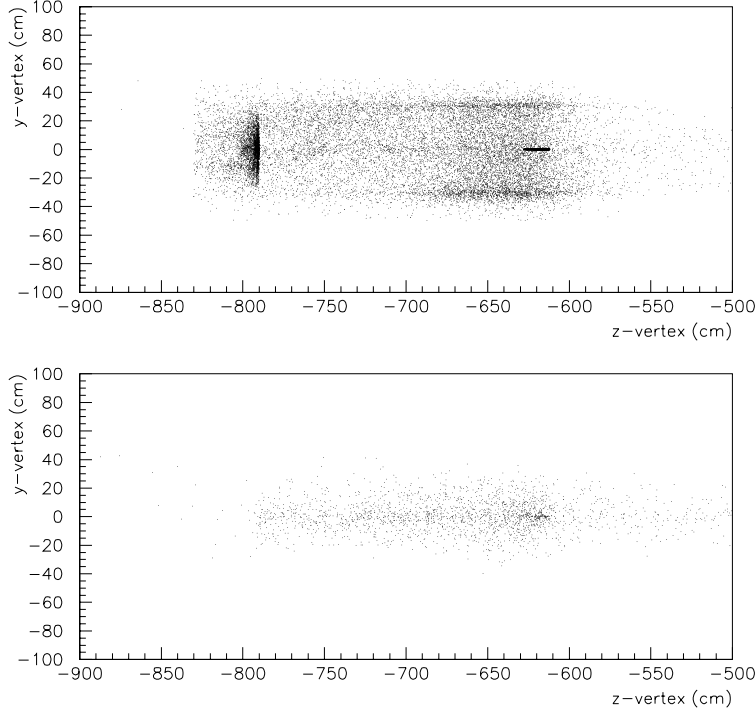


Figure 19: Location of  $\mu$  creation point in production solenoid. The top plot is for  $\mu^+$ s; the bottom is for  $\mu^-$ s. Most  $\mu^+$ s are generated in the walls of the solenoid (“surface muons”), whereas the  $\mu^-$ s come from  $\pi$  decays in flight.

Table 2 shows the GEANT [51] simulation results for average energy loss per proton and heat power release in the tungsten target by 8 GeV/c proton beam with emittance  $\epsilon_x^{95\%} =$

Table 2: Average energy loss per proton and heat power release in the tungsten target by 8 GeV/c proton beam with emittance 6  $\pi$ -mm-mrad.

Hadron Code	Average Current	Target Radius	Target Length	Average Loss	Peak Power	Average Power
GHEISHA	$2 \times 10^{13}$ p/sec	0.4 cm	16 cm	0.7 GeV	4.7 kW	2.35 kW
GHEISHA	-	-	20 cm	0.77 GeV	5.1 kW	2.55 kW
FLUKA	-	-	16 cm	0.7 GeV	4.7 kW	2.35 kW
FLUKA	-	-	20 cm	0.74 GeV	4.9 kW	2.45 kW

$\epsilon_y^{95\%} = 6$   $\pi$ -mm-mrad. For this simulation two different hadron codes GHEISHA [42] and FLUKA [41] were used. The proton beam was simulated by independent uniform elliptical distributions in  $(x, \theta_x)$  and  $(y, \theta_y)$  phase-space ( $x_{\max}=y_{\max}=3$  mm) and by requiring  $x^2 + y^2 \leq R^2$ , where  $R$ , beam radius, is 3 mm. The calculated result for average energy loss per primary proton is practically the same for these codes and equal to 0.70 GeV/proton and

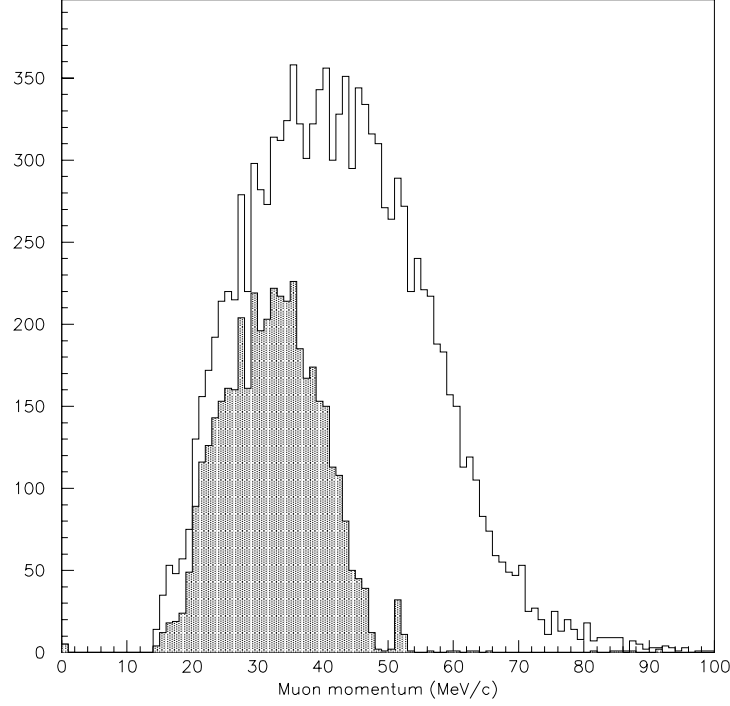


Figure 20: Muon momenta at the entrance to the detector solenoid. The shaded region corresponds to events which stop in the conversion target disks. Results are based on the GHEISHA production model for  $\pi$ 's.

0.74 GeV/proton for the target lengths 16 cm and 20 cm, respectively. This is equivalent to heat peak power 4.7 kW and 5.1 kW for target lengths 16 cm and 20 cm, respectively. The longitudinal distribution of the average energy loss per primary 8 GeV/c proton is shown in figure 21.

The differential equations can be solved analytically. The solution for the heating equation is

$$\frac{C_P T_{\max}}{2P} \left[ \frac{1}{2} \log \left( \frac{T_{\max} + T}{T_{\max} - T} \right) + \arctan \left( \frac{T}{T_{\max}} \right) \right] =$$

$$t - t_0 + \frac{C_P T_{\max}}{2P} \left[ \frac{1}{2} \log \left( \frac{T_{\max} + T_0}{T_{\max} - T_0} \right) + \arctan \left( \frac{T_0}{T_{\max}} \right) \right]$$

where

$$t_0, T_0 = \text{initial conditions,}$$

$$T_{\max} = \sqrt[4]{P/(\sigma \epsilon S)} = \text{maximum temperature.}$$

The values  $T_{\max}$  and  $C_P T_{\max}/2P$  are  $T_{\max} = 2861$  K and  $C_P T_{\max}/2P = 6.2$  seconds for the target with radius 0.4 cm and length 16 cm.



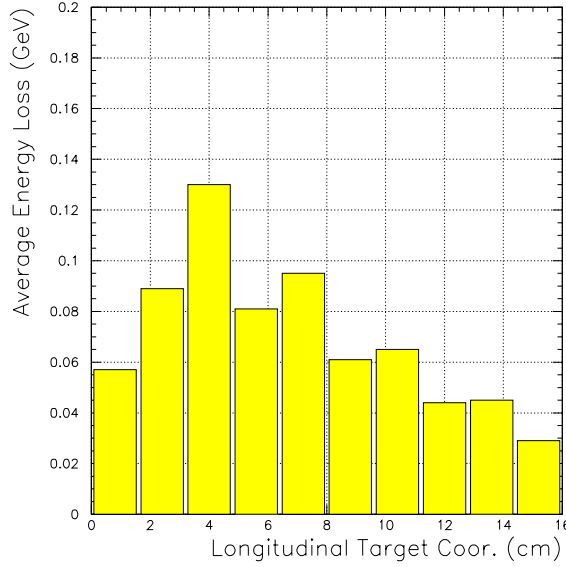


Figure 21: The longitudinal distribution of average energy loss per primary 8 GeV/c proton in the tungsten target ( $L = 16$  cm,  $r = 0.4$  cm).

The cooling equation solution is

$$T = T_0 \left[ 1 + \frac{3\sigma\epsilon S}{C_P} T_0^3 (t - t_0) \right]^{-\frac{1}{3}}$$

where  $t_0$  and  $T_0$  are initial conditions.

Figure 22 shows the target temperature rise relative to room temperature (300 K) in a 0.4 cm radius and 16 cm long tungsten target when irradiated by 8 GeV/c beam of  $2 \times 10^{13}$  protons with one second pulse and two second repetition cycle. The target temperature reaches the average temperature ( $T_e = 2430$  K) after 35 seconds in 0.4 cm radius and 16 cm long tungsten target when irradiated by 8 GeV/c beam of  $2 \times 10^{13}$  protons/second. The temperature deviation relative to the average temperature is  $\pm 60$  K. The average temperature is determined by the equation

$$\bar{T} = \sqrt[4]{\bar{P}/(\sigma\epsilon S)},$$

where  $\bar{P}$  is the average heat power.

Aging of the target is caused by tungsten evaporation from the target surface due to the high temperature. Figure 23 shows the evaporation rate as a function of temperature. At  $\sim 2500$  K, the evaporation rate is  $\sim 9 \times 10^{-10}$ . For a target of mass 155 g, surface area 41 cm<sup>2</sup>, and running time of  $10^7$  seconds, this corresponds to less than 0.25% evaporation over the course of the experiment.

### 7.2.3 Solenoid Heat Load

Heat load from the particle spray on the superconducting solenoid surrounding the production target is manageable. Results from our GEANT calculations show that a combination of copper and tungsten shielding in a cylindrical shell surrounding a 30 cm radius evacuated

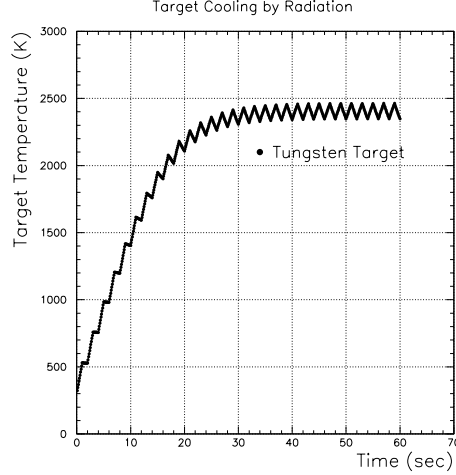


Figure 22: The target temperature rise relative to room temperature (300 K) in a 0.4 cm radius and 16 cm long tungsten target when irradiated by 8 GeV/c beam of  $2 \times 10^{13}$  protons with one second pulse and two second repetition cycle. Peak heat power releases in the target is equal 4.7 kW.

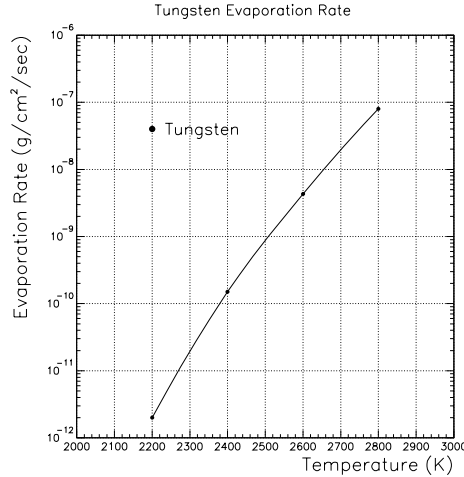


Figure 23: Dependence of evaporation rate with temperature for tungsten. Taken from reference [52].

$\pi$  decay volume would result in under 30 W deposited in a 6 cm thick coil pack outside the shield. This is deposited mainly in the region near the exit hole for the noninteracting proton beam. The higher density tungsten shielding in that region allows us to maintain the superconducting coils at a 60 cm radius.

To estimate the heat load on the coils and solenoid pole piece, a GEANT simulation was run for 8 GeV protons hitting a tungsten target inside the superconducting solenoid [53]. The solenoid was approximated by several concentric cylinders, made of copper or tungsten. One cylinder, representing the superconducting coils, was made of aluminum. A hole was placed through the end to allow non-interacting protons to escape the solenoid without interacting in the pole piece. A typical setup is shown in figure 24.

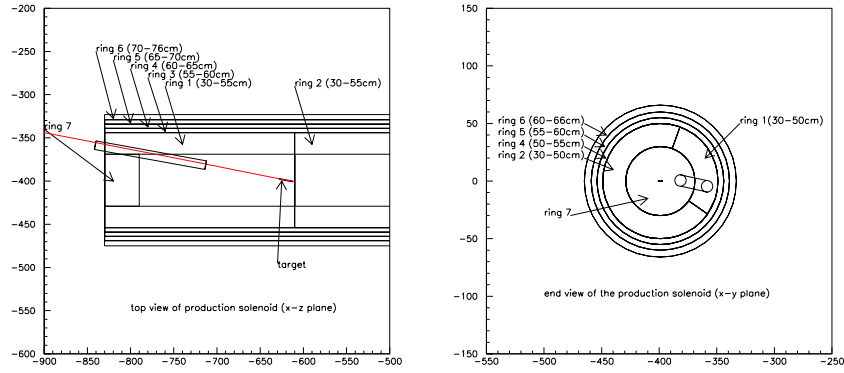


Figure 24: Geometries used in GEANT simulation for production solenoid. The line shows a sample non-interacting proton escaping out the back hole. The hole has a 5 cm radius and the target is located at  $-620.0$  cm. The view on the right shows the typical segmentations of the cylinders, to allow specific placement of materials.

Preliminary studies were performed with different hadronic codes: GHEISHA, FLUKA, SHIELD. As figure 25 shows, energy deposited in the cylinders is roughly insensitive to the particular hadronic model chosen. For the full study, only GHEISHA, the GEANT default model, was used.

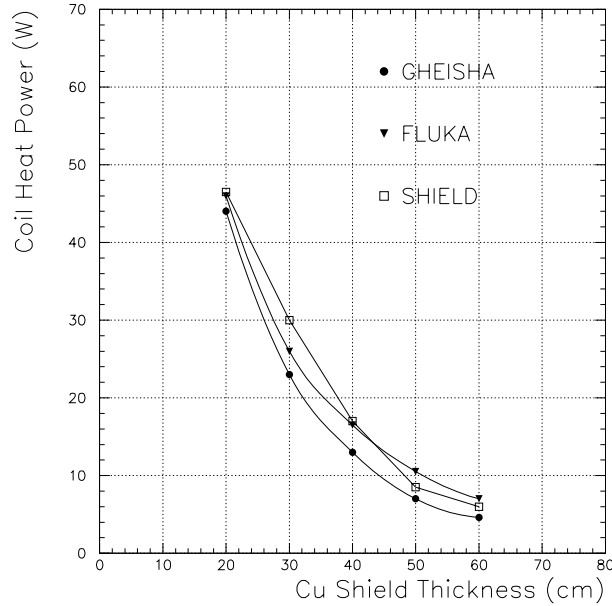


Figure 25: Power deposited in solenoid walls for different hadrons codes. All codes give approximately the same result.

The exit hole is aligned such that beam protons escape without touching the solenoid walls. Studies reveal that an exit hole of 5 cm is sufficient and necessary to minimize the contributions from the beam protons; increasing the hole radius beyond this has little effect

on the total power deposition. Various configurations of absorbers were studied with the goal of minimizing the solenoid radius while keeping the power load on the superconducting coils to under 30 Watts. We present the results of three designs here: an all-copper configuration, a copper-tungsten configuration, and a copper-tungsten configuration where the tungsten is only part of a cylinder. These are summarized in table 3. The tungsten need not cover an

Table 3: Energy deposition in 6 cm aluminum coils for three solenoid configurations. In all cases, the solenoid has an internal radius of 30 cm and a length of 440 cm. The coil radius listed is the minimum radius for the superconducting coils which will keep the power load under 30 W.

	Configuration	Power in coils	Coil radius
A	All copper	22.7 W	70 cm
B	Tungsten in innermost cylinder: 30 cm inner radius, 15 cm thick, 220 cm length.	30.9 W	60 cm
C	Partial tungsten in innermost cylinder: $-120^\circ$ to $125^\circ$ 30 cm inner radius, 20 cm thick, 220 cm length.	30.3 W	60 cm

entire cylinder because the energy deposited is not uniform over the surface of a cylinder, as seen in figure 26. The material requirements for each design are summarized in table 4

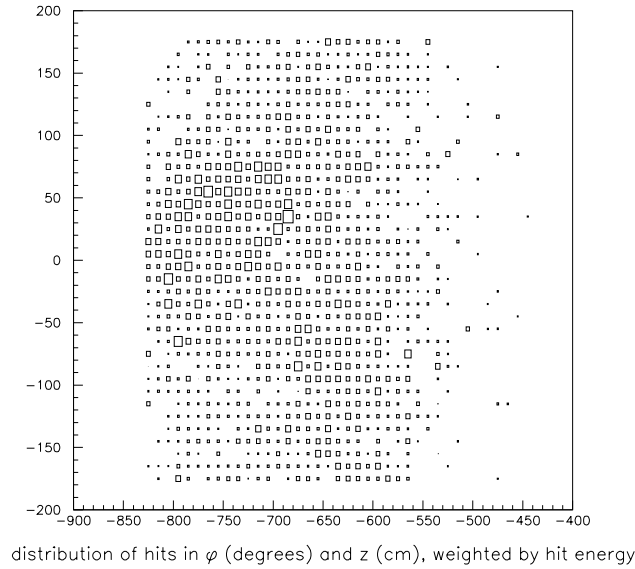


Figure 26: Angular and axial dependence of power deposited in solenoid walls for configuration B.

below. In all cases, the power load on the coils can be maintained below 30 W. The trade-off is between solenoidal radius and amount of tungsten.

Table 4: Mass and volume of Tungsten (W) and Copper (Cu) for the three shielding configurations.

	volume of W	mass of W	volume of Cu	mass of Cu
A	0	0	$5.53 \times 10^6 \text{cm}^3$	$4.95 \times 10^7 \text{g}$
B	$7.775 \times 10^5 \text{cm}^3$	$1.50 \times 10^7 \text{g}$	$2.96 \times 10^6 \text{cm}^3$	$2.65 \times 10^7 \text{g}$
C	$7.526 \times 10^5 \text{cm}^3$	$1.45 \times 10^7 \text{g}$	$2.98 \times 10^6 \text{cm}^3$	$2.67 \times 10^7 \text{g}$

### 7.3 The Transport Solenoid

Muons are transported from the production solenoid to the detector solenoid using a curved solenoid bent first by  $90^\circ$  in one direction, and then  $90^\circ$  in the opposite direction. The purpose of the bends is to decrease the transmission of both high momentum particles and positive particles. Unwanted particles are absorbed in appropriately shaped collimators at the ends of the transport and at the center.

An initial design [37] of the solenoid uses 54 “coil packs” to contain the coil windings, each maintaining enough current to produce 2 T uniformly in the solenoid (approximately 6.8 kA). The coil packs are each  $\sim 18$  cm long and  $\sim 70$  cm in diameter, and are modeled with Russian superconducting cable consisting of 8 wires of PSNT-0.85 superconductor embedded in a  $1.0 \times 9.0 \text{ mm}^2$  aluminum cable. The cables wind in three layers with 35 turns of cable each, depending on the insulation between each layer. The packs are arranged in the curved configuration with appropriate gaps for mechanical considerations. The basic construction is shown in figure 27.

The magnetic field was calculated exactly using the law of Biot and Savart, then used in GEANT simulations to accurately estimate the effects of different collimator settings. The field map reveals that there are small ripples at large radii due to discontinuities in the coil packs. For the region with radius less than 25 cm, the ripples are sufficiently small so as not to affect the transport.

Charged particles of sufficiently low momentum follow helical trajectories centered on magnetic field lines. In a torus, they drift in a direction perpendicular to the plane of the torus, by an amount given by  $D = 1/0.3B \times s/R \times (p_s^2 + \frac{1}{2}p_t^2)/p_s$ , where  $D$  is the drift distance,  $B$  is the magnetic field,  $s/R$  is the bend angle of the solenoid, and  $p_t$  and  $p_s$  are the perpendicular and parallel momentum components. For  $s/R = \pi/2$ ,  $p_t = 0.09 \text{ GeV}/c$ ,  $p_s = 0.12 \text{ GeV}/c$ , and  $B = 2 \text{ T}$ , the drift of the center of the helix is 49 cm. The drift direction depends on the charge. Hence, by putting appropriate collimators in the straight sections, positive particles can be absorbed as can negative particles of high momentum. The drift effect in the trajectory is illustrated in figures 28 and 29. The curved solenoids and collimators have been simulated in the GEANT calculations used to estimate  $\mu$  stopping rates and backgrounds.

Cylindrical collimators are placed in the first and last straight sections (regions 1 and 5 with inner radii  $r_1$  and  $r_5$ ) and in the center straight section (region 3 with inner radius  $r_3$ ). In addition, collimators in the central straight section restrict the coordinate perpendicular to the plane of the transport ( $y$  coordinate with  $y_{min}$  and  $y_{max}$ ), so as to absorb positive particles and high energy negative particles. A sketch of the collimators is shown in figure 30.

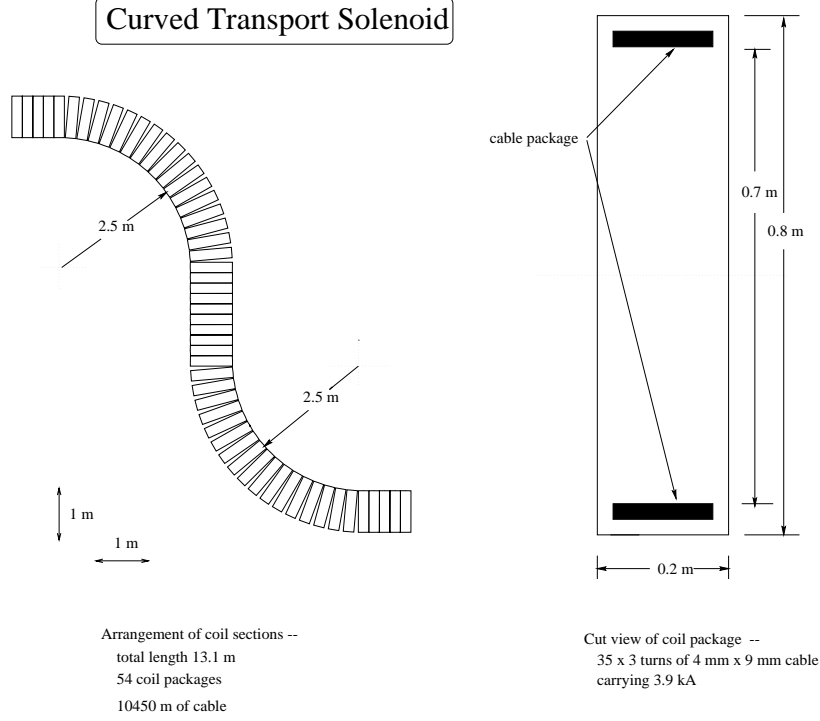


Figure 27: Sketch of transport construction. Solenoid is composed of 54 coil packages.

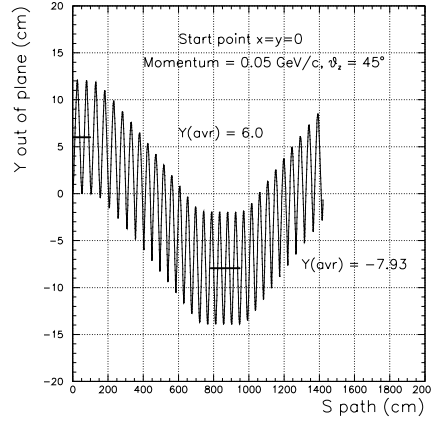


Figure 28: Simulated trajectory in central region of transport for typical  $\mu$ . A downward drift can be seen, caused by the electron's negative charge in the toroidal field.

The collimator sizes are optimized to remove all electrons above 100 MeV. To determine these parameters, a GEANT simulation of  $10^7$  protons was run, and the electrons which made it through the transport recorded. Values of  $r_1 = r_5 = 20 \text{ cm}$ ,  $r_3 = 25 \text{ cm}$ ,  $y_{\min} = -19 \text{ cm}$  and  $y_{\max} = 5 \text{ cm}$  completely eliminated 100 MeV electrons. Figure 31 shows how the circular collimator in region 5 and the collimator in region 3 restricting  $y_{\min}$  remove the last few 100 MeV electrons from the sample. This calculation is statistics limited. Other studies showed that no electrons with energy greater than 100 MeV which are produced in

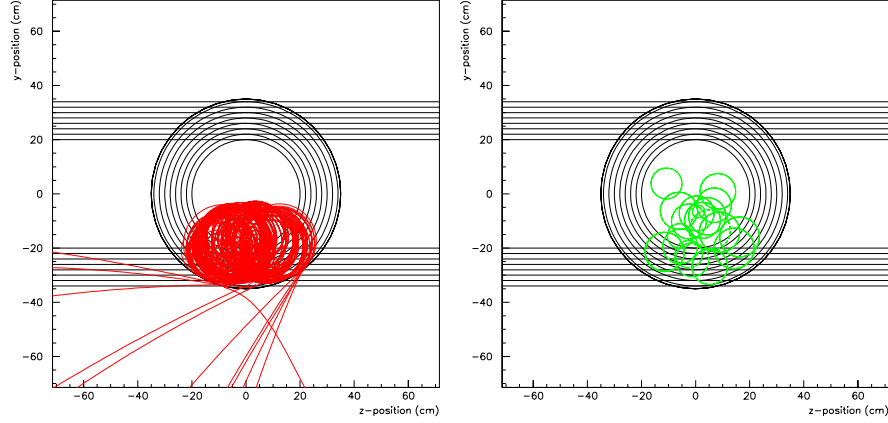


Figure 29: Trajectories in the straight region after the first  $90^\circ$  bend of the transport, looking along the solenoid direction. The left side is electrons with  $E_e > 75$  MeV; the right side is  $\mu$ 's with  $E_\mu < 40$  MeV.

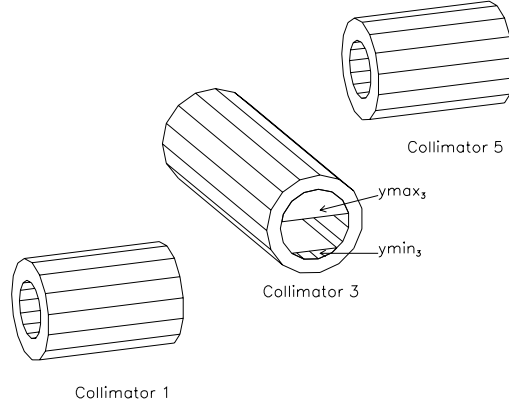


Figure 30: Sketch of the three collimators in the transport solenoid.

the production solenoid and don't scatter in the transport solenoid pass the collimators.

Figure 32 shows the spectrum of charged particles at the transport solenoid exit for the nominal collimators, and also for a more restrictive set. Both sets remove high energy electrons, but high energy  $\mu$ 's appear to need tighter collimators. The precise implementation of collimators to remove positive and high momentum negative particles is still being optimized.

## 8 The MECO Detector

An experiment to reach the design sensitivity must deal with the high rates discussed earlier and achieve excellent energy resolution. We propose a solenoidal spectrometer, differing from that of SINDRUM2 in that the detection apparatus is displaced downstream along the incident  $\mu$  direction from the stopping target. This reduces the solid angle subtended by the detector for photons and neutrons produced in the target. The stopping target is placed in a region of the solenoid where the axial field component is decreasing linearly with

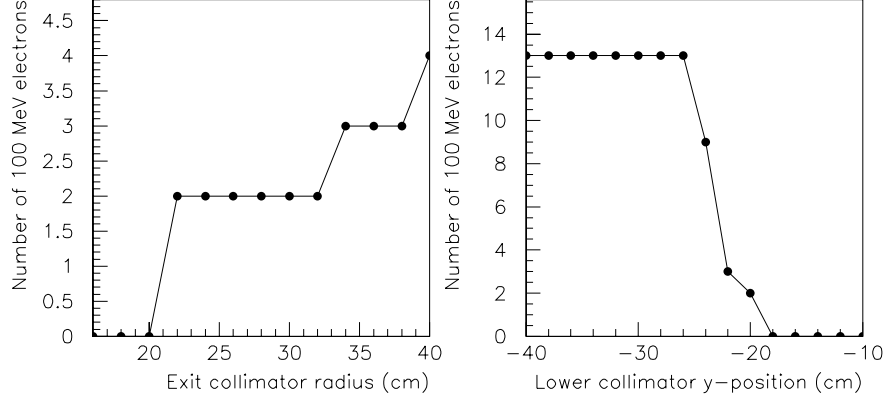


Figure 31: Required values of collimator bore size and height to remove high energy electrons. Each of the other collimator parameters is set to its nominal value as stated in text. This sample of electrons represents  $10^7$  protons on the production target.

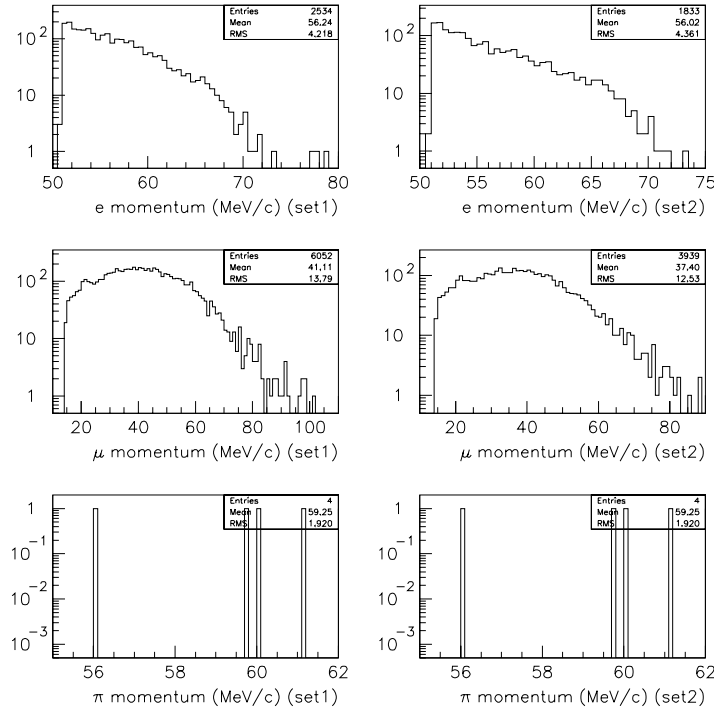


Figure 32: Momentum spectra for e,  $\mu$ ,  $\pi$  at the exit of the transport solenoid for two sets of collimator settings. The plots on the left are for the standard collimator set discussed in the text. The plots on the right have  $r_1$  and  $r_5$  set to 15 cm. These plots are for  $5 \times 10^5$  simulated proton interactions.

position along the solenoid, and the tracking detector is downstream of it, in a constant field



region. All electrons with production angles between  $60^\circ$  and  $120^\circ$  with respect to the beam direction will enter the detector region with approximately the same helical pitch, of about  $50^\circ$ . This is not true of electrons produced at other positions (from the entrance face of the detector solenoid, for example), and hence these do not contribute to background.

The process of choosing the transverse size, thickness and position of the stopping target and tracking detector involves variations of these parameters in order to optimize acceptance, rates, and rejection of physics backgrounds. Aspects of this optimization are discussed in various sections to which we refer at the appropriate time.

## 8.1 The Detector Solenoid

The detector solenoid with stopping target, tracking detector, and trigger detector is shown in figure 33. It consists of a 10.5 m long solenoid of radius  $\sim 0.9$  m. The axial component of

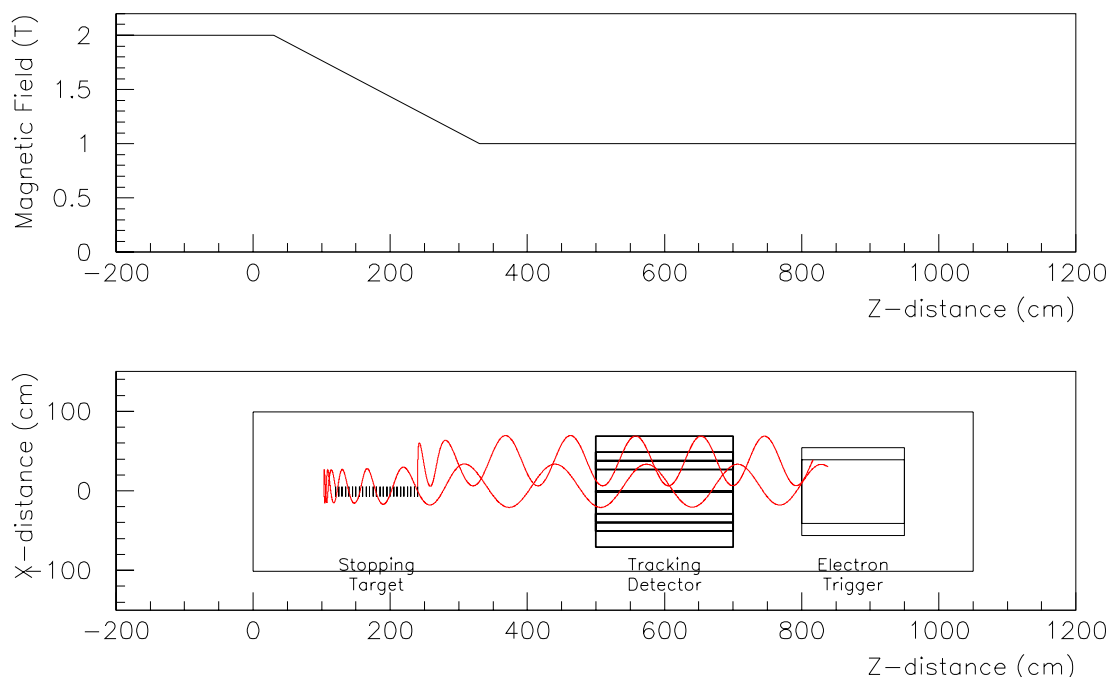


Figure 33: Schematic drawing of the detector solenoid with stopping target, tracking detector, and electron calorimeter. The axial component of the magnetic field as a function of distance along the solenoid is also shown, on the same horizontal scale.

the field varies with distance along the solenoid; this variation is also shown in figure 33.

The magnetic and cryogenic design of the detector solenoid has not been done. The parameters of this magnet are similar to that of the MELC proposal [3] and a design is discussed in that document. We include a cost based on scaling arguments in the section on costs.

## 8.2 The Stopping Target

The stopping target is designed to maximize the stopping rate and the signal electron acceptance into the detector. Increasing the target size and total thickness improves the stopping rate, but decreases the acceptance because of the larger energy loss dispersion in the target. Further, reducing detector rates is a concern; these rates are directly proportional to the  $\mu$  stopping rate and depend less strongly on the detector acceptance.

Variations of target parameters were made about initial values of 25 layers of aluminum, each 0.02 cm thick, with radius 6.53 cm and distance between layers 5 cm. The target resides in a B field varying between 1.3 T and 1.7 T. In this configuration, 39% of the  $\mu$ 's stop. The stopping distribution is peaked at the upstream end as shown in figure 34 for a target with fewer layers. Reducing the number of target layers does not significantly decrease the

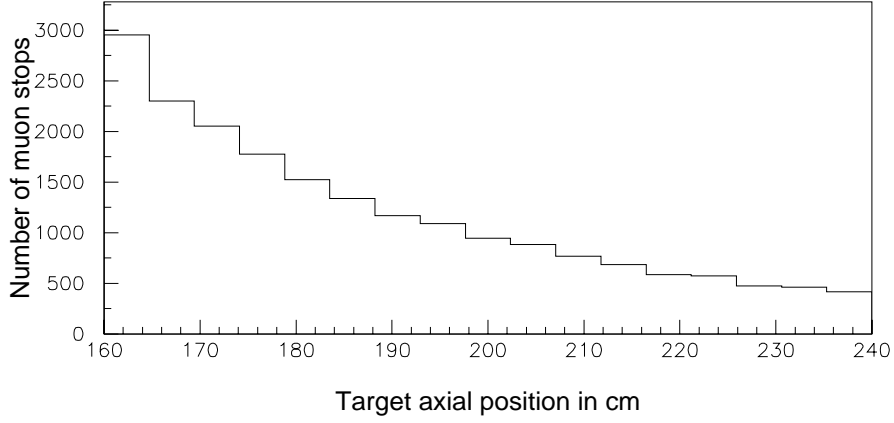


Figure 34: The distribution in the axial stopping position of  $\mu$ 's for the optimal target setting with 17 layers between 1.57 T and 1.3 T, with target radii of 8.3 cm at 1.57 T and 6.53 cm at 1.3 T.

stop rate, while reducing the energy loss dispersion in the target and improves the electron momentum measurement and hence reduces the background from  $\mu$  decay in orbit. The number of target layers and the target center position are varied to study the product of the  $\mu$  stopping probability and detector acceptance. Table 5 shows that reducing the number of disks to 17 yields a larger value for the product of the stopping rate and acceptance.

Another important consideration in the target and detector design is to limit the acceptance for electrons from  $\mu$  decay in orbit. The energy below which no electrons produced in the stopping target hit the detector depends on the target radius, the inner diameter of the tracking detector, and the ratio of B field values at the target and the detector. This relationship can be worked out using the fact that in an axially graded magnetic field the transverse momentum varies with axial coordinate, with  $p_T^2/B$  constant. Also, R, the distance from the helix center to the axis of the solenoid varies with axial coordinate, with  $R^2 \times B$  constant. The cut-off energy decreases with increasing B field value at the target for a given target radius and detector inner diameter. For a target radius 6.53 cm, the

Table 5: Comparison of performance between 17 and 25 target layers with radius 6.53 cm and the most downstream layer both at 1.3 T, with upstream end of the target at 1.57 T and 1.7 T, respectively.

# of layers	radius	$e^-$ cut-off energy	stop rate	acc.	stop rate $\times$ acc.
25	6.53 cm	56 MeV	39.4%	20.0%	7.87%
17	6.53 cm	56 MeV	31.1%	26.9%	8.36%

electron cut-off energy is given by the most downstream target layer at 1.3 T, yielding 56 MeV. Increased stop rate can be achieved by increasing the target radius at higher B field, to maintain the same cut-off energy. This criterion gives a target radius of 6.53 at 1.3 T and 8.3 cm at 1.57 T. Table 6 shows comparison of performance for various number of target layers, all with the downstream end of the target at 1.3 T. The optimal choice is again 17

Table 6: Comparison of performance for various number of target layers, all with the most downstream end of the target at 1.3 T. In each case, the target radius varies with position to keep the electron cut-off energy constant.

# of layers	$e^-$ cut-off energy	stop rate	acc.	stop rate $\times$ acc.
21	56 MeV	42.9%	20.8%	8.91%
19	56 MeV	40.0%	22.9%	9.12%
17	56 MeV	36.9%	24.9%	9.14%
15	56 MeV	33.5%	26.8%	8.98%
13	56 MeV	29.9%	29.0%	8.69%

layers, and yields a 10% improvement in the product of stopping rate times acceptance with respect to a constant radius target.

We have also studied the effect of increasing the target radius from 6.53 cm to 7.53 cm at 1.3 T for the 17 target layer case. The stopping rate increases by 13%, and the acceptance decreases by 8%, leaving a gain of 5% in the product. However, this reduces the electron cut-off energy by 2 MeV and increases noise rates substantially for small gain in sensitivity.

We take the baseline target to be 17 layers extending between 1.57 T and 1.30 T with target radius between 8.3 and 6.53 cm. The electron cut-off energy for hitting the tracking detector is 56 MeV. Figure 34 shows the distribution of the stopped  $\mu$ 's along  $z$  for this optimal target setting, showing that more  $\mu$ 's are stopped upstream than downstream.

Moving the target downstream also helps the acceptance. With the target at lower B field, the electrons have larger  $p_t$  at the detector. The disadvantage is that, in order to maintain the same cut-off energy, the target radius must be smaller, and hence the stopping fraction decreases. The solid angle for photons to hit the detector is also increased. Table 7 shows comparison of performance for various number of target layers, with the most downstream

end of target all at 1.17 T instead of 1.3 T. For each target setting the target radius increases

Table 7: Comparison of performance for various number of target layers, with the most downstream end of target all at 1.17 T. In each target setting, the target radius increases upstream to keep the electron cut-off energy constant with  $z$ .

# of layers	$e^-$ cut-off energy	stop rate	acc.	stop rate $\times$ acc.
21	56 MeV	35.4%	30.6%	10.8%
19	56 MeV	32.5%	32.3%	10.5%
17	56 MeV	29.5%	33.8%	9.96%
15	56 MeV	26.2%	35.6%	9.32%
13	56 MeV	22.9%	36.9%	8.41%

upstream to keep the electron energy cut-off constant. The product of stop rate times acceptance increases by 18% by moving downstream and increasing the number of target layers to 21. Simulations show that in this case, less than 4% of the signal electrons will hit a single straw more than twice. In the worst case, one can always throw away those events if multiple hits in one straw presents a problem. The noise rate caused by photons increases nearly 50% in this case. This can be addressed by moving the detector downstream. We will continue the target optimization, but take the baseline design as stated above, as it has been more thoroughly studied.

### 8.3 The Tracking Detector

The goal for the tracking detector is to measure with good efficiency the parameters of the helix trajectory of electrons.

Simulations show that the precision of the radius measurement is dominated by multiple scattering. To minimize the effects of multiple scattering on the resolution, Detectors are optimally positioned at three points along the helix, with the first and last separated by  $180^\circ$  in the helical trajectory. We require more than three hits in order to provide a constraint to the helical fit. Our detector geometry consists of a cylinder of tracking detectors with 8 equally spaced *vanes* of detectors projecting radially outward from the cylinder. All individual detector elements are oriented in the axial direction.

The cylinder diameter is chosen consistent with the rate considerations discussed above, and on average, one half a helical turn is inside the cylinder and one half is outside it. Typically, one or two vanes are intercepted by a signal electron. To set the scale of the trajectories, figure 35 shows a cross section of the detector with three circular trajectories superposed. The transverse momenta of these trajectories (referenced to the stopping target position) are 55 MeV/c (the momentum exceeded by only 0.3% of decay in orbit electrons), 91 MeV/c (the transverse momentum of a conversion electron emitted at  $60^\circ$ ), and 105 MeV/c. The cylinder radius is 41 cm, the vanes extend radially for 30 cm, and the physical target radius shown is 6.5 cm.

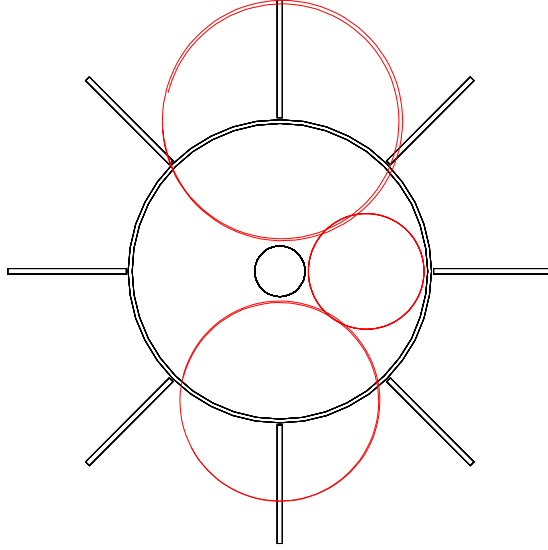


Figure 35: A cross section of the detector, effective target size, and trajectories for electrons created in the target with transverse momentum of 55, 91, and 105 MeV/c. The trajectories are shown in the region of the detector and are positioned to show the minimum allowed inner radius to keep rates from  $\mu$  decay in orbit manageable, and the detector required to have good acceptance and resolution for conversion electrons. The cylindrical part of the detector has radius 38 cm.

The baseline design of the detector has detectors consisting of 5 mm diameter straw tubes. Both the cylinder and the vanes have three layers of axially oriented straws. The straws have wall thickness  $25\ \mu\text{m}$  and are constructed of kapton. The axial coordinate will be measured by capacitive coupling to foils on the outsides of the three layer array on both the vanes and the cylinder. For multiple scattering calculations, we assume  $25\ \mu\text{m}$  foils on both sides of all detectors, with an extra pair of foils on the vanes to serve as signal traces for the pads on the cylinder. For purposes of acceptance, resolution, and background rate calculations, we assume the gas manifold and straw mounting fixtures on each end of the straws can be made of beryllium with  $2\ \text{gm}/\text{cm}^2$  thickness in the axial direction and a width perpendicular to the straws of 2.0 cm. Straws similar to these have been successfully used in BNL experiments E871 and E935, and capacitive pad readout has been demonstrated by a group at Princeton, as discussed below. The full magnetic volume from the production target through the detector solenoid is evacuated.

The baseline design has a tracking detector length of 2 m. There is little gain in acceptance or resolution with a 2.5 m long detector, and the acceptance is cut in half with a 1.5 m long detector.

In addition to the baseline detector design, an alternative design has been studied in which the cylinder is made of a 0.5 mm thick carbon fiber cylinder supporting 4 layers of 0.5 mm diameter scintillating fibers, arranged in pairs at small angle stereo, to get the axial coordinate [23]. This design is easier to manufacture, but there is more scattering and energy loss in the cylinder, which makes the energy reconstruction more difficult. The performance of both detectors will be discussed in the following sections.

### 8.3.1 Tracking Detector Performance Analysis

A full GEANT simulation of the target and detectors was done [24]. It incorporated the full Moliere scattering formalism and Landau fluctuations in the energy loss. It also incorporates Gaussian measurement errors with  $\sigma_x$ ,  $\sigma_y$  and  $\sigma_z$  to be 0.2 mm, 0.2 mm and 1.4 mm, respectively. The same spatial resolution is used for both straws and fibers, and is easily achieved in both technologies. This simulation generated electrons originating in the target with the appropriate distribution of  $\mu$  stopping positions, and exiting the target isotropically. All hit positions in the detector in multiple turns were recorded, and correctly ordered to be later used for energy reconstruction. Figure 36 shows a few typical events in the simulation.

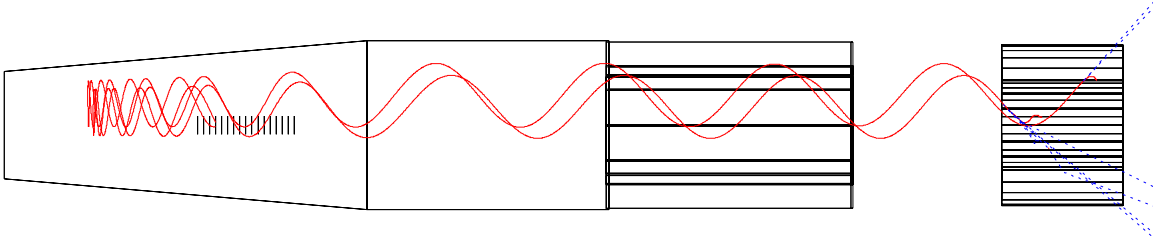


Figure 36: Two sample trajectories from the GEANT simulation.

The number of times the electron helix trajectory turns within the detector region is determined by its pitch angle and the detector's length. Figure 37 shows the  $p_t$  distribution at the detector entrance for 105 MeV electrons generated at the target. Due to the restricted

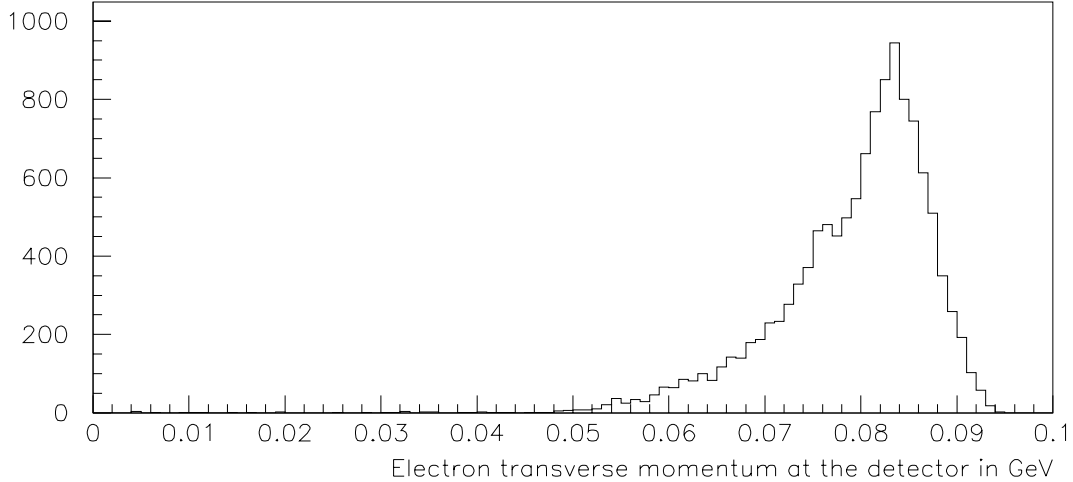


Figure 37:  $p_t$  distribution of 105 MeV electrons generated at the target at the detector entrance from the GEANT simulation.

range of  $p_t$ , most of them make between 1.4 and 1.8 turns in the detector, leaving between 5 and 8 hits in total. Figure 38 shows the distribution of total number of hit as well as the number of hits in a single turn in the detector. About 20% of the electrons have three hits

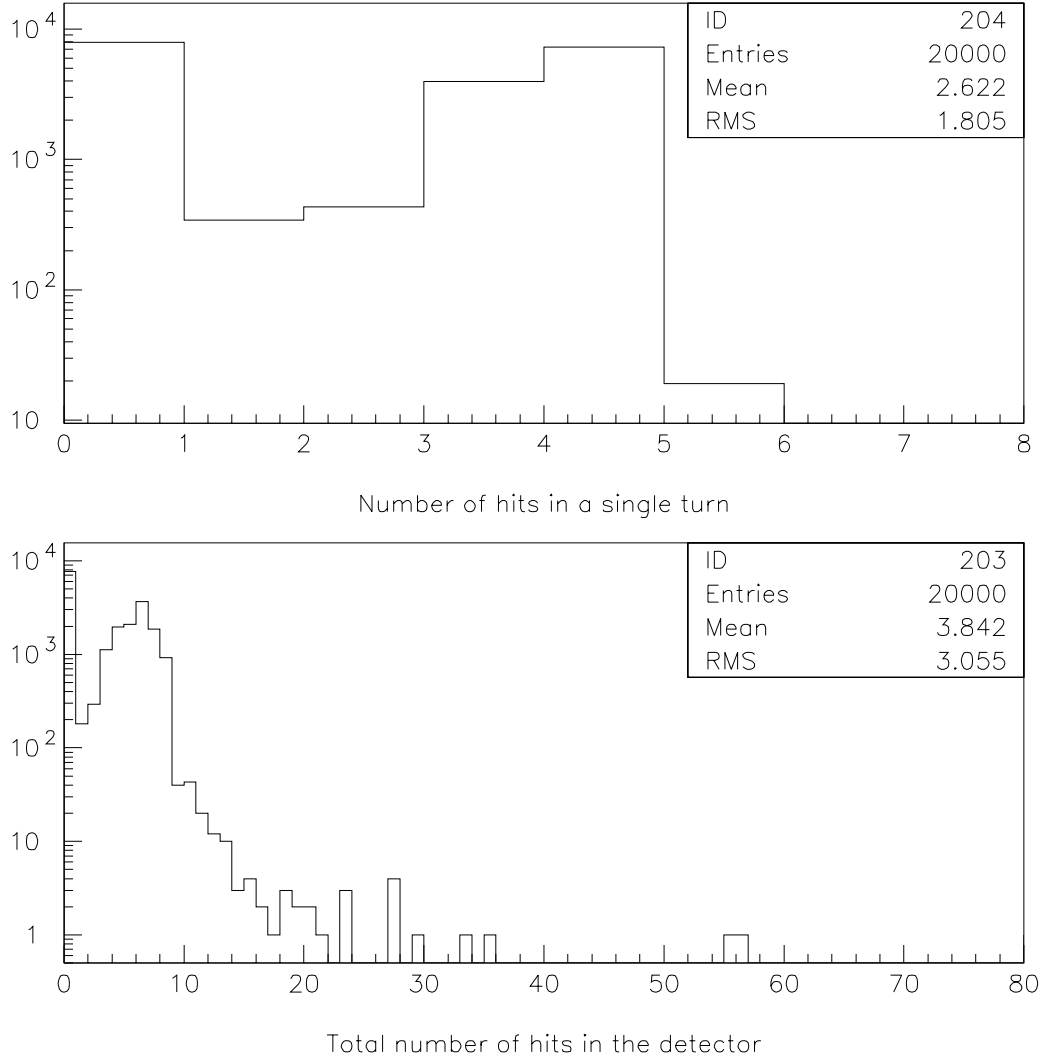


Figure 38: The distribution in the number of hits in a single turn and the total number of hits in the detector, for 105 MeV electrons generated isotropically at the target. The result is from the GEANT simulation.

in a single turn, and 37% have four hits in one turn. A total of 59% of the electrons have at least one hit in the detector. The total number of hits peaks at 6. A very small fraction of events have up to 60 hits, that is due to a significant energy loss or large angle scattering in passing one of the detector elements.

To ensure that the events have well measured trajectories, only events with at least 3 hits in a single turn were accepted. In addition, at least four total hits were required to make a reliable fit of the trajectory. A minimum transverse momentum of the electron of 75 MeV/c was also required to reject possible electron background coming from the transport system.

This also minimizes background from beam electrons scattering in the target, as discussed in the section on backgrounds. This cut has an efficiency of 80%. About fifty percent of the generated events satisfy the above requirements and are passed to a fitter for energy reconstruction.

The energy can be reconstructed by reconstructing the helix trajectory of the electron in the detector. The difficulty is that the electron's trajectory deviates from a helix due to multiple scattering. A fitting procedure taking into account the error correlations between hits, using an error matrix would account for the effects of scattering. However, the elements of this error matrix strongly depend on the trajectory, complicating this method of analysis.

Different fitting algorithms have been studied and the fitter performance has improved steadily with better energy resolution and significant reduction in the high energy tails. The current fitter works on the principal of the maximum likelihood method. Here we briefly describe this method, under the simplified assumption that the deviation from helix trajectory only comes from multiple scattering. We note that although the entire electron trajectory is no longer helix due to multiple scattering, the individual segments between neighboring hits are. For each event, this method determines the trajectory of the individual segments as a function of the electron momentum  $p_e$ , and it then defines a likelihood value  $L(P_e)$  as a function of  $p_e$  simply as the product of the scattering probability at each detector position:

$$L(P_e) = f_2(\theta_2)f_3(\theta_3)...f_{n-1}(\theta_{n-1}) \quad (1)$$

where  $n$  is the total number of hits and  $f_i(\theta)d\Omega$  is the probability that the particle scattered into the solid angle  $d\Omega$  at  $\theta$  in the detector element where the  $i$ th hit was recorded. The parameter  $f(\theta)$  takes Gaussian form for small angles and has Moliere tails for large scattering. In this case, the value of  $p_e$  is simply that which maximizes the likelihood. It is also possible to incorporate energy loss and the detector spatial resolutions in equation 1. More discussions on this subject can be found in reference [24].

To estimate the error on the value of  $p_e$  from the fitter, we fit the likelihood versus  $p_e$  in the region of the peak with a Gaussian form; denoting the  $\sigma$  of this fit as  $\sigma_{pe}$ . This gives a good estimate of the uncertainty in the measured  $p_e$ . The parameter  $\sigma_{pe}$  is found to be a powerful discriminant against events with badly fit trajectories.

In principal,  $\sigma_{pe}$  should be the sole figure of merit in determining  $p_e$  in a noise free environment such as in the GEANT simulation. However, we also cut on the likelihood value  $L$ , to ensure that no large angle scattering has occurred, for which the value of  $f(\theta)$  in equation 1 may not be accurate. For this purpose, we have chosen a very modest cut on  $L$  which removes only 2% of the events. A more useful cut in eliminating high energy tails is  $\sigma_{pe}$  and one expects to see a direct correlation between the uncertainty in energy reconstruction and the value of  $\sigma_{pe}$ . Figure 39 shows the error in the measured energy as determined by the likelihood function for various choice of the value of the  $\sigma_{pe}$  cut. It is based on the full GEANT straw detector simulation with the energy loss in target and the detector spatial resolutions included, and with all other cuts mentioned above imposed at fixed values. As the cut on  $\sigma_{pe}$  is relaxed, the energy resolution worsens with more high energy tails present. We have chosen a  $\sigma_{pe}$  cut of 500 keV, which maximize the acceptance while maintaining discrimination against high energy tails in the resolution function. The cuts on  $L$  and  $\sigma_{pe}$  have a combined acceptance of 85%.



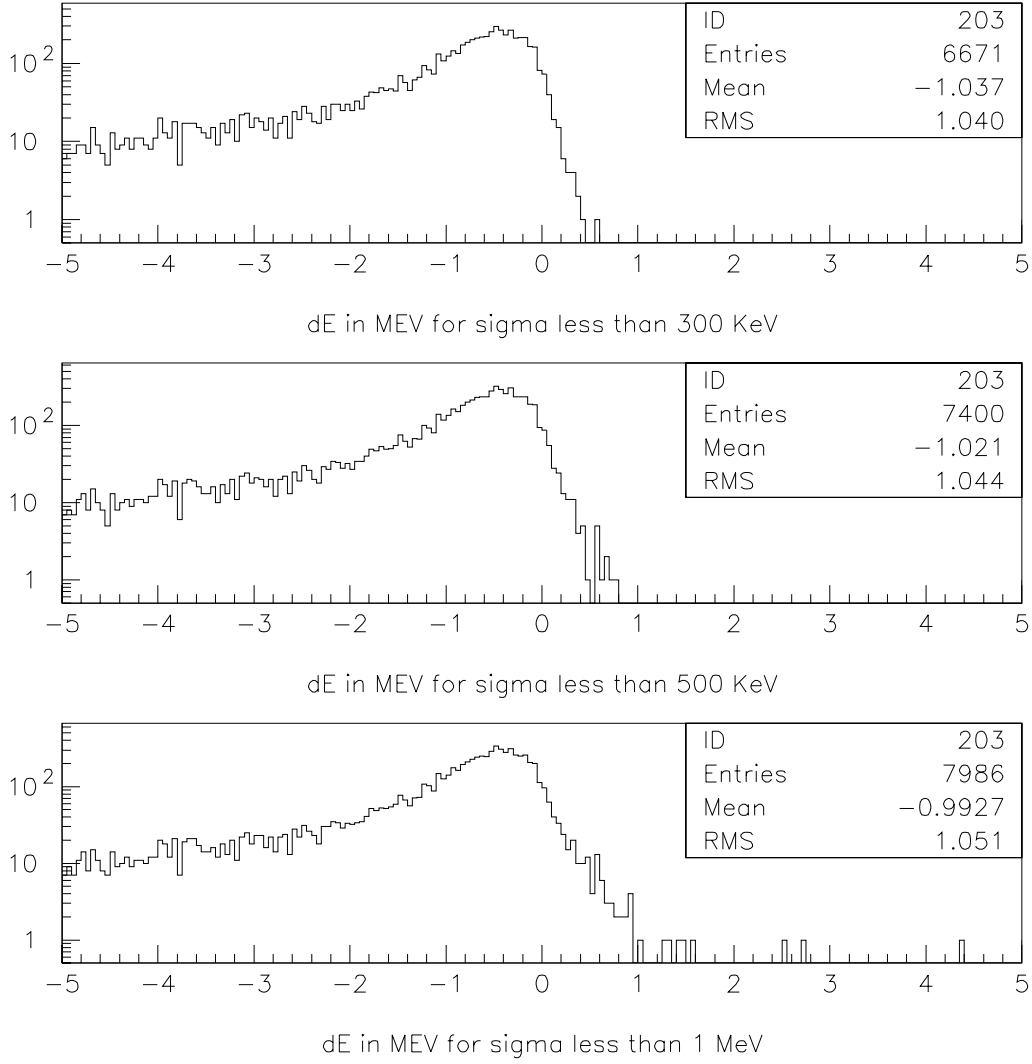


Figure 39: Distribution of error in the measured energy for various choice of  $\sigma_{pe}$  cut based on the full GEANT simulation of the straw detector, showing correlation between  $\sigma_{pe}$  and error.

We summarize the selection criteria used and their efficiencies in table 8. With the above cuts, the intrinsic energy resolution (excluding the effects of energy loss in the target and of spatial resolution in the tracking detector) is found to be 140 keV and 230 MeV respectively for the straw and fiber detectors. Adding the detector spatial resolutions increases the resolutions to 170 keV and 240 keV. Adding the effect of energy loss straggling in the target causes significantly worse resolution, and the energy response function deviates from a Gaussian shape at low energies. High energy tails in the resolution function are still suppressed. In this case, the FWHM for the straw and fiber detectors are 750 keV and 1000

Table 8: A summary of the selection criteria used in the electron momentum measurement for the MECO detector

Selection criterion	efficiency
At least 4 hits in total and 3 in a single turn	53%
Detected energy above 103.9 MeV	67%
$p_t > 75$ MeV at the detector	86%
Requirements on $L$ and $\sigma_{pe}$	85%
Overall acceptance	25%

keV, respectively. Figure 40 shows the detector response for the above four cases.

We have calculated [24] the level of intrinsic background from  $\mu$  decay in orbit by convolving the detector response function and the background electron energy spectrum. The latter is proportional to  $(E_{max}-E_e)^5$  near the endpoint [22]. We accept events with detected energy above a certain energy value  $\Delta$  relative to  $E_{max}$ . In this way, both the acceptance and background can be expressed as a function of  $\Delta$ . We then parameterize the noise to signal ratio as a function of the acceptance. Figure 41 is a plot the noise to signal ratio versus the acceptance for the two detector possibilities, after applying all selection criteria. At a noise to signal ratio of 0.05, the acceptance is 0.25 and 0.22 for the straw and fiber detectors, including effects of the target energy loss and the detector spatial resolutions. The values of  $\Delta$  in the fiber and straw detector case are both around  $\sim 1.1$  MeV.

Further suppression of some backgrounds can be gained by restricting the upper limit on the electron energy. A signal window as small as 1.5 MeV helps in reducing possible background events with negligible loss of signal.

One additional concern for the acceptance is the overlap of hits from multiple turns in the detector. Figure 42 plots a typical electron trajectory in the straw detector; there are overlapping hits in some detector elements. Two ways exist to minimize overlaps. One is to introduce energy loss between turns by putting material on the inner side of the cylindrical part of the detector. The baseline design has a thin layer of polyethylene inside the tracking detector. This has been included in the GEANT simulation used in the resolution calculation. In the scintillating fiber option for the detector, the total mount of material is three times as much as in the straw detector, and the loss in acceptance corresponds to only 10%.

A second way to eliminate overlaps is to have the downstream end of each straw at larger radius than the upstream end, so that the second pass would hit a different straw. The radius would have to be larger by about 1 cm. This could be implemented in the vanes rather easily. For the cylinder, it is more difficult, since the straws must be close packed to make them mechanically stable. A possibility is to make a polygon (of 8 or 16 sides) rather than a cylinder, and increase the distance of the downstream end from the axis. We will pursue these two possibilities.

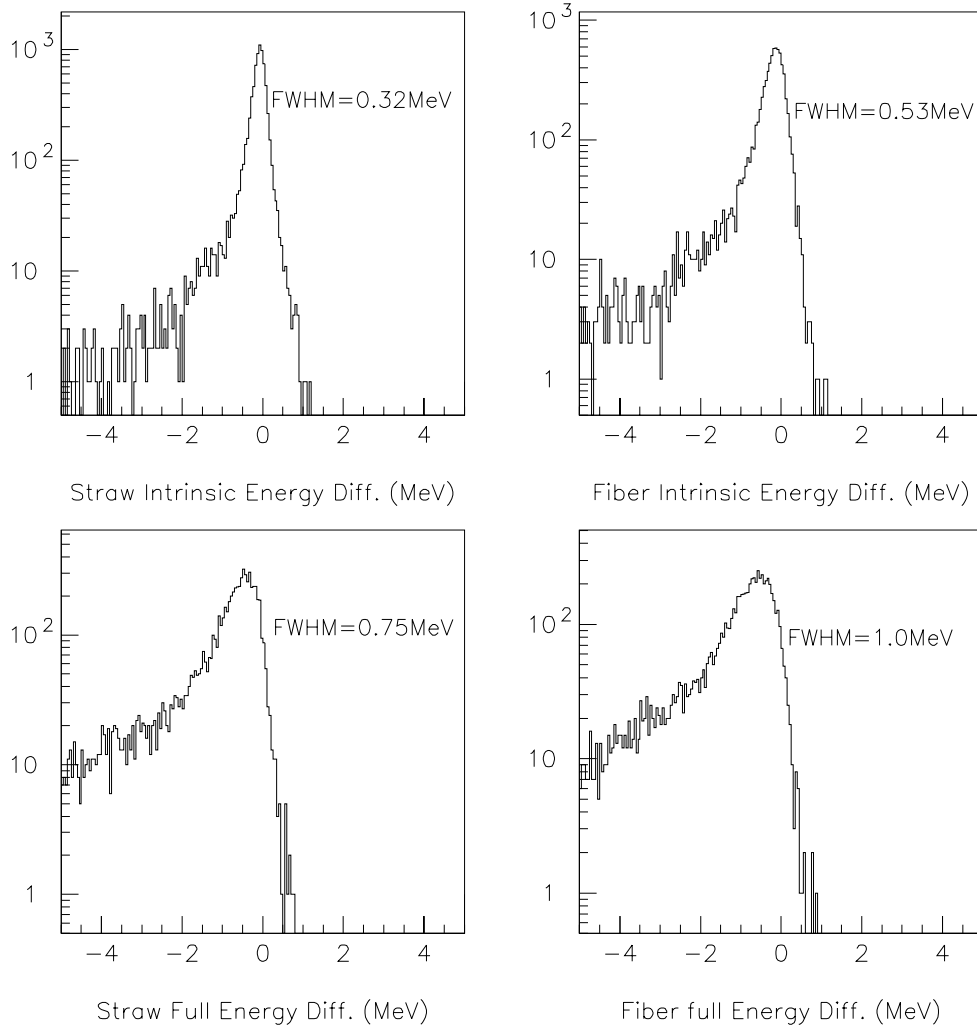


Figure 40: Distributions in the error in the reconstructed energy for the straw chamber implementation of the tracking detector (left) and for the mixed straw chamber and scintillating fiber implementation (right). For each, the resolution function without(top) and with(bottom) effects of energy straggling in the stopping target are shown.

### 8.3.2 Prototype Straw Chambers

As discussed earlier, the tracking spectrometer has straw chambers operated in vacuum as an essential feature. We have begun an R&D project to verify these devices can be built.

One test was of the ability to operate the straws in vacuum with sufficiently small leak rates. In our simulations, we have assumed we would use straws similar to those used in

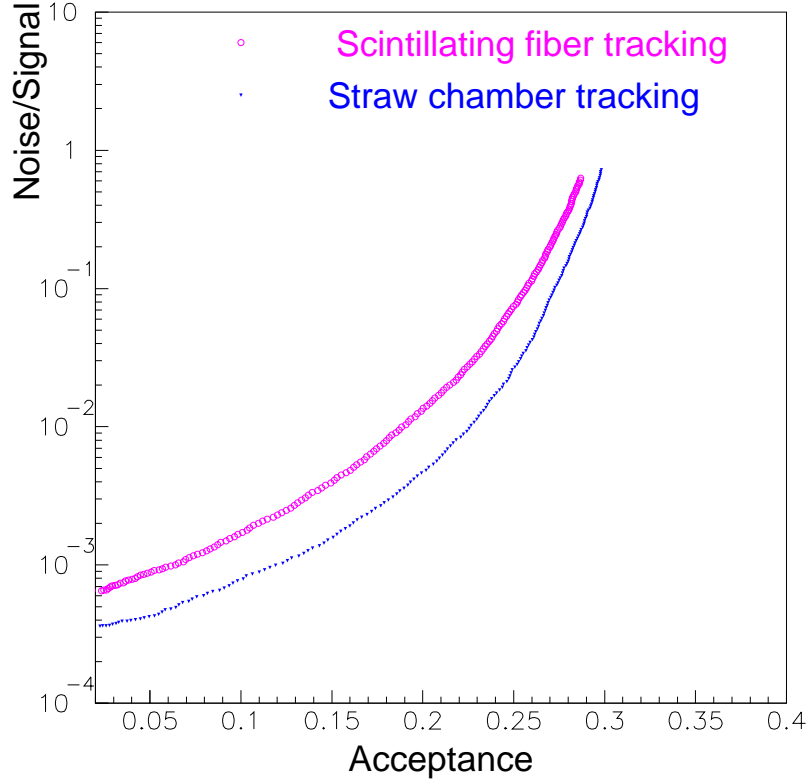


Figure 41: Noise/signal ratio as a function of the acceptance for the straw and fiber detector response, including effects of the target energy loss and detector spatial resolutions. At a noise to signal ratio of 0.05, the acceptances are 0.25 and 0.22.

E871. They are made of two layers of kapton, each .0005 inch thick, spiral wound with a half strip overlap. The inner layer has  $\sim 1000$  Angstroms of copper deposited on the interior. We tested the leak rate of both the bulk straw material and the end fittings by measuring the rate of rise of pressure in an evacuated tube in which sample straws with 1 atmosphere pressure were placed. The rate of rise of the chamber pressure was measured (with the pump valved off) as a function of pumping time. It decreased with pumping time, indicating the rise was due to outgassing of the exterior of the straw. The residual rise after 5 days of pumping corresponded to a leak rate of  $\sim 2 \times 10^{-8} \text{ l min}^{-1} \text{ m}^{-1}$  for the bulk straw, and a leak rate of  $\sim 3 \times 10^{-9} \text{ l min}^{-1}$  per end. These leak rates, when scaled to the full spectrometer, are well within pumping rates easily achievable.

We have now constructed prototype low-mass gas and electrical manifolds with which a fraction of a “vane” module will be assembled. This will allow us to test construction techniques and the leak tightness of the full assembly.

A second test was done of the deformation of straws when loaded by gas pressure and

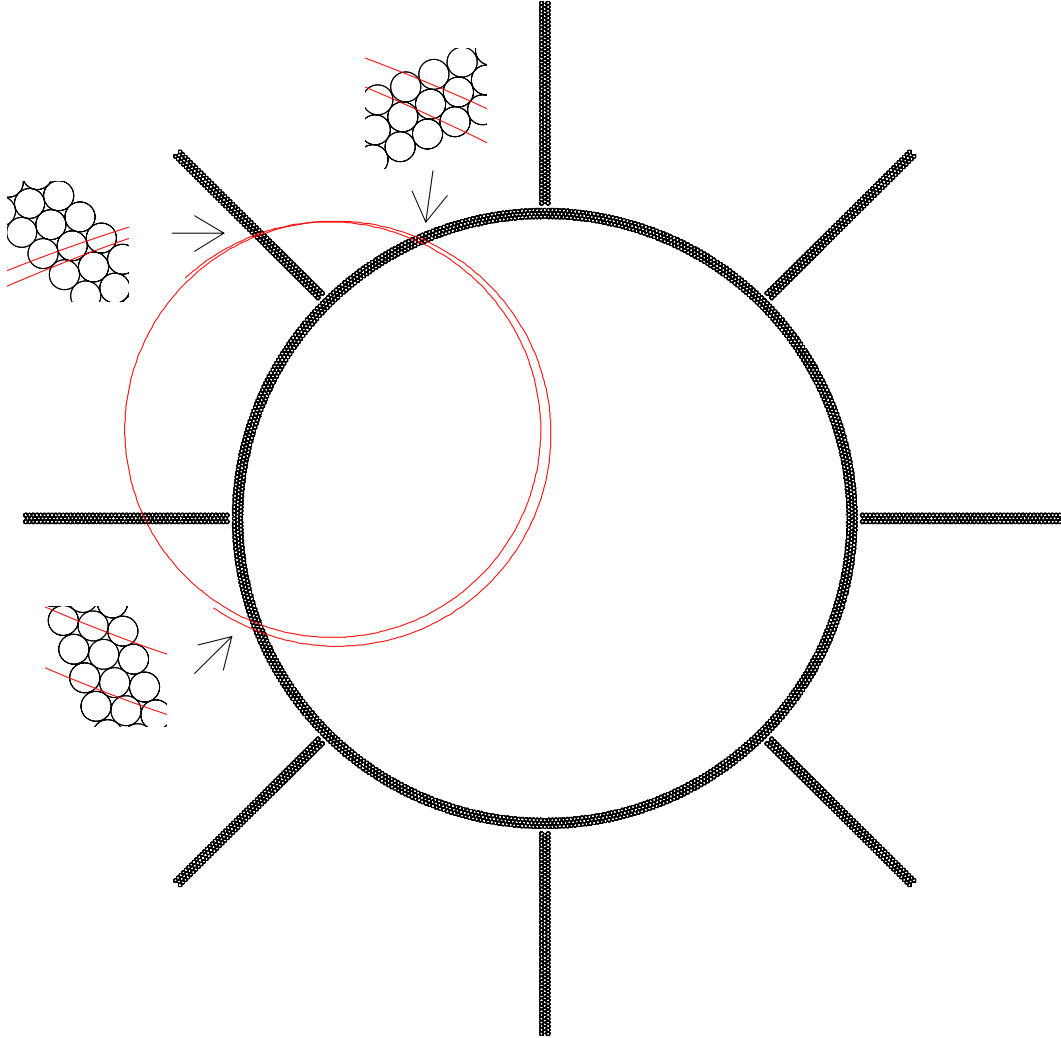


Figure 42: An electron trajectory in the region of the tracking detector, projected onto the plane perpendicular to the magnetic field. The enlarged pieces show detail of the particle track as it traverses the cylinder and vane, showing the overlap of hits in the same straw detector elements.

wire tension. If treated as a cylinder under tension due to the internal gas pressure, the tension is  $\sim 2.0$  N per straw. This exceeds the wire tension of  $\sim 0.5$  N. At issue is the extent to which the straw stretches due to this loading, which would cause them to bow if the length was constrained, or overtension the wires and complicate the construction if the length were allowed to change. We tested the fractional stretch by increasing the pressure in a sealed straw with one end fixed and the other free. The typical fractional change in length is 0.04% for 1 atmosphere overpressure. We will continue these studies with the multistraw “vane”

prototype.

A second significant feature of the straw chamber spectrometer is the use of pad readout for determining the coordinate along the straw. We have followed the development of Alan Schwartz [54] at Princeton, who has constructed prototype straw detectors for the HERA-B experiment. The straws are constructed of carbon loaded kapton, which allows an electrical signal to be induced on pads deposited on a thin layer of kapton which is glued to the exterior of the straw assembly. We envision layers of pads on either side of a three layer straw assembly, with charge readout of the pads. By interpolating the position based on the charge deposited on the pads, we anticipate a resolution of under 1 mm can be achieved with pads a few mm wide.

## 8.4 Electron Trigger Calorimeter

The purpose of the electron trigger calorimeter in the MECO experiment is to detect electrons with 105 MeV energy that have passed through the tracking system. Because these electrons are relatively low in energy, it is necessary to detect as much of the light generated by the stopping electrons as is possible, consistent with being immersed in a 1 T magnetic field. Due to the high rate of low energy particles hitting this detector, the trigger will require a segmented detector. The degree of segmentation is not yet well understood, and the design considered below is probably more segmented than necessary.

Our proposed detector [55] is a scintillator cylinder of outer radius 68 cm and inner radius 41 cm and 1 meter in length, shown in figure 43. The cylinder is composed of 32

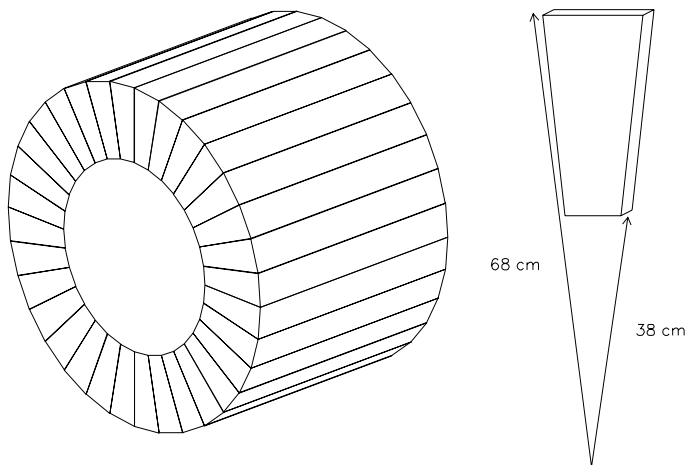


Figure 43: The MECO scintillating tile calorimeter containing 32 wedges, with each wedge containing 100 tiles 1 cm thick. Each tile is a wedge shaped 7.4 cm to 13.35 cm, by 30 cm on the edge.

wedge segments; each wedge consists of 100 scintillator tiles, each with a wave shifting fiber embedded within the tile. The light from each tile is brought to the rear of the cylinder by a waveguide fiber. Other groups [56, 57] have achieved good light output by reading out the tiles using waveshifting fibers. This same waveguide fiber acts as the readout waveguide fiber

and takes the light to the readout system. We assume that each tile is readout individually for a total of 3200 channels.

To act as a trigger, it is required that the calorimeter have high efficiency for those tracks that are well measured by the charged particle tracker. The energy resolution must be capable of separating the large number of electrons from  $\mu$  decay, which peaks at  $\sim 50$  MeV, from the  $\mu$  conversion electrons with energies of 105 MeV. The tracked electrons must satisfy the following requirements:

- 4 hits in tracking system
- 75 MeV/c transverse momentum

The energy deposition for 105 MeV electrons in the scintillator is shown in figure 44. The distribution was found using a GEANT calculation with the scintillator immersed in a 1 T magnetic field.

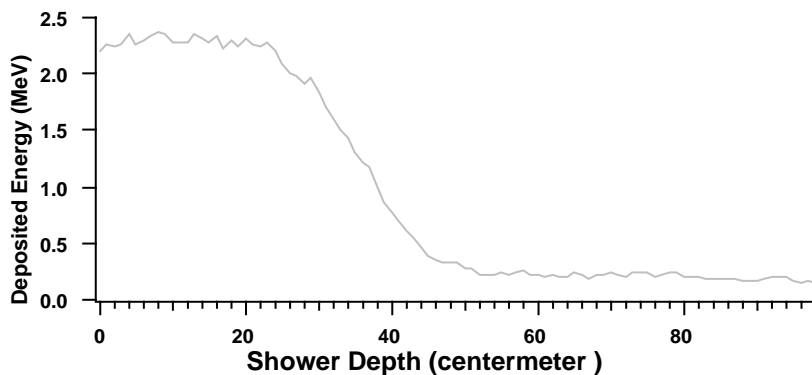


Figure 44: The mean  $dE/dx$  (MeV/cm) for a 105 MeV electron as a function of depth in scintillator immersed in a 2 T field. The calorimeter is 100 cm long.

The calorimeter design has a hole in the center to allow for the large flux of uninteresting  $\mu$  decay electrons to pass through the detector without interaction. This hole complicates the way in which the  $\mu$  conversion electrons interact with the calorimeter. There is a  $56\% \pm 1\%$  probability that a conversion electron will interact with the front face of the calorimeter. The other 44% spiral into the calorimeter to hit along its inner radius. No conversion electrons strike the outer radius of the calorimeter. The hit location probability distribution for hits in the inner radius is shown in figure 45. As can be seen, a one meter long calorimeter will intercept all the tracked conversion electrons.

Summing the total energy deposited in the calorimeter by 105 MeV conversion electrons measures the effective resolution of this calorimeter design. Some energy escapes the calorimeter and is not measured. The energy measured for 105 MeV conversion electrons that have at least 4 track coordinates measured, is shown in figure 46. The low energy tail is due to electrons that are near the transverse acceptance limit of the tracker. These electrons hit the inner radius and then scatter out of the calorimeter into a magnetic orbit that does not again intercept the calorimeter. Because of this only a fraction of their energy is absorbed in the calorimeter. The acceptance for conversion electrons hitting the front face

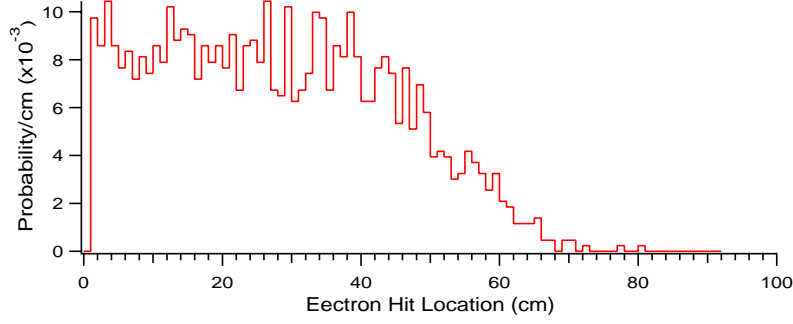


Figure 45: The probability for an electron to hit the inner radius of the calorimeter as a function of distance along the calorimeter. The plot is normalized to 1. The total probability to hit the inner radius is 44%.

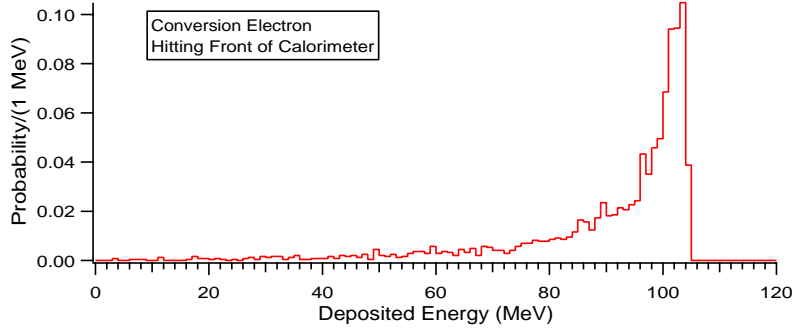


Figure 46: The theoretical energy resolution of the calorimeter for conversion electrons hitting the front face of the calorimeter. 56% of tracked conversion electrons hit the front face. The plot is normalized to 1.

and the inner radius are the same within the statistics used in our study. The comparison is made in table 9.

Table 9: The acceptance as a function of energy cut, for 105 MeV electrons. The results are shown separately for events hitting the front face and inside of the cylinder.

0 Cutoff energy (MeV)	Acceptance (front surface)	Acceptance (inner surface)
0	1.00	1.00
60	0.93	0.92
70	0.89	0.87
80	0.83	0.80

The energy deposited as a function of the location of the first hit of the conversion electron is displayed in figure 47. As can be seen, the resolution function is constant until about 60 cm along the inner calorimeter, after which the resolution becomes worse. This occurs because electrons of 105 MeV penetrate about 40 cm and the calorimeter is unable



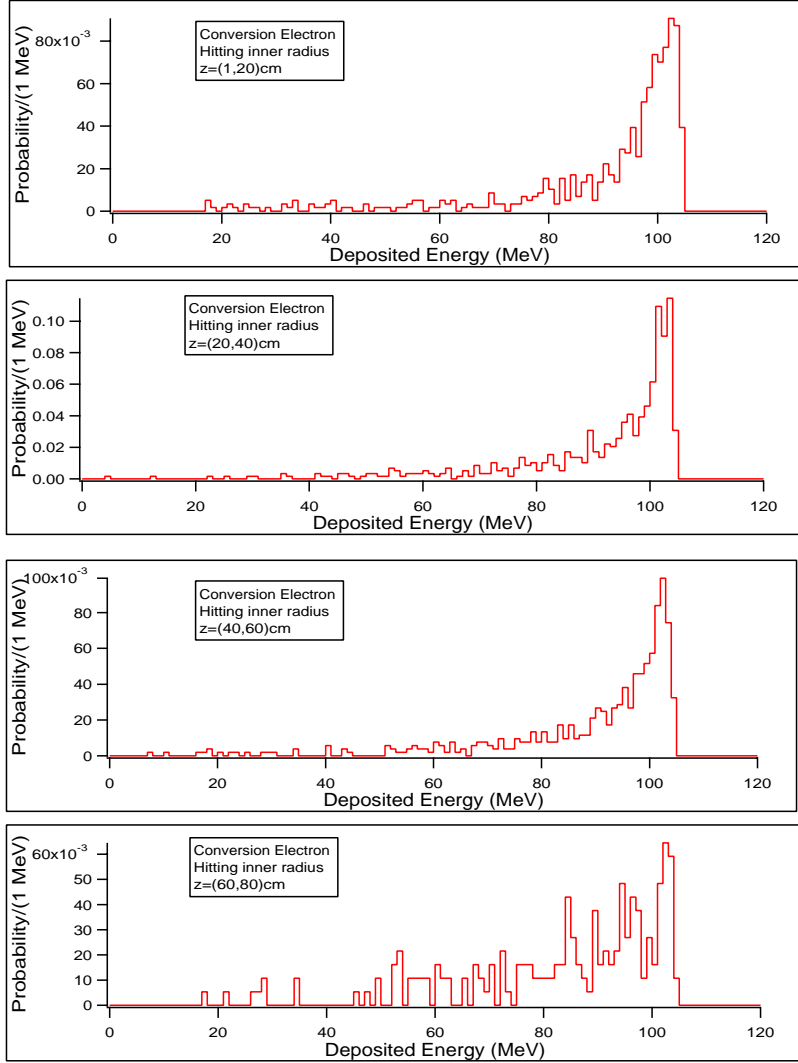


Figure 47: The deposited energy as a function of the location of the conversion electron hit in the inner radius of the calorimeter, for the case that all the energy deposited in the calorimeter is measured perfectly. Each plot is normalized to 1.

to contain the shower. However less than 1% of the tracked conversion electrons hit beyond a distance of 60 cm down the calorimeter, so that it is not worthwhile to extend the length of the calorimeter.

Because the calorimeter is read out using scintillating fibers there are two possible options for the phototransducer. One is to use multianode phototubes and the other is to use visible light photon counters (VLPCs). Each of these devices allows individual read out of the tiles and allows for a number of cross checks between the tracker and calorimeter and consistency checks within the calorimeter.

The light yield of each tile can be calculated using measured values found in reference [56]. Their results were for 0.4 cm thick tiles of various shapes. This group achieved about 8 photoelectrons per minimum ionizing particle, largely independent of the tile shape. The

results were found using phototubes (Q.E.  $\sim 0.18$ ) and 4 meters of waveguide fibers with 3 connectors between the scintillating fiber and phototube. The system performance achieved 1 photoelectron produced per 100 keV input into the tile system.

Using these results as a guide, we have simulated the effects of signal noise and measurement error in the calorimeter for phototubes and VLPCs. The resulting “intrinsic resolutions” are shown in figure 48. The VLPC’s provide good resolution of  $\sigma = 1.38$  MeV. For

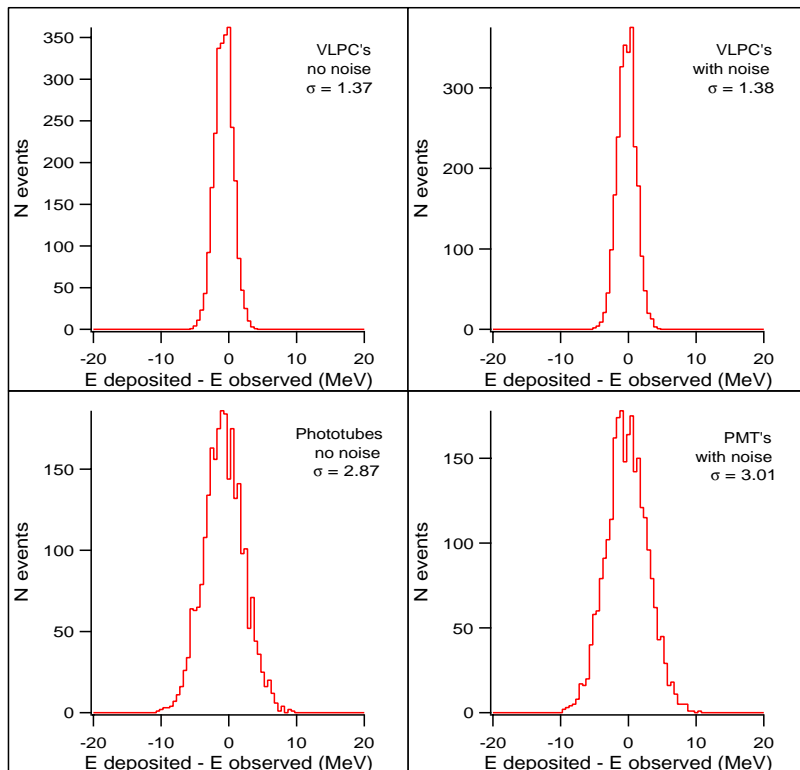


Figure 48: The intrinsic resolution of the calorimeter when read out using VLPCs and phototubes.

the purpose of determining the original energy of the electron, one must define an “effective resolution” which represents the probability that the energy measured in the calorimeter equals the original kinetic energy of the electron. Often, some energy leaves the calorimeter due to the open shape of the counter. Thus, in general, the deposited energy is less than the electron energy. Defined this way, the effective resolution is much poorer than the intrinsic resolution. To accept conversion electrons, we will need to trigger on energies as low as 65 MeV (90% acceptance). However, due to the high intrinsic resolution, such a cut will still discriminate well against low energy electrons from  $\mu$  decay and other processes.

We have not yet studied in detail the trigger rate in this device, and we make some comments here. First, we can easily shield it so no protons hit it, with a 1 mm passive absorber surrounding it. The flux of photons from the stopping target hitting this detector is about  $3 \times 10^8 \text{ s}^{-1}$  and these photons typically have 5 MeV. The typical size of a trigger element will be three wedges, summed over about 50 tiles. Figure 49 shows a simulation of the energy deposition due to 105 MeV electrons, showing that the energy is well localized.

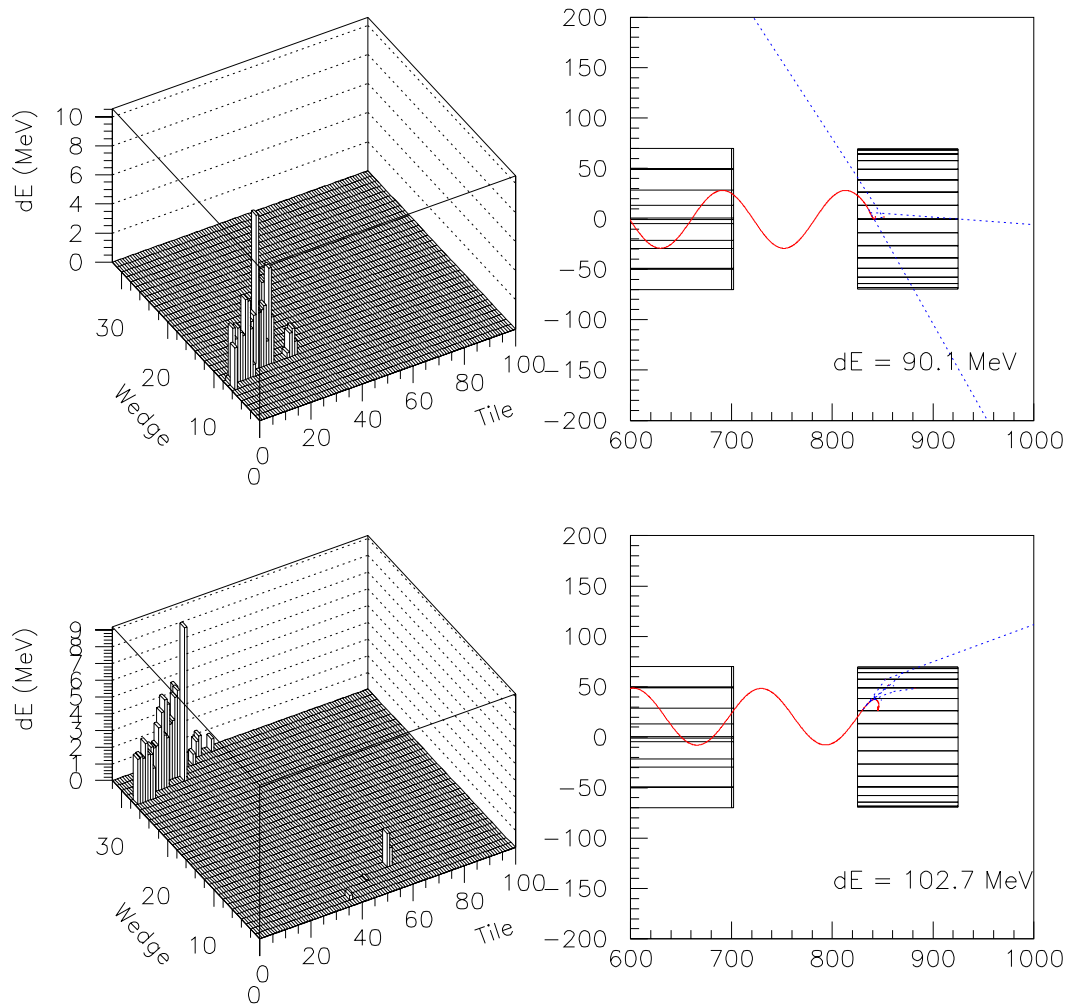


Figure 49: Event displays of two 105 MeV electrons incident on the electron trigger detector. The energy is typically localized in two wedges.

Assuming an integration time in the trigger of 30 ns, the typical number of photons impinging on a trigger element is about 1, introducing an additional 5 MeV in the resolution. The trigger rate from photon pileup is negligible. The trigger rate will be dominated by the tail of the muon decay in orbit electrons. The inner radius of the device can be adjusted to minimize this trigger rate with negligible effect on the resolution.

## 8.5 Cosmic Ray Shielding

Cosmic ray induced electrons (or  $\mu$ 's mistaken as electrons) may induce backgrounds and limit the sensitivity. Detailed calculation of the sources of backgrounds and the shielding requirements have been done and are described in this section.

We point out that the graded solenoidal detector has certain advantages with respect to cosmic ray induced background. Most importantly, there is a restricted range of  $p_t$  of electrons produced in the stopping target and detected in the spectrometer. For example, all electrons produced upstream of the stopping target (produced in the magnet pole piece, for example) can be eliminated by requirements on the  $p_t$  of the electron. The restricted range of allowed  $p_t$  also limits the phase space of electrons resulting from  $\mu$  decay or interactions in the detector.

In the rest of this section, we describe the calculation and results. The calculated flux is normalized to  $10^7$  sec of operation of the accelerator and experiment. The active time of the detector within that time is reduced by a factor of two for the 50% macro duty cycle (a one second spill each 2 seconds) and a factor of 2 for the detection time of 500 ns for each pulse every  $1 \mu\text{s}$ . The cosmic ray rate can be monitored during the 1 second each cycle when beam is not delivered to the target. As we will show, it will be necessary to use both active and passive shielding to reduce backgrounds to an acceptable level.

### 8.5.1 Background Rate Calculation

The calculation is based on measured cosmic  $\mu$  fluxes from the literature [58] and a GEANT simulation of the shielding and detector. Muons dominate the flux of particles penetrating any significant amount of shielding. The angular dependance is also taken from the literature. The distribution is approximated by  $dN/d\theta \propto e^{-0.25\theta}$ , with  $\theta$  in degrees. The calculation accounts for the following sources:

- Muons penetrating the shielding and decaying in the detector solenoid.
- Muons penetrating the shielding, interacting in the target, and making electrons.
- Muons penetrating the shielding, scattering in the target, and the  $\mu$  being mistaken for an electron.
- Muons interacting in the shielding and producing other particles (photons or hadrons) which then interact in the detector to produce electrons. These events may not deposit energy in a veto counter.

The  $\mu$  flux is about 60% positive. For decays and incident  $\mu$ 's mistaken as electrons, only  $\mu^-$  contribute. For delta rays and pair production in materials in the target and detector region, both  $\mu^+$ s and  $\mu^-$ s contribute.

The calculation starts with the measured muon energy spectrum. It is essentially flat out to 1 GeV, and then falls with a power law approximately given by  $E_\mu^{-2.5}$ . For an initial shielding arrangement, we used 2 m concrete, a scintillation counter detector, and 0.5 m steel. No magnetic field was used in the steel. Since it will probably provide a return yoke for the solenoid, it probably will be magnetized; this should improve the shielding. The attenuation was calculated assuming particles normally incident; this overestimates the flux penetrating the shielding.

The flux of particles exiting the shielding consists of  $\mu$ 's,  $\gamma$ 's, electrons and positrons, and lesser numbers of low energy hadrons. Figure 50 shows the GEANT particle type distribution for particles exiting the shielding. The effect of an additional meter of concrete

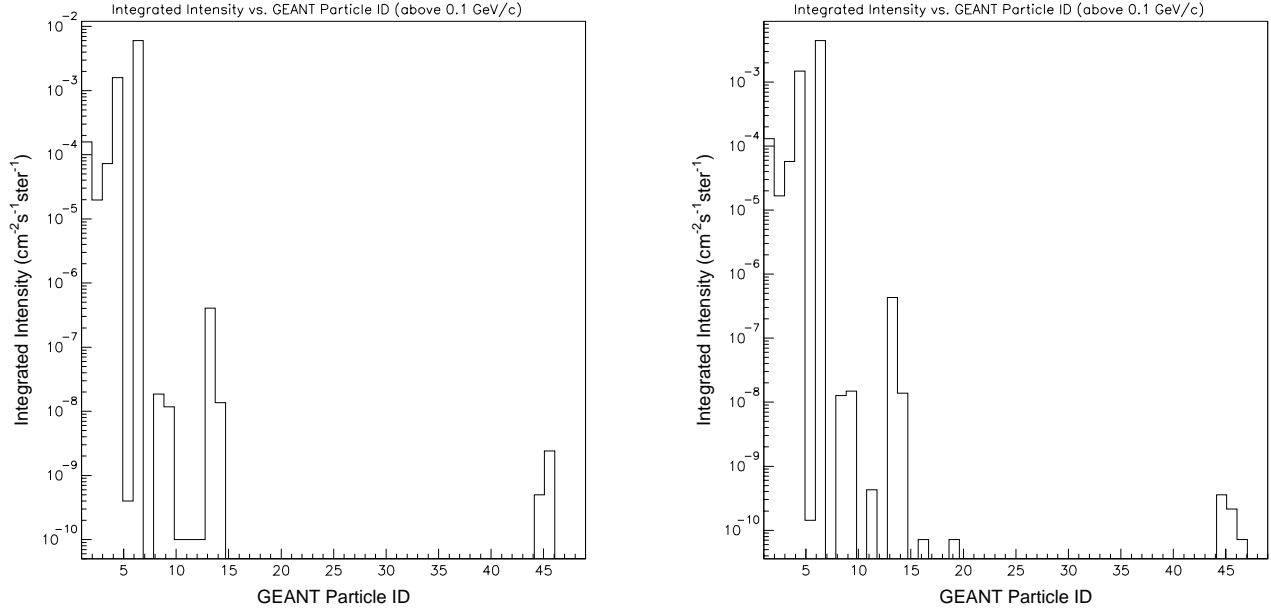


Figure 50: Plot of the number of particles emerging from the two shielding configurations. The particle codes are 1 ( $\gamma$ ), 2,3 ( $e^+, e^-$ ), 4 ( $\nu$ ), 5,6 ( $\mu^+, \mu^-$ ), 8,9 ( $\pi$ ), 13,14 (neutrons and protons), and other hadrons.

and half meter of steel is to attenuate the penetrating  $\mu$  flux by about a factor of 2. Figure 51 shows the differential intensities for  $\gamma$ ,  $e^\pm$  and  $\mu^-$  fluxes emerging from the nominal shielding. These fluxes were used as input to the calculation of the probability of producing a 100 MeV electron from cosmic rays.

Essentially all particles exiting the shielding deposited energy in a scintillation counter between the concrete and steel. A small flux of photons emerged without depositing energy in the scintillator. These are caused by bremsstrahlung by a  $\mu$  which then ranged out before passing through the scintillator. The probability of getting a photon with energy exceeding 100 MeV is  $\simeq 2 \times 10^{-6}$ . This contributes negligibly to the potential background from photons, assuming an inefficiency in the scintillator for detecting a penetrating charged particle is  $10^{-4}$  and has been neglected.

To estimate the background, the exiting flux of photons,  $e^\pm$ , and  $\mu^\pm$  was caused to impinge on the volume inside the detector solenoid. Particles were generated on the interior of a cylindrical shell (the magnet coil) according to the calculated flux of particles penetrating the shielding, and weighted by the cosmic ray flux as a function of zenith angle. The simulation of the resulting propagation and interactions was done including the effect of the magnetic field. All kinematic properties of all particles which intersected any part of the tracking detector were recorded, and selection criteria imposed. The selection criteria were the following:

- particle charge is negative
- particle momentum  $100 \text{ MeV}/c < p < 110 \text{ MeV}/c$

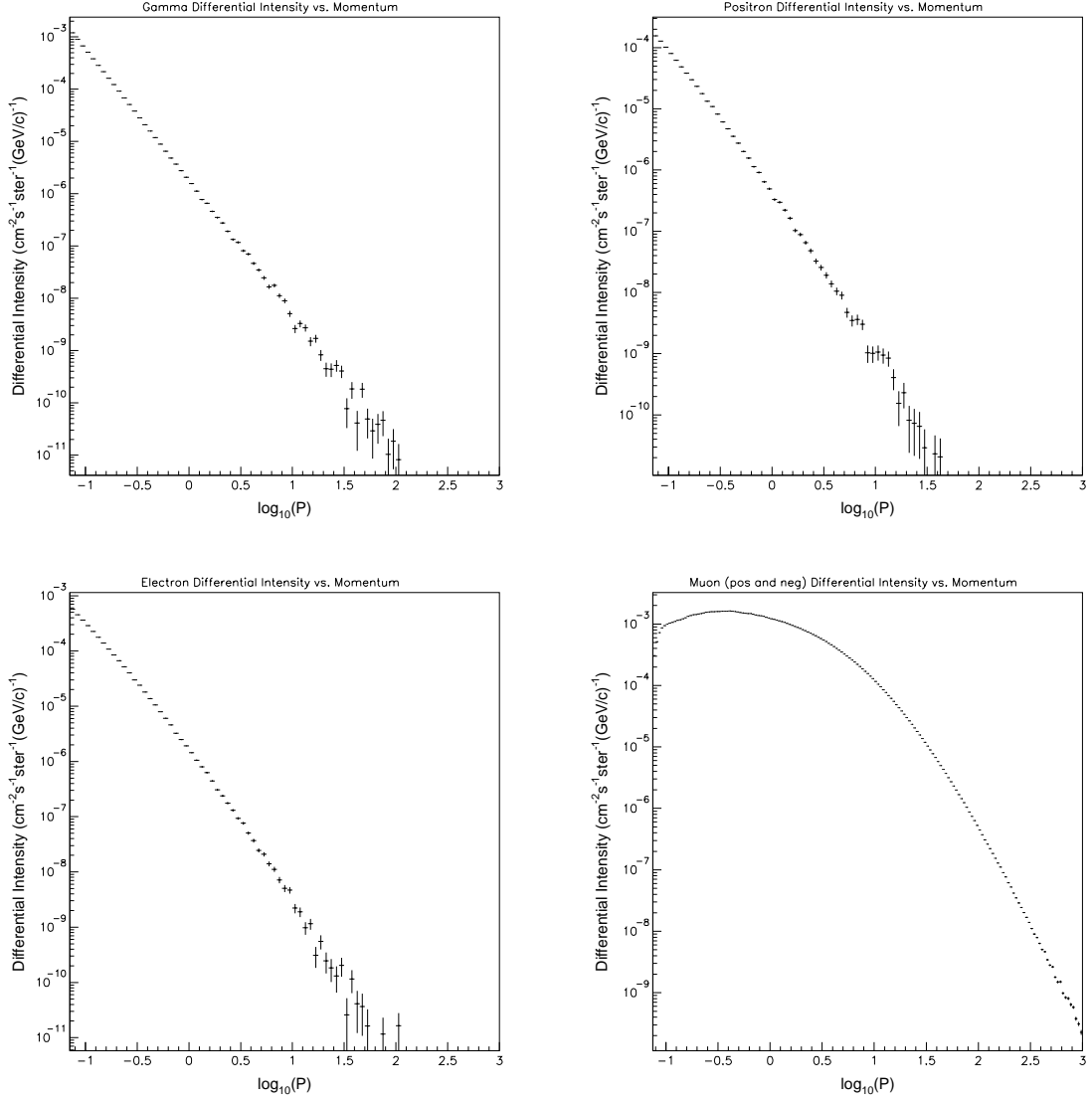


Figure 51: The differential intensities for particles emerging behind the minimum shielding configuration normal to the shielding surface, for the four background particle types with highest flux: upper left— $\gamma$ , upper right— $e^+$ , lower left— $e^-$ , and lower right— $\mu^-$ .

- number of hits in tracking detector:  $n > 3$
- ratio of transverse to axial momentum:  $1.0 < p_t/p_l < 1.83$
- closest distance to axis at stopping target:  $r < 10$  cm
- less than 3 missing hits in the fitted trajectory

The selection on ratio of transverse to axial momentum accounts for the fact that electrons produced in the stopping target have allowed values of this quantity in this range. The last selection criterion eliminates electrons originating in the middle of the detector, for which the fitted trajectory is predicted to pass through the cylinder and vanes 3 or more times without it having done so.

A total of  $9 \times 10^7$  particles was generated, distributed according to the particle type and momentum distributions calculated in the first part of the calculation. The incident trajectories were distributed isotropically over an area fully illuminating the interior of the solenoid. Taking the duty cycle of the accelerator to be 50%, the detection time for conversion electrons to be 500 ns each  $1 \mu s$ , assuming that we veto cosmic ray induced events using the veto scintillation counter with an efficiency of 0.9999, and accounting for the illumination area, this corresponds to 207 times our nominal  $10^7$  s running time.

A weight was applied to these events corresponding to the relative CR flux as a function of the zenith angle of the  $\mu$  which produced the event. A total of 24 (weighted) particles satisfying the above selection criteria was found. Most of these events were caused by particles produced downstream of the tracking detector (in the electron trigger detector, for example), moving upstream through the tracking detector, reflecting off the B field, and then moving downstream through the tracking detector a second time. Figure 52 shows the distribution in the number of hits in the tracking detector caused by particles moving upstream, for the 24 (weighted) background events. All but 3 (weighted) events have at least 4 hit segments in the tracking detector.

We will reconstruct the backward track, out of time in the tracking detector. Additionally, events produced in the electron trigger detector will have energy deposited at a time and position which can be deduced from the tracking information. We assume that these events will be vetoed with high efficiency. Of the particles with less than three backward hits, three (1.2 weighted) were  $\mu$ 's and can be eliminated by a time of flight requirement between the tracking detector and electron trigger counter. Three (1.2 weighted) others had more than 200 MeV deposited in the electron trigger counter, and can be eliminated by a cleanliness requirement in a small time and position window. One (.1 weighted) had only 27 MeV deposited in the electron trigger counter. The three (.7 weighted) remaining events were a  $\mu$  decay upstream of the tracking detector and two delta rays, one produced in the target and one in the straw detector. Figure 53 shows GEANT event displays of a sample of background events. The cosmic ray background is predicted to be 0.7 events at  $207 \times$  the nominal  $10^7$  running time, or a background of 0.0035 events.

### 8.5.2 Hardware Implementation

The cosmic ray shield completely surrounds the detector solenoid. Assuming a length of 12 m and appropriate endwalls, the total volume is  $\sim 200$  m<sup>3</sup> of concrete, and  $\sim 65$  m<sup>3</sup>

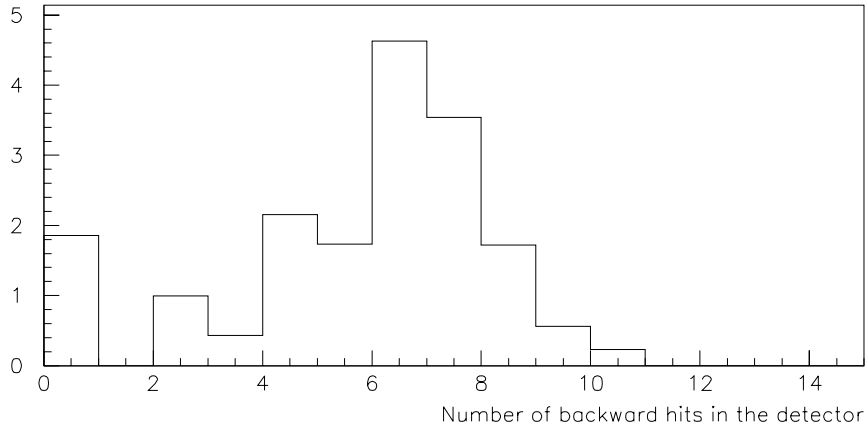


Figure 52: The distribution in the number of hits caused by a particle as it was moving upstream through the detector. The entries are weighted by the zenith angle dependence of the cosmic ray  $\mu$  flux.

of steel. The scintillator will be consist of  $\sim 260 \text{ m}^2$  of plastic scintillator. To achieve an inefficiency below  $10^{-4}$ , we assume a double layer of active detectors will be required.

The veto scintillator will be arranged in a box made of 1500 rectangular extruded scintillator bars 6.5 m in length and 4 cm wide and 1 cm thick. The end bars will be 4 m in length by 4 cm wide by 1 cm thick. The scintillator bars will be co-extruded with a titanium oxide outer coating to improve the light output of the bar. The narrow bars will allow for dense placement around support structures. The light generated in the bar will be brought out to phototubes using waveshifting scintillating fibers.

A single bar will be readout from both ends. Two waveshifting fibers will pass through the entire length of the bar. Each end of these fibers will be read out by a separate phototube, to assure redundancy. A single phototube will transduce the light from 20 fibers. The complete system will require only 300 phototubes. Failure of a single phototube will not cause a hole in the veto system. Fibers from the top layer of bars will not share tubes with fibers from the lower layer.

The MINOS group has made light yield measurements [59] on a system similar to this proposal. Measurements using 8 m long by 4 cm wide by 1 cm thick scintillator bars have achieved 7 photoelectrons for minimum ionizing particles passing through the center of the bar. The signal consisted of the sum of the phototube (Q.E.=12%) signals readout using 1mm scintillating fibers readout from each end of the bar. The signal reached 12 photoelectrons at the end of the bar.

Because MECO requires a shorter scintillating bar the worst signal is expected to be 8 photoelectrons in the center of the bar. Other improvements such as the use of a titanium oxide coating on the bar and the use of extended range phototubes (Q.E.=18%) can further improve the worst case signal to about 10 photoelectrons. However, in either case the



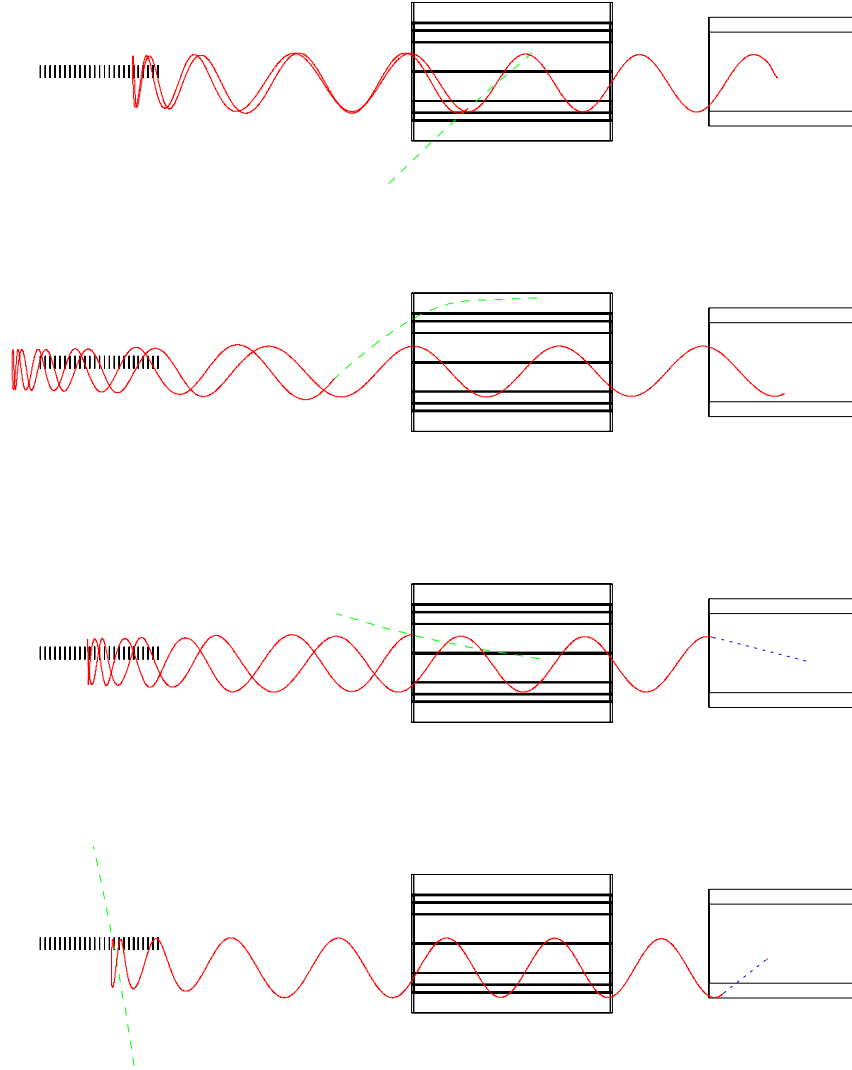


Figure 53: Sample CR induced background events. The top event is a delta ray produced in the straw material. The second is a  $\mu$  decay which cannot be eliminated. The third is a delta ray produced in the straw chamber gas manifold (eliminated because it deposited too little energy in the electron trigger detector), and the fourth is a delta ray produced in the stopping target.

photoelectron yield is more than adequate. With the goal of a system wide inefficiency of  $10^{-4}$ , a single layer inefficiency of  $10^{-2}$  is acceptable. A worse case signal level of 8 photoelectrons means the scintillator contribution to the system inefficiency is less than  $10^{-3}$  per layer. The cracks between scintillating bars will be the dominant contribution to the inefficiency of a single layer. Assuming spacing cracks of 0.5mm the single layer inefficiency will be  $\sim 10^{-2}$ . However, because each layer is staggered with respect to the other, the system inefficiency should be less than  $10^{-5}$ , well within the experiment's design goal.

## 9 MECO Expected Performance and Sensitivity

We first discuss the fraction of  $\mu$  captures in the timing window, to which the sensitivity is directly proportional. This fraction depends on the specific choice of the time structure of the pulsed beam as well as the distribution  $\mu$  stopping times. We estimate this fraction for two scenarios for the pulse spacing, 900 ns and 1350 ns (corresponding to 3 and 2 bunches in the AGS revolution time). We assume the accepted time window starts at 600 ns after the proton pulse hits the production target, or 550 ns after the time a particle moving at velocity  $c$  and traveling axially along the solenoids arrives at the stopping target. We take a very conservative approach and end the signal time window just before the arrival at the stopping target of velocity  $c$  particles from the next pulse moving with momentum completely along the transport solenoid axis. Figure 54 shows the  $\mu$  stopping time distribution relative to the proton arrival at the production target. The average stop time is 370 ns. Using this

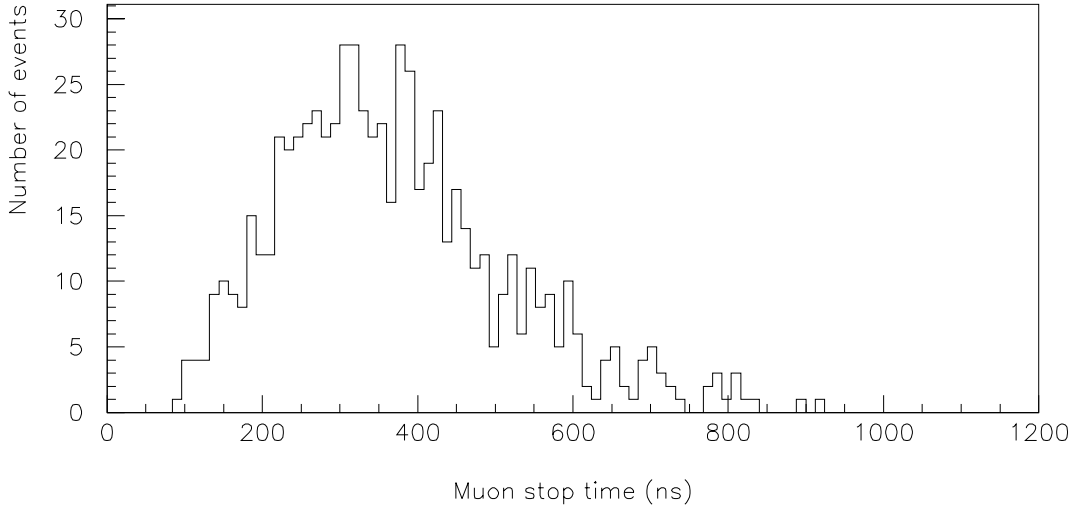


Figure 54: The distribution of the  $\mu$  stop time relative to the time when the proton beam impinges on the production target

distribution and a  $\mu$  lifetime in aluminum of 880 ns, we calculate the fraction of  $\mu$  stops in the time window starting at 600 ns and ending at 950 ns or 1400 ns to be 39% and 58% for the 900 ns and 1350 ns pulse separation, respectively. If the start of the timing window is delayed to 700 ns with the end of the timing window unchanged, the corresponding fractions are 27% and 49%. This reduction in sensitivity can be compensated in the following way. By increasing the length of the transport solenoid, the  $\mu$  arrival time is delayed minimizing the effect of the delayed start of the time window on the probability of  $\mu$  captures occurring in the accepted time window. Further, the end of the time window can also be delayed due to increased transport distance. It is estimated that by adding five meters to the transport solenoid, the  $\mu$  stopping time will be delayed by about 100 ns. With the start of the timing window at 700 ns and the end of it delayed by 15 ns, the capture probability in the accepted time window is calculated to be 31% and 54% for the 900 ns and 1350 ns pulse spacing, respectively.

The other factors entering into the sensitivity are the running time, the proton intensity, the number of  $\mu$ 's per proton produced and transported to the stopping target, the stopping probability, the fraction of stops which capture (as opposed to decay), the trigger efficiency, and the tracking acceptance. Missing from this table are loss of events due to accidental cosmic ray vetos, which are expected to be small, deadtime losses, which are also expected to be small, and losses in pattern recognition in the tracking detector, which we have not estimated. The factors entering the sensitivity are given in table 9. With one year ( $10^7$  s) running time with both the AGS and experiment working, a few events can be detected at a value of  $R_{\mu e} = 10^{-16}$ . Even with the  $\mu$  yield calculated with the most pessimistic of the

Table 10: A summary of the expected MECO sensitivity for a one year ( $10^7$  s) run. The  $\mu$  yield is calculated for an 8 GeV proton beam incident on a tungsten target using the GHEISHA hadron production model.

Running time (sec)	$10^7$
Proton flux ( $\text{sec}^{-1}$ )	$2 \times 10^{13}$
$\mu/p$ entering solenoid	0.012
Stopping probability	0.37
$\mu$ capture probability	0.60
Fraction of $\mu$ which capture in time window	0.31-0.54
Electron trigger efficiency	0.90
Fitting and selection criteria(see table 8)	0.25
Detected events for $R_{\mu e} = 10^{-16}$	3.7-6.5

hadronic codes, the expected number of events is more than one for  $10^7$  s of data collection.

Table 9 shows the expected background rates for the sensitivity quoted above. The backgrounds scale in different ways, and we tabulate the backgrounds with the following assumptions. For  $\mu$  decay in orbit and radiative  $\mu$  capture, the background scales with the number of captured  $\mu$ 's, and hence is directly proportional to the sensitivity. For beam electrons and  $\pi$ 's, we assume the background will also scale with the sensitivity, since the biggest uncertainty in the sensitivity is due to the  $\pi$  yield, to which the beam electron and  $\pi$  fluxes are also proportional. For cosmic ray backgrounds, we assume the sensitivity can be achieved in  $10^7$  seconds of beam and detector on time. This background is inversely proportional to the rate at which data is collected.

The background is dominated by the  $\mu$  decay in orbit contribution which gives about 0.05 events for a sensitivity of one event for  $R_{\mu e} = 10^{-16}$ , and scales with the experimental sensitivity. However, substantial improvements in discrimination against this source of background can be had with modest loss in acceptance, as shown in figure 41. For example, the background/signal ration can be decreased from 0.05 to 0.02 with a relative loss in sensitivity of less than 10%.

Many of the background depend on the proton beam extinction. We explicitly assume that the number of protons hitting the production target during a time corresponding to the detection time is less than 1 for  $10^{10}$  protons hitting the target during the beam pulses.

Table 11: A summary of the level of background from various sources, calculated for the sensitivity given in the previous table, and with scaling as discussed in the text. The numbers given are for a sensitivity of 5 events for  $R_{\mu E} = 10^{-16}$ .

Source	Events	Comment
$\mu$ decay in orbit	0.19-.33	signal/noise = 20 for $R_{\mu e} = 10^{-16}$
Radiative $\mu$ capture	$<< 0.05$	
$\mu$ decay in flight	$< 0.003$	without scatter in target
$\mu$ decay in flight	0.004	with scatter in target
Radiative $\pi$ capture	0.007	from proton during detection time
Radiative $\pi$ capture	0.014	from late arriving $\pi$
$\pi$ decay in flight	$<< 0.001$	
Beam electrons	$< 0.02$	
Cosmic ray induced	0.004	assuming $10^{-4}$ CR veto inefficiency
Total background	0.29-.41	

This beam extinction has not been demonstrated, although we are confident it can be done. The background from late arriving  $\pi$ 's depends very much on the details of the  $\pi$  production and transport and is difficult to model with good sensitivity. We have discussed a number of ways in which this background can be further suppressed and are confident that the quoted suppression can be achieved using one of the available techniques.

At the proposed level, the experiment is not expected to be limited by background.

## 10 MECO Equipment Cost

We here summarize the expected cost of the beam and apparatus. Essentially all costs are based on scaling arguments and experience of other experiments. They are summarized in table 10.

The majority of the cost of this experiment is in the beam lines, primarily in the cost of the superconducting solenoids. We have estimated the cost of these magnets based on scaling relationships [62] between the amount of stored energy and the cost. That estimate is \$6.4M, excluding the cost of refrigeration and the return yoke. This cost has gone down from the time of the LOI since the field is now better known, and the size of some of the magnets has decreased. We have made a guess at the cost of the refrigerator and the pole pieces and return yoke. Some relatively intricate pole pieces may be needed at the interfaces of the solenoids in order to maintain a continuously decreasing axial component of the field. The estimate of the solenoid costs is clearly very imprecise.

A second potentially costly item is the secondary extinction device. In scenarios using either electrostatic kickers or magnetic kickers, the cost is expected to be dominated by the cost of the 15 power supplies running at frequencies from 1-15 MHz. These have been estimated [36] at \$75000 per power supply, with a total cost for the kicker, including the

mechanical parts, of \$1200k.

The detector costs have been estimated with varying degrees of sophistication. For the tracking detector, the cost is mostly in the electronics – 13000 channels of pad readout and 3200 channels of wire readout. We estimate very roughly \$100 per channel for the complete electronics cost. The detector itself is comparable in numbers of channels to the E871 system. We estimate the cost at \$500k. For the fiber tracker, the channel count is increased, and VLPC's are used, somewhat increasing the cost.

The cosmic ray shield cost is estimated based on information from MINOS on similar large area planar scintillator arrays with fiber readout. We include the cost of the phototubes and electronics. We also include here the cost of shielding material, concrete and steel, which accounts for the majority of the cost.

The electron trigger detector cost is dominated by the scintillator and the VLPC's. It is not clear that such a high degree of segmentation is required, and substantial savings could be had by using small area phototubes and coarser segmentation. This may also save on scintillator costs. Our estimate is based on fine segmentation and VLPC's.

Data acquisition should be rather straightforward, as the trigger and data rates should be low.

We take a contingency of 40% based on the lack of reliability of physicists' estimates of costs.

Table 12: A summary of the estimated costs of the MECO beam and detector. The source of the estimates is discussed in the text.

Item	Cost (\$/1000)
Electrostatic kicker	1200
Production solenoid	2700
Transport solenoid	1700
Detector solenoid	2000
Magnetic and cryogenic design	200
Refrigerator and controls	2000
Pole pieces and return yokes	800
Cosmic ray shield and readout	900
Wire tracking spectrometer and readout	2100
Hybrid tracking spectrometer and readout	3000
Electron trigger and readout	600
Trigger electronics, online computing	400
Contingency	6000
Total with full straw detector	20700
Total with mixed fiber and straw detector	21600

We will continue to pursue the option of incorporating the resources available to the INR group. That group has sufficient superconducting cable to make the solenoids, a large fraction of the steel necessary for the pole pieces and return yokes, and high purity aluminum which could be used for the cryostats and coil support. We request that BNL convene a group

of experts to examine the Russian magnet technology and determine if it is a cost effective and technically reliable option for producing some or all of the solenoids.

## 11 MECO R&D Plan

There are a number of important outstanding studies to be done:

- We need to reduce the uncertainty in the expected  $\mu$  yield. We hope that the measurements of E910 will help in that respect. It may be necessary to do some independent measurements. We will continue to try to optimize the  $\mu$  yield with further target and beam improvements.
- We need to make more reliable the calculations of backgrounds, primarily those associated with prompt processes. This will require more detailed studies of beam issues, including information about the performance of a secondary extinction device, the time distribution of late arriving pions, and the ability of the  $\mu$  transport system to absorb high momentum electrons.
- We need to study the issue of how to do the pattern recognition, finding which hits in a realistic, high rate environment correspond to the track of a 105 MeV electron. A necessary ingredient in this is a realistic simulation of the environment, with a GEANT simulation of extra hits from the background particles discussed earlier.

We will shift the emphasis of our work towards engineering issues and tests of critical parts of the experiment in the next year. The main issues to be addressed early in this program are the following.

- We will continue work on the design of the tracking spectrometer. We will finish a baseline design of a spectrometer using straw tubes of two meters length operating in vacuum. We will test the mechanical construction of the straw assembly, including gas tightness, maintaining straightness of straws with gas pressure and wire loading, developing a mounting and alignment technique, and developing means of electrical connections and vacuum feedthroughs. We will follow the work of the Princeton group on pad readout of straws and prototype a pad straw chamber.
- We will develop the alternate tracking detector design using scintillating fibers in the cylindrical part of the spectrometer.
- We plan further tests of the bunched beam extraction, including extracting with 2 filled bunches, and extracting at 8 GeV.
- We will measure the beam emittance, particularly tails which might allow beam particles to get through the secondary extinction device (the electrostatic kicker). This will require beam tests with a low field magnet and a long straight section with some beam focusing magnets and a septum magnet. We hope to do these tests in the upcoming SEB run.

- We will choose the technology for the secondary extinction device, either electrostatic or magnetic, and design and prototype at least two segments of the kicker. We request that BNL do this design and prototyping.
- We request that BNL do an engineering design of the production target, the heat and radiation shielding in the production solenoid, and the dump for the proton beam.
- We request that BNL begin the magnetic and cryogenic design of the full suite of superconducting solenoids. This will require interaction of a physicist in our collaboration with a superconducting magnet engineer. It has been estimated by Michael Green at LBL that it will require six months engineering FTE to produce a magnet specification that could go out to commercial vendors for quotes.

In addition, there are collaboration issues to address. The strength of the collaboration is insufficient at present. Many people have expressed interest in the experiment, but are reluctant to commit given the uncertainty in the future of BNL. This issue will hopefully be resolved with the HEPAP subpanel recommendation. We are actively working to strengthen the collaboration.

## 12 Acknowledgements

We thank David Garcia, Rina Lim, and Houtan Rezaei, who made valuable contributions to many of the calculations in this proposal and to the preparations of the figures.

## References

- [1] M. Bachman, *et al.*, “A Search for  $\mu^- N \rightarrow e^- N$  with Sensitivity Below  $10^{-16}$ , AGS Letter of Intent (1996).
- [2] R.M. Djilkibaev and V.M. Lobashev, Sov., J. Nucl. Phys. **49(2)**, 384 (1989).
- [3] “MELC Experiment to Search for the  $\mu^- A \rightarrow e^- A$  Process”, V.S. Abadjev, *et al.*, INR preprint 786/92, November 1992.
- [4] R. Cahn and H. Harari *et al.*, Nucl.Ph **B176**, 135 (1980).
- [5] K. Arisaka, *et al.*, Phys. Rev. Lett. **70**, 1049 (1993).
- [6] T. Akagi, *et al.*, Phys. Rev. Lett. **67**, 2614 (1991).
- [7] K. Arisaka, *et al.*, Phys. Rev. Lett. **71**, 3910 (1993).
- [8] P. Krolak *et al.*, Phys. Lett. **B320**, 407 (1994).
- [9] A. M. Lee *et al.*, PRL **64**, 165 (1990).
- [10] U. Bellgardt *et al.*, Nucl. Ph. B, 299 (1988).
- [11] R.D. Bolton *et al.*, PRD **38**, 2077 (1988).
- [12] F. Riepenhausen, talk at the Sixth Conference on the Intersections of Particle and Nuclear Physics (1997).
- [13] D. Barlow *et al.*, P969 to LAMPF (1985).
- [14] Y. Kuno and Y. Okada, LANL hep-ph/9604296 (1996);  
Y. Kuno, A. Maki and Y. Okada, LANL hep-ph/9609307 (1996).
- [15] Barbieri, *et al.*, “Violations of Lepton Flavour and CP in Supersymmetric Unified Theories”, IFUP-TH 72/94, January 1995.
- [16] Arkani-Hamed, *et al.*, “Flavor Mixing Signals for Realistic Supersymmetric Unification”, LBL-37343 (1996).
- [17] Barbieri and Hall, “A Grand Unified Supersymmetric Theory of Flavor”, LBL-38381 (1996).
- [18] Hisano *et al.*, “Exact Event Rates of Lepton Flavor Violating Processes in Supersymmetric SU(5) Model”, LBL-38653 (1996).
- [19] W. Marciano, private communication.
- [20] A. vanderSchaaf, private communication.
- [21] Badert *et al.*, Nucl. Physics **A377**, 406 (1979).



- [22] O. Shankar, Phys. Rev. **D25**, 1847 (1982).
- [23] D. Koltick, meco020, “Light Yield From a Scintillating Fiber Tracker” (1997).
- [24] T. Liu, meco-004, “Initial Resolution Studies” (1997).
- [25] A. Frischknecht, *et al.*, Phys. Rev. **C2**, 1506 (1985).
- [26] T. Stoudl, *et al.*, Nucl. Phys. **A91**, 520 (1967).
- [27] R.A. Eramzhyan, *et al.*, Nucl. Phys. **A290**, 294 (1977).
- [28] M. Overlin, meco-014, “Estimates of Cosmic Ray Induced Background for MECO” (1997).
- [29] N. Mukhopadhyay, Phys. Rep., **30**, 1(1977).
- [30] T. Kozlowski, *et al.*, Nucl. Phys., **A436**, 717(1985).
- [31] V. Balashov and R. Eramzhyan, “Muon Capture by Nuclei and Problems of Weak Interactions”, Atomic Energy Reviews **5**, (1967);  
H. Morinaga and W. Fry, Nuovo Cimento **10**, 308 (1953);  
C. Ishi, Prog Theoretical Physics **21**, 663 (1959).
- [32] Wyttenbach, *et al.*, Helv. Phys. Acta, **49**, 776 (1976).
- [33] R. Lee, meco-017, “Timing Measurements of AGS Bunched Beam Extraction” (1996).
- [34] W. Molzon, meco-006, “A Pulsed Electrostatic Kicker for Secondary Extinction” (1997).
- [35] A. Soukas, private communication.
- [36] A. Soukas, J. Sandberg, W. Meng, “A Pulsed Kicker for Secondary Extinction in a Proton Beam”, BNL AGS memo, (1997).
- [37] W. Molzon, meco-008, “Schematic of Transport Solenoid Based on Russian SC Cable” (1997).
- [38] “Beam Dynamics and Technology Issues for  $\mu^+\mu^-$  Colliders”, J. Gallardo ed., 1995.
- [39] “ $\mu^+\mu^-$  Collider a Feasibility Study”, the  $\mu^+\mu^-$  collaboration, ed. J. Gallardo (1996).
- [40] I. Chemakin *et al.*, P910 to BNL AGS (1995).
- [41] P.A. Aarnio, *et al.*, CERN/TIS-RP/190 (1987).
- [42] H.C. Fesefeldt, “Simulation of Hadronic Showers, Physics and Applications”, PITHIA Report, Aachen 85-02 (1985).
- [43] V.S. Barashenkov, N.M. Sololevsky and V.D. Toneev, Atomn. Energ. **32**, (1972).
- [44] N. Mokhov, “The MARS code System Users’s Guide” FNAL-FN-628 (1995).

- [45] J. Ranft, “The DPMJET Code System” (1995).
- [46] Y. Pang, *et al.*, Nucl. Phys. **A544**, 435 (19920).
- [47] J. Sculli, meco-021, “A Check of GHEISHA using BNL E910 Data” (1997).
- [48] R. Djilkibaev, meco-009, “Pion Yield and Muon Flux Simulation” (1997).
- [49] M. Bachman and R. Lim, meco-016, “Study of Muon Yields in MECO” (1997).
- [50] R. Djilkibaev, meco-010, “Proton Target Temperature Simulation” (1997).
- [51] R. Brun, *et al.*, “GEANT3”, DD/ee/84-1, CERN (1984).
- [52] A.N. Zalikman and L.S. Nikitin, “Tungsten”, Moscow Press (1978).
- [53] D. Garcia and W. Molzon, meco-018 “A Study of Heat Loads on the MECO Production Solenoid” (1997).
- [54] A. Schwartz, private communication.
- [55] S. Carabello and D. Koltick, meco-015, “Scintillating Tile Calorimeter for MECO” (1997).
- [56] S. Aota, *et al.*, Nuclear Instruments and Methods **A352**, 557 (1995).
- [57] J. Ernwein, SCIFI 93, World Scientific, Ed. A.D. Bross, /it et al., 265 (1994).
- [58] O. Allkofer, *et al.*, Phys. Lett. **36B**, 425 (1971).
- [59] A. Parra, private communication. Work to be published in Nuclear Instruments and Methods.
- [60] S. Aota, *et al.*, Nuclear Instruments and Methods, **A352**, 557 (1995).
- [61] Y.K. Chen, *et al.*, Nucl. Inst. Meth. **A372**, 195 (1996).
- [62] M.A. Green, R.A. Byrns, and S.J. St. Lorant, Advances in Cryogenic Engineering **37**, Plenum Press, New York (1992).